FE-PML Modeling of Guided Elastic Waves and its Applications to Ultrasonic NDE

by

Abdel-Rahman Mahmoud

A Thesis
submitted to the Faculty of Graduate Studies
in partial fulfilment of the requirements for the degree of

Doctor of Philosophy

Mechanical and Manufacturing Engineering Department
Faculty of Engineering, University of Manitoba
Winnipeg, Manitoba

Abstract

This thesis investigates the use of a combined finite element and perfectly matched layer approach in modeling guided elastic wave motion in infinite plates and cylinders and its potential applications to non-destructive evaluation. Underlying principles of the perfectly-matched, absorbing layer are demonstrated on one-dimensional wave propagation in a semi-infinite elastic rod.

Feasibility of using the perfectly matched layer as absorbing boundary condition in the finite-element modeling of guided elastic wave propagation and scattering is studied for the canonical problem of shear horizontal wave motion in isotropic plates. Numerical results in this study are validated against exact analytical solutions. Excellent agreement has motivated the endeavour to take the technique to the next level of pressure, shear-vertical wave motion in isotropic and transversely isotropic plates.

Time-domain, finite-element formulation of the perfectly matched layer for pressure, shear-vertical wave motion was validated through comparisons with semi-analytical literature data and reciprocity checks. Numerical implementation of the model was employed in studying the effect of crack presence on the time of arrival in a pitch-catch, non-destructive inspection arrangement. Predictions made confirmed previously-reported experimental findings.

Extensions into three-dimensional, Cartesian and cylindrical spaces were validated against reported data. Practical examples of wave scattering in damaged concrete beams, oil and gas pipelines, and composite shells demonstrated the potential use of the proposed model in simulating elastic-wave based non-destructive inspection. Up to 80 % of the computational time needed to run an extended-mesh, finite-element model can be saved by introducing the perfectly-matched, absorbing layer to the finite-element model as the current thesis proposes. This significant saving in computational time by the proposed FE-PML model can accelerate the production of artificial neural network training data or help tackle complicated non-destructive testing applications.

Acknowledgments

"Praise be to God, Lord of all that exist." (Quran 1:1) I am grateful to my advisor, Dr. Quan (Abraham) Wang for his guidance and support, and to committee members: Dr. Nipon Rattanawangcharoen and Dr. Yunhua Luo for their constructive feedbacks and the much appreciated help in vetting thesis manuscript.

This study was supported mainly by a University of Manitoba Graduate Fellowship and partially by Natural Science and Engineering Research Council of Canada; both are kindly acknowledged. I would like to thank my manager at Schlumberger Reservoir Completion, Kevin Scarsdale, for kindly allowing me a one-month leave of absence to expedite my thesis write-up.

Every conversation I had with my parents back in Egypt has planted roses of hope, belief, and confidence in my abilities to bring this effort to fruition. Last but not least, special appreciation goes to my wife, Sara, for providing me with the necessary atmosphere of understanding and support during the untold number of hours it took to complete this work.

Dedication

“And lower to them the wing of humility out of mercy and say my Lord! Have mercy on them as they have brought me up when I was little.” (Quran 17:24) I dedicate this work to my parents.

Contents

Front Matter

List of Tables

List of Figures

List of Abbreviations

General Abbreviations

1D	one dimension or one-dimensional
2D	two dimensions or two-dimensional
3D	three dimensions or three-dimensional
ABCs	absorbing boundary conditions
ANN	artificial neural networks
BE	boundary-element
BEM	boundary element method
BIEM	boundary integral equation method
CEM	computational electromagnetics
CFD	computational fluid dynamics
CFRP	carbon-fibre reinforced plastic
CPU	central processing unit
EFIT	elastodynamic finite-integration technique
FFT	fast Fourier transform
FDM	finite-difference method
FDTD	finite-difference time-domain
FE	finite-element
FEA	finite element analysis
FEM	finite element method
GRI	Green's reciprocity identity
Im ()	imaginary part of an the entity in brackets
IMSL	international mathematical and statistical library
MSLM	mass-spring lattice model
MWR	method of weighted residuals
NDE	non-destructive evaluation
NDI	non-destructive inspection
NDT	non-destructive testing
NME	normal modes expansion
PDE	partial differential equation
P-C	pitch-catch
P-E	pulse-echo

PML	perfectly matched layer
PSV	pressure, shear-vertical (wave)
PUFEM	partition of unity FEM
Re ()	real part of the entity in brackets
SAFE	semi-analytical finite-element
SAFT	synthetic aperture focusing technique
SEM	strip-element method
SFEM	spectral, finite-element method
SH	horizontally-polarized shear (wave)
TFRs	time-frequency representations
TOFD	time-of-flight diffraction
XFEM	extended FEM (a special variant of the PUFEM)
EMFE	extended mesh finite element (model)

Journal Titles Abbreviations (in bold)

Advances in **Theo**retical and **Appl**ied **Mech**anics
Applied **Math**ematical **Modelling**
British **J**ournal of **Non**-**Destr**uctive **Test**ing
Bulletin of the **Seism**ological **Soc**iety of **Am**erica
Composites **Eng**ineering
Composite **Struct**ures
Computational **Methods** in **Appl**ied **Mech**anics and **Eng**ineering
Computers and **Struct**ures
Computers, **Mater**ials, and **Contin**ua
Finite Element in **Anal**ysis and **Des**ign
Geophysical **J**ournal **Int**ernational
Geophysics
IEEE Transactions on **Antennas** and **Propag**ation
IEEE Transactions on **Microwave Theory** and **Tech**niques
IEEE Transactions on **Sonics** and **Ultrason**ics
IEEE Transactions on **Ultrason**ics, **Ferroelectr**ics, and **Freq**uency **Control**
Insight
International **J**ournal of **Comput**ational **Methods**
International **J**ournal of **Mech**anical **Sci**ences
International **J**ournal of **Numer**ical **Methods** in **Eng**ineering
International **J**ournal of **Pressure Vessels** and **Piping**
International **J**ournal of **Solids** and **Struct**ures
International **J**ournal of **Struct**ural **Stab**ility and **Dyn**amics
Journal of **Acoust**ic **Emiss**ion
Journal of **Appl**ied **Mech**anics, **Trans**actions of **ASME**
Journal of **Appl**ied **Phys**ics
Journal of **Composi**te **Mater**ials
Journal of **Comput**ational **Acoust**ics

Journal of **Comput**ational **Phys**ics
Journal of **Eng**ineering **Mech**anics
Journal of **Intell**igent **Mater**ial **Syst**ems and **Struct**ures
Journal of **Mech**anical **Sci**ence and **Technol**ogy
Journal of **Nondestr**uctive **Eval**uation
Journal of **Pressure Vessel Technol**ogy, **Trans**actions of **ASME**
Journal of **Sound** and **Vib**ration
Journal of the **Acoust**ical **Soc**iety of **Am**erica
Journal of **Vib**ration and **Acoust**ics, **Trans**actions of **ASME**
Materials **Eval**uation
Mechanics of **Mater**ial
Microwave and **Opt**ical **Technol**ogy **Lett**ers
NDT & E International
Nondestructive **Test**ing and **Eval**uation
Research in **Nondestr**uctive **Eval**uation
Russian Journal of **Nondestr**uctive **Test**ing
SIAM Journal of **Numer**ical **Anal**ysis
Structural **Health Monit**oring
Ultrasonics
Wave Motion

List of Symbols

Roman Letters

$\mathbf{0}$	null vector
A	cross-sectional area
A_0	the first anti-symmetric Lamb mode
b	breadth of a rectangular plate
c	bar wavespeed
$c_{ij},\ i, j = 1\ldots6$	elements of the matrix of elastic constants, $\boldsymbol{c}$
c_p	pressure wavespeed
c_s	shear wavespeed
$\boldsymbol{c}_{ij},\ i, j = x, y, z$	the stiffness matrices associated with the derivatives of displacement with respect to variables i and j
$\boldsymbol{c}$	the matrix of elastic constants, $c_{ij},\ i, j = 1\ldots6$
C_l	an expansion coefficient corresponding to normal mode l
Co_l'	stress coefficient term $j\xi_l \cos\beta_l z_i$ corresponding to normal mode l, hybrid method
d	damping profile
d_0	damping profile amplitude
D	source-receiver separation distance
e	the base of a natural exponential function (approximately 2.718281828)
E	young's Modulus
E_l	displacement coefficient exponential term $e^{j\xi_l x_i}$ corresponding to normal mode l, hybrid method
f	internal force
g_{kl}	Green's function (displacement at point k due to a load at point l)
$\boldsymbol{G}$	displacement coefficients matrix, hybrid method
G_i	displacement coefficients vector at point i, hybrid method
G_{12}	shear modulus in a composite laminate
h	plate's thickness
$\boldsymbol{H}$	stress coefficients matrix, hybrid method
H_i	stress coefficients vector at point i, hybrid method

$\boldsymbol{I}_2$	a 2 by 2 identity matrix
$\boldsymbol{I}_3$	a 3 by 3 identity matrix
$\boldsymbol{I}_i,\ i=x,z$	matrices of 1s and 0s used in the definition of $\boldsymbol{c}_{ij}$ as $\boldsymbol{c}_{ij}=\boldsymbol{I}_i\boldsymbol{c}\boldsymbol{I}_j,\ i,j=x,z$ in 2D Cartesian coordinates
$\boldsymbol{I}_i,\ i=x,y,z$	matrices of 1s and 0s used in the definition of $\boldsymbol{c}_{ij}$ as $\boldsymbol{c}_{ij}=\boldsymbol{I}_i\boldsymbol{c}\boldsymbol{I}_j,\ i,j=x,y,z$ in 3D Cartesian coordinates
j	imaginary unit
$\boldsymbol{J}_i,\ i=0,r,\theta,z$	matrices of 1s and 0s used in the definition of $\boldsymbol{c}_{ij}$ as $\boldsymbol{c}_{ij}=\boldsymbol{J}_i\boldsymbol{c}\boldsymbol{J}_j,\ i,j=0,r,\theta,z$ in 3D cylindrical coordinates
$\boldsymbol{J}'_i,\ i=0,r,z$	matrices of 1s and 0s used in the definition of $\boldsymbol{c}_{ij}$ as $\boldsymbol{c}_{ij}=\boldsymbol{J}'_i\boldsymbol{c}\boldsymbol{J}'_j,\ i,j=0,r,z$ for axisymmetric problems
$\boldsymbol{k}$	element stiffness matrix
$\boldsymbol{K}$	global stiffness matrix
L	computational domain length
L_c	crack length
L_P	PML length
$\boldsymbol{m}$	element mass matrix
m	damping profile exponent
$\boldsymbol{M}$	global mass matrix
M	number of normal modes
n	local shape functions
N	global basis functions
n_0	number o elements between the observation points and the PML boundary
n_e	number of elements
n_n	number of global nodes
n_P	number of elements inside the PML along the absorption direction
n_s	number of sampling points in a time history signal
n_Γ	number nodes on the boundary $\Gamma=\Gamma^-\cup\Gamma^+$
n_n^e	number of nodes per element
p	external force
p_0	amplitude of applied harmonic force
$\boldsymbol{p}$	element force vector
$\boldsymbol{P}$	global force vector
$\boldsymbol{q}$	element displacement vector
$\boldsymbol{Q}$	global displacement vector
$\dot{\boldsymbol{Q}}$	global velocity vector
$\ddot{\boldsymbol{Q}}$	global acceleration vector

r_i	inner radius of a pipe or a cylindrical shell
R_a	amplitude reflection coefficient
R_P	theoretical reflection coefficient from the PML
t	time
t_0	time delay in a Gaussian signal
T	time of arrival
u	axial or x -displacement
u_o	amplitude of incident, harmonic axial displacement in a slender rod
$\dot{u}$	axial or x-velocity in a slender rod
$\ddot{u}$	axial or x-acceleration in a slender rod
$\widehat{u}$	reflected axial displacement wavefield in a slender rod
$\widehat{u}_o$	reflected x- displacement amplitude
v	anti-plane displacement in a plate or $\theta-$displacement in a cylinder
w	z -displacement
W_c	crack width
x	x -coordinate or axis
x_o	x -coordinate of observation point
x_c	x -coordinate of surface-breaking crack trip
x_p	x -coordinate of loading point
$\overline{x}$	stretched x-coordinate inside PML region
y	y -coordinate axis
y_o	y -coordinate of observation point
y_p	y -coordinate of loading point
z	z -coordinate axis
z_o	z -coordinate of observation point
z_c	z -coordinate of surface-breaking crack trip
z_p	z -coordinate of loading point
Z	impedance
Z_0	impedance at $x = 0$
Z_L	impedance at $x = L$

Greek Letters

α	the angle a crack makes with the x-axis
β	wavenumber in the thickness, z-direction, of a plate
δ	Dirac delta function
Δ	a prefix that denotes an increment in the subsequent variable or parameter
Δf	an increment in the internal axial force in a slender rod

Δt	an increment in time or time step
Δu	an increment in axial or x-displacement, u
Δx	an increment in x, element size in the x-direction
Δy	an increment in y, element size in the y-direction
Δz	an increment in z, element size in the z-direction
ε	tensile strain
ε_{RMS}	root-mean-square error in FE-PML predictions compared to EMFE
γ	shear strain
Γ	$\Gamma^- \cup \Gamma^+$
Γ^-, Γ^+	boundaries of Ω_c, hybrid method
λ	wavelength
μ	shear modulus of an isotropic material
ν	Poisson's ratio
ν_{12}	Poisson's ratio
ν_{23}	Poisson's ratio
Π	standard FE assembly of element contributions
θ	circumferential coordinate in a 3D cylindrical frame
ρ	mass density
σ	stress, axial stress in a slender rod
σ_G	a parameter that controls the width of a Gaussian signal
τ	applied surface traction (stress)
ω	angular frequency
$\omega_{\bar{c}}$	centre frequency
Ω	problem domain
Ω_C	finite computational domain
Ω_e	a finite element domain
Ω_P	$\Omega_{P+} \cup \Omega_{P-}$
Ω_{P+}, Ω_{P-}	left and right PML regions
Ω_∞	infinite physical domain
$\Omega_{-\infty}, \Omega_{+\infty}$	semi-infinite regions, hybrid method
$\bar{\Omega}_\infty$	$\Omega_{+\infty} \cup \Omega_{-\infty}$
ξ	wavenumber in the axial or x-direction
ζ	coordinate stretching function

"*If I have seen further it is by standing on the shoulders of giants*" Isaac Newton's letter to Robert Hooke on February 5, 1675

Chapter 1

Introduction

1.1 Preamble

Plates, beams, and cylinders are encountered so frequently in engineering applications. Bridge slabs, pipelines, and rails are few real-life examples, see Figure 1.1. They may deteriorate due to sever service or environmental conditions. Interior and exterior pipeline wall thinning, for example, poses a major problem for the oil & gas industry due to reduced integrity. Another example is the development of cracks in concrete bridge slabs as a result of overloading or drastic changes in surrounding temperature, which is typical of the North American climate. Therefore, safety regulations and economical strategies may require regular inspections or continuous monitoring of these structures in a non-invasive fashion.

Non-destructive inspection (NDI) can be visual, optical, magnetic, radiographic, thermographic, nuclear, or elastodynamic. Elastodynamic, NDI can be either vibration- or elas-

tic-wave-based. Vibration inspection exploits variation in modal frequencies, mode shapes, frequency response functions or time histories to characterize a defect [1, 2]. Traditional elastic-wave inspection methods (e.g. pulse-echo, through transmission, and pitch-catch) employ a single point source/point receiver arrangement to recognize a defect from changes in received signals [3]. Modern elastic-wave imaging techniques (e.g. synthetic aperture focusing technique, SAFT) employ multiple source/receiver arrangement to scan a structure for defects [4].

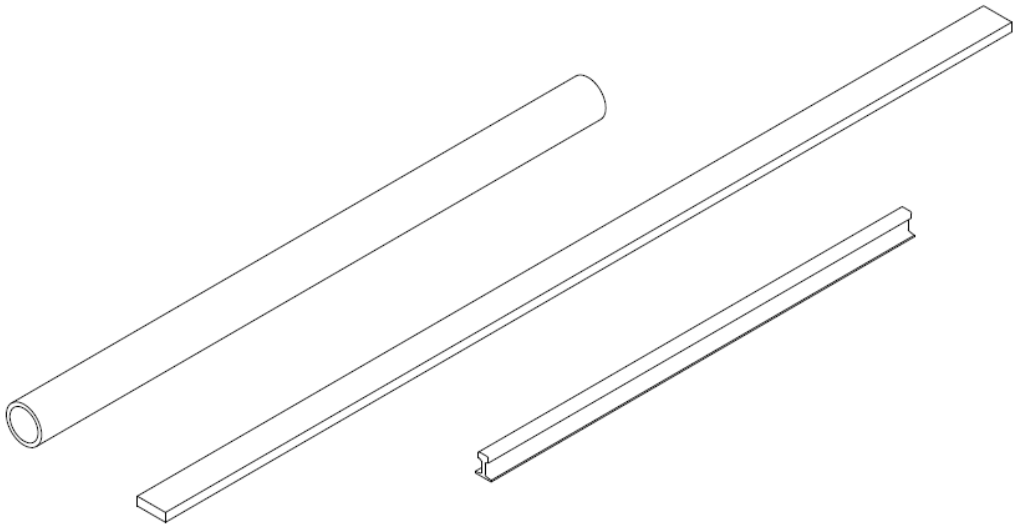

Figure 1.1 Real-life examples of cylindrical and plate-like structures

In the context of elastic-wave NDI, cylindrical and plate-like structures are collectively known as elastic waveguides and the waves propagating in them are known as guided elastic waves. The presence of guided elastic waves with long wavelengths has given elastic-wave inspection methods great potential in rapid, long-range examination of cy-

lindrical and plate-like structures. Several researchers have investigated this potential [5-8]. Dalton et al., for example, have concluded that guided elastic waves possess good sensitivity to localized damage [6]. Rose has given an extremely comprehensive account of the state-of-the-art as well as the future vision of NDI with guided elastic waves [7]. In structural health monitoring with guided elastic waves, a comparison between the measurements of a flawed structure to the measurements of an identical but flawless one is needed. Conducting such a comparison by physical experiments is not only expensive and time-consuming but may also be impossible in some cases. Fortunately, mathematical modeling offers a viable alternative. Mathematical modeling can be analytical, numerical, or a combination of both (semi-analytical). Analytical and semi-analytical models are accurate and inexpensive. Moreover, our basic understanding of elastic-wave phenomena is from these models. However, they are based on simplifications of geometry and/or boundary conditions. Therefore, they are only applicable to simple cases. The more practical yet complex problems can only be handled by numerical methods.

1.2 Numerical Elastic-wave Modeling

More than fifty years ago, major developments in engineering and technology were driven by advances in experimental and analytical techniques. The advent of powerful computers has accelerated the use of already-existing numerical methods and motivated the development of new ones. By now, numerical methods have become so widely accepted and intensely used that one can argue that they constitute the third pillar of mod-

ern research and development in both academia and industry beside experimental and analytical techniques. For example, any researcher or new product developer cannot dispense with, at least, basic understanding of how finite element analysis (FEA) and computational fluid dynamics (CFD) work.

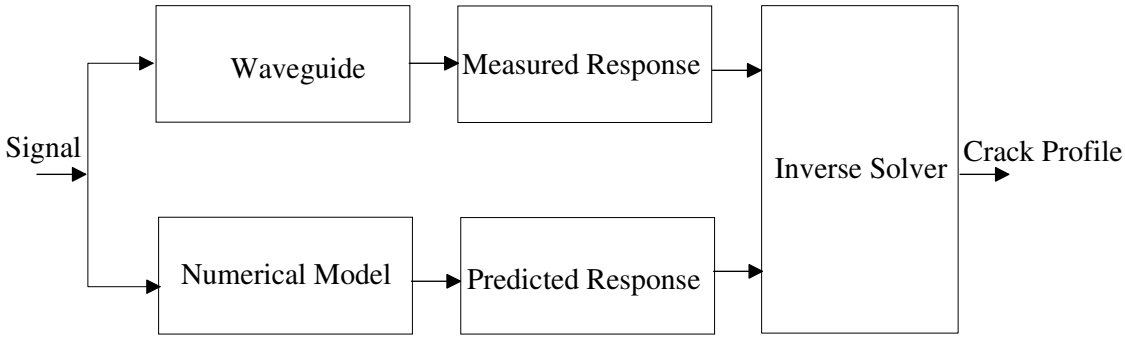

Figure 1.2 A schematic structural health monitoring setup using guided elastic waves

In the field of elastic-wave NDI, the status of affairs is no different. Numerical elastic-wave modeling plays a vital role in elastic-wave NDI for the following reasons. Numerical elastic-wave modeling represents an integral part of any structural health monitoring setup using guided elastic waves [9], see Figure 1.2 In the setup, understanding the forward problem of elastic-wave scattering through numerical modeling is the first step towards solving the inverse problem of identifying scatterers [10]. For example, the results of numerical elastic-wave modeling can train an artificial neural network (ANN) to solve the inverse problem or even solve other intractable forward problems [11-15]. Last but not least, numerical elastic-wave modeling has been very helpful in all phases of advancing new elastic-wave NDI methods [16, 17].

Nnumerical methods are used in the field of elastic waves to model: 1) free waves in a flawless waveguide; 2) the impulsive response of a flawless waveguide (Green's function); or 3) the interaction of elastic waves with flaws in a waveguide (scattering problems).

1.3 Free Guided Elastic Waves

In 1972, Dong and Nelson [18] have proposed the implementation of an approximate Rayleigh-Ritz based stiffness method (1D finite element through the plate's thickness) to study natural vibrations and waves in laminated orthotropic plates. It has been shown that Dong's method is accurate and numerically efficient over a broad range of frequencies [19], and for any type of anisotropy [20]. Kausel [21], and Kausel and Roësset [22] have implemented a stiffness method that is similar to Dong's method to anisotropic wave propagation in laminated soil. Liu et al. [23] have extended Dong's method to study the effect of anisotropy on the speed of energy transmission in hybrid composite plates. Rattanawangcharoen et al. [24] have employed a displacement-based Rayleigh-Ritz approximation method, similar to Dong's method, to obtain initial guesses for numerical solution of 3D dispersive relation derived through a propagator matrix method. Pan et al. [25] followed the same approach as in [24] to investigate the effect of a viscoelastic coating on modal dispersion in a steel plate. Onipede and Dong has extended Dong's method to study 3D dispersion of guided elastic waves in rectangular cross-section infinite plates [26]. It is worth mentioning that dispersion properties can be obtained by using 2D-FFT

[27, 28] or Time Frequency Representations (TFRs) [29-31] of computed time histories or laser-measured signals.

1.4 Elastodynamic Green's Function

Elastodynamic Green's function is an indispensable ingredient in the boundary element method (BEM) [32]. It is also needed for inverse identification of impact loads [33]. Numerical evaluation of 2D elastodynamic Green's function using a combined finite element method (FEM) and normal mode expansion (NME) technique was reported by Zhu et al. [34] and Pan et al [35]. Extending this method to 3D problems involved the use of numerical integration [36-39] or Cauchy residue theorem [40-42] to perform spatial Fourier transformation. The use of pure FEM to compute elastodynamic Green's function in 2D and 3D was also reported [43, 44]. The computational time consumed by the FEM was a burden especially in 3D.

1.5 Modeling Elastic Wave Scattering

There are several numerical methods to model guided elastic wave scattering. These methods include: the finite element method (FEM), the spectral finite element method (SFEM), the finite difference method (FDM), the BEM, the strip element method (SEM), the elastodynamic finite integration technique (EFIT), and the mass spring lattice model (MSLM). The most frequently used numerical method in modeling guided elastic wave

propagation and scattering is the FEM. The use of FEM in elastic-wave modeling can be sorted under two main categories: pure or hybrid. Pure usage of FEM can be through numerical implementations or commercial software packages.

1.5.1 Pure FEM Implementations

Examples of pure implementation of the conventional *h*-version FEM are the works of Ludwig and Lord, You et al., Alleyne and Cawley, Alleyne et al., and Tang and Cheng. Ludwig and Lord reported the use of transient FEA to simulate ultrasonic non-destructive testing (NDT) processes [45]. This approach has been followed by You et al. to study ultrasonic attenuation in viscoelastic solids [46]. Alleyne and Cawley studied the interaction of ultrasonic pulses with rectangular surface defects in plates under plane-strain conditions following the same approach [47]. Alleyne et al. and Lowe et al. investigated reflection and mode conversion of guided elastic waves from circumferential notches in steel pipes using a 3D membrane FEM [48, 49]. Tang and Cheng have compared the total waveform of laser-generated longitudinal modes in a hollow cylinder simulated by NME to FEM predictions concluding a good agreement [50]. The use of other FEM versions has also been reported [51-53]. Issa et al. reported the use of a *p*-version FEM to model elastic wave propagation and scattering [51]. In a *p*-version FEM, the polynomial order of the interpolation functions can be increased in order to achieve convergence. The use of partition of unity FEM (PUFEM) and a particular instance of it known as the extended FEM (XFEM) to model guided elastic wave propagation and scattering has been reported

[52, 53]. Hu et al. have reported the use of PUFEM to model elastic wave propagation in Reissner-Mindlin plates [52]. Recently, Rabinovich et al. have developed a computational framework, in which an XFEM and a genetic algorithm are used to investigate the detectability of small cracks in 2D structures using arrival time [53].

1.5.2 Commercial FE Packages

In addition to the numerical implementations, the use of FEM through commercial software packages has also been reported [54-63]. Moser et al. investigated the use a commercial FEM code in modeling plate and thick-ring structures by validating FEM results against optically-measured data and predictions made by NME [54]. They considered meshing and post-processing capabilities the real advantages of commercial FE packages. Zhu used an FEM package to simulate the generation and reflection of guided elastic waves in a finite-length steel pipe having corrosion defects [55]. Zerwer et al. reported the use of ABAQUS, a commercially available FEM package, to model 2D Rayleigh wave scattering from near-surface discontinuities in isotropic plates [56]. Bartoli et al. demonstrated the use of ABAQUS/Explicit, to model guided elastic wave scattering of broad-band vertical bending mode from transverse-type defects in railroad tracks [57]. Jeong and Park employed ANSYS, another commercially available FEM package, to model propagation and interaction of laser generated ultrasound [58]. Chong has also used ABAQUS/Explicit to simulate elastic wave scattering from several types of defects along with shelling in rail head [59]. Erdem reported the use of ABAQUS in FEM simu-

lation of guided elastic wave scattering in cracked graphite rods; results were successfully corroborated with experimental measurements [60]. Protopappas et al. reported to use of ABAQUS in 3D FEM of guided elastic wave propagation in intact and healing long bones [61]. Baskaran et al. used ANSYS to simulate 2D Time-of-Flight Diffraction (TOFD) of guided elastic waves in thin structural waveguides in order to help select optimal parameters in TOFD measurements [62]. Very recently, Ke et al. reported the use of a commercial FEM code in 3D modeling of an air-coupled ultrasonic NDT system [63].

1.5.3 Hybrid FE Implementations

The most popular, hybrid approach of implementing the FEM is the so-called global-local FEM (GLFEM), semi-analytical finite element (SAFE), or the hybrid method. The latter term will be used throughout this thesis to refer to this technique. The hybrid method is a technique that combines a finite-element (FE) idealization of a bounded region containing the crack (or inhomogeneity) and a wave function expansion in the exterior region. Continuity conditions of displacements and interactive forces are applied at discrete points on the common boundaries between the two regions. This procedure results in a system of linear equations in the unknown wave function amplitudes. These amplitudes are used to obtain the reflection and transmission coefficients of an incident wave.

The use of the hybrid method may date as early back as to 1969 when Lysmer and Kuhlemeyer [64] approximated an infinite half space by a finite model whose convex boundary was supported on infinitesimal dashpots oriented normal and tangential to the boundary. They analyzed the response of this model to spatially limited harmonic excitations by utilizing the FEM. Lysmer also reported a dispersion study [65] of free Rayleigh waves in an infinite layered medium. The layered medium was divided across its thickness into a finite number of infinite sub-layers that are, indeed, 1D finite elements. This discretization led to a generalized eigenvalue problem that was solved, at each frequency, for the eigenvalues (wavenumbers) and the corresponding eigenfunctions (mode shapes). Later, Lysmer and Waas modeled a layered, plane, infinite structure that contained geometric irregularities and rested on a rigid base by dividing it into three regions: a bounded region containing the irregularities and two (left and right) semi-infinite regions joined to the bounded region along vertical boundaries [66]. They idealized the bounded region with finite elements and used 1D finite elements (identical to those reported earlier for Rayleigh waves) to represent free Love waves in the semi-infinite regions. It should be noted that a similar approach to the hybrid method was also used by electrical engineers in the 1970s to investigate the scattering of electromagnetic waves [67-69]. Datta et al. were able to apply the hybrid method to the field of elastic waves in their study of diffraction of horizontally-polarized shear (SH) waves by edge cracks in a half-space [70]. Angelov and Ivanov reported the use of the hybrid method in analyzing transient pressure, shear-vertical (PSV) waves excited by line loads in semi-infinite isotropic media

[71]. The first application to waveguides was made in 1982 by Abduljabbar et al. in a study of the scattering of SH waves by a symmetric crack in a plate [72]. The hybrid method has been since used to model the scattering of Lamb waves by cracks [73, 74] and weldments [75]. It has been also used to study plane-strain wave scattering by surface breaking crack in transversely isotropic plates [76]. More recently, the hybrid method was reported in a study of Lamb wave interaction with delamination in carbon fibre reinforced plastic (CFRP) laminates [77]. In the case of a horizontal crack the SEM can be used instead of the FEM in order to reduce computational cost. An example of this approach was reported by Liu and Lam [78]. The hybrid method has been also used to study 2D wave scattering in a cylinder containing an inhomogeneous region, a crack, and/or a weldment [79, 80]. Implementation of the hybrid method in 3D was reported for plates by Zensheu and Mal [81] and for cylinder by Mahmoud et al. [82]. It should be made clear at this point, that the hybrid method introduces an Absorbing Boundary Condition (ABC) by forcing displacement and force continuity at the interface between the finite and infinite regions. Theoretically, these ABCs are exact.

Another form of combining the FEM with NME was reported in the context of modeling plate waveguides with integrated piezoelectric transducers. Moulin et al. have introduced the use of FEM to model an infinite composite plate with an integrated piezoelectric transducer. The mechanical field created by the piezoelectric transducer was computed from the FEM model and then introduced as a forcing function into the NME equations [83]. This approach was followed by Grondel et al. in studying the influence of piezoce-

ramic transducer characteristics on Lamb waves for the purpose of designing a dual piezoelectric transducer that is capable of exciting the A_0 Lamb mode in composite plates [16]. This technique has been successfully used by Hu et al. to locate damage in metallic structures [17].

1.5.4 Spectral Finite Element Method

The SFEM is a high-order FEM that combines the flexibility of FEM and the high accuracy of spectral methods. The SFEM is based on exact solution of a polynomial eigenvalue problem of free waves (the dispersion equation) whereby exact solutions (the mode shapes) are employed as element interpolation functions. This yields exact stiffness and mass matrices. Hence a problem can be represented by fewer elements than standard FE formulation. In fact one spectral finite element can be used across the thickness of a composite plate compared to several finite elements needed in a corresponding FE idealization. Thus, SFEM offers great saving in computational cost if compared to similar frequency-domain FE formulation.

There are two SFEM approaches: an FFT-based approach [84] and an orthogonal-polynomial-based approach [85]. The former approach is more efficient with simple 1D and 2D problems. The latter approach is more suitable for problems with complex geometry and for those in 3D. Kumar et al. employed a frequency-domain, spectral finite element with embedded transverse crack to simulate various cracks in a composite beam [86]. Wang et al. developed a concrete-steel interface spectral element to study guided

wave propagation along the steel rebar in reinforced concrete [87]. Palacz et al. followed an FFT-based SFEM approach to model flexural-shear coupled wave propagation in laminated and delaminated multilayer composite beams [88, 89]. Chakraborty and Gopalakrishnan developed a spectral plate element to analyze wave propagation in laminated composite media following an orthogonal-polynomial-based SFEM approach [90]. Recently, Zak has adopted an orthogonal-polynomial-based SFEM to analyze elastic waves in isotropic plate structures, wherein a spectral plate finite element was formulated [91]. A recent account of the history of SFEM can be found in [92].

1.5.5 Finite Difference Method

The FDM solves elastodynamic wave equations by replacing the derivatives in space and time with their finite-difference approximations. For discretization in space of a spatially varying material, two basic difference schemes are used: the homogeneous and the heterogeneous. For discretization in time, the explicit scheme is the most common. In the explicit scheme, the wavefield is updated over the entire grid at each time step. Implicit schemes involve matrix inversion to update the wavefield at each time step; they are, therefore, less common. Examples of using the FDM in modeling elastic wave scattering by cracks are the works of Harker [93], Scandrett and Achenbach [94], and Wu and Chong [95]. Probably, one of the earliest attempts to apply the FDM to guided elastic wave scattering is the work of Harker. Harker applied the FDM to elastic scattering of Lamb waves in cracked plates. He demonstrated the potential of the FDM in modelling

NDI system. Scandrett and Achenbach employed the FDM to simulate ultrasonic inspection of inner-surface breaking cracks, where time-domain signal and snapshots of displacement were presented. Wu and Chong employed a heterogeneous FDM with staggered grid to study impact induced transient elastic waves in plates with surface-breaking cracks. Implementations of finite difference time domain (FDTD) method combined with the perfectly matched layer (PML) have been frequently reported in modeling bulk elastic wave propagation and scattering in infinite media for NDI [96-99]. Also the use of commercially available FDM software packages is not uncommon [100].

1.5.6 Boundary Element Method

Time-harmonic elastodynamic BEM formulation is derived by applying Green's reciprocal identity (GRI) to wave partial differential equation (PDE). This identity converts a volume (domain) integral to a surface (boundary) integral, therefore, comes the often-used name boundary integral equation method (BIEM). This reduction in dimensions is a significant advantage over domain-type approaches like the FEM and the FDM. Another important feature of BEM is the rigorous treatment of the Sommerfeld radiation condition for an unbounded medium. However, BEM has been broadly used in solving various bulk wave scattering problems compared to very few studies of guided elastic wave scattering [101]. Of those studies is the 2D study by Cho and Rose of modal conversion at the edge of a semi-infinite plate [102]. They also reported another study of the interaction of Lamb waves with surface breaking cracks in a plate [103]. However, there are few BEM studies

of 3D bulk wave scattering, to the best of the author's knowledge BEM has not been yet used to study guided elastic wave scattering in 3D. It should be noted that BEM could play the same role of the FEM in the hybrid method [104-108]. In this case, the hybrid method was sometimes referred to as the hybrid FE-BE method, since the exterior region is modeled by 1D finite elements (or sub-layers) [106-108].

1.5.7 Strip Element Method

The strip element is a 1D finite element that is infinite always in one direction and can be finite or infinite in the other two directions. This element is ideal for modeling unbounded stratified media and layered guides. A strip element that is finite in one direction and infinite in the other two directions is, in fact, an infinite layer or a sub-layer. It is sometimes referred to by this term in the literature. Infinite strip elements are the same as the sub-layers used by Dong and others to analyze free wave dispersion in laminated plate and cylindrical structures [18-26]. Liu and Achenbach have employed the SEM in analyzing scattering of plane-strain elastic waves in anisotropic laminated plates [109].

1.5.8 Elastodynamic Finite Integration Technique

The EFIT starts with elastodynamic governing equation in integral form. In this technique the spatial discretization is done by integrating the differential equations over a control volume or cell. Temporal discretization in time is done through a second-order central difference scheme [110].

1.5.9 Mass Spring Lattice Model

The MSLM [111] can be used to simulate and visualize ultrasonic wave propagation and interaction with cracks. In the MSLM, the inertia of the medium is modeled by lumped masses interconnected together by stiffness that is expressed by finite difference.

1.6 ABCs and the PML

As it has been pointed out earlier, the hybrid method introduces an exact set of ABCs. Another category of ABCs is represented, for example, by the work of Clayton and Enguist [112]. In this category, the wave equation in the boundary region is replaced by a one-way wave equation that does not permit the energy to propagate back from the boundaries into the numerical domain. The technique was applied successfully to acoustic and elastic waves striking a rigid boundary at a small angle of incidence. At large angle of incidence, these boundary conditions become numerically unstable and inefficient. To overcome this problem, Higdon proposed a combination of first order boundary conditions [113]. Givoli et al., on the other hand, presented a higher-order, Higdon-based technique for wave propagation in semi-infinite, time-dependent waveguides [114]. The idea of absorbing outgoing waves by exponentially reducing wave amplitudes in time (i.e. damping) inside a boundary strip surrounding the computational domain of interest was proposed first by Cerjan et al. [115]. They employed a Fourier method for analyzing acoustic and elastic waves to demonstrate the idea. Moreover, the wave amplitudes were

reduced at discrete nodes without reformulating the governing equations of motion. Twenty discrete nodes were needed to reduce reflection coefficients to a few percent. Sochacki et al. [116] introduced Cerjan's idea to 2D equations governing acoustic and elastic wave propagation. In addition to the exponential damping used by Cerjan, they investigated other dampers and indicated how an optimal damper can be chosen. Moulin et al. introduced the use of an attenuating layer to FEM simulation of an infinite composite plate with an integrated piezoelectric transducer. Each attenuating material constant contained a non-zero imaginary part that accounts for attenuation [83]. Following a gradual-damping approach, Liu and Quek Jerry recently studied Lamb wave propagation in an infinitely-long plate by exponentially increasing damping in a boundary layer [117]. Ziemianski proposed the novel use of ANN to formulate a transmitting boundary in modeling elastic wave propagation in infinite domain with FEM [118].

A PML whose interface with the computational domain does not return any reflection at any frequency or angle of incidence, was first introduced by Berenger [119] to solve Maxwell's equation in computational electromagnetics (CEM) using an FDTD method. Chew and Weedon [120] interpreted the PML as a complex coordinate stretching. This interpretation widely inspired researchers to apply the PML to other disciplines. Hastings et al. introduced the PML to PSV elastic wave propagation in an infinite medium [121]. They employed the FDTD method to formulate a PML for the stress-velocity equations in the form of compressional and shear potentials. Chew and Liu showed the feasibility and stability of the PML solutions for 2D and 3D stress-velocity, elastodynamic equa-

tions in isotropic elastic media [122]. Liu formulated PMLs for elastic wave propagation in polar and cylindrical coordinates [123]. Liu introduced integral complex coordinate stretching to keep the number of unknowns in the formulation the same as that for Cartesian coordinates. Collino and Tsogka applied the PML to a linear elastodynamic problem in anisotropic heterogeneous media using FDTD [124]. They reported a 1% (artificial) reflection coefficient for a layer thickness corresponding to five FDTD space steps. These numbers indicate the relatively better computational efficiency of the PML compared to the damping layer used in [115, 116]. Becache et al. used the PML with a mixed FEM and FDTD to overcome the inadequacy of the latter for irregular geometries [125]. Komatitsch and Tromp introduced a time-domain formulation of the PML boundary condition for the second-order, seismic wave equation that is amenable to explicit Newmark time integration [126]. A spectral element method is used to implement this formulation to solve PSV problems in infinite elastic media. Good agreement was reported with previous results. In two consecutive papers, Basu and Chopra reported steady-state and time-domain formulations of 2D (anti-plane and plane-strain) elastodynamic problems in an infinite layer resting on a semi-infinite elastic media [127,128]. Unlike the research in [125], the time integration in [128] was implicit and a system of equations was solved at each time step. Just recently, Basu extended the work in [128] to 3D and made it amenable to explicit time integration by lumping inertial matrices inside the PML [129]. Studies in [118-129] employed a split-field technique to formulate time-domain, perfectly

matched layers to avoid convolution in time. A non-splitting formulation was reported by Wang and Tang [130].

1.7 Scope and Significance

The objective of this thesis is to *introduce the use of the PML in combination with the FEM to the numerical modeling of guided elastic wave propagation and scattering by defects in infinite plates, beams, and cylinders*. The purpose of this thesis is to numerically investigate the feasibility of using the PML in elastic wave modeling as it relates to ultrasonic NDT rather than to break new ground in the mathematical theory of ABCs. The plates, beams, and cylinders are assumed isotropic. Only the special anisotropic case of transverse isotropy is considered. General anisotropy is outside the scope of this thesis. To the best of the author's knowledge no such investigation has been yet reported in the open literature.

Some capabilities of FE-PML modeling become very clear when the technique is contrasted to the hybrid method. The latter gives us the understanding of wave propagation and interaction with flaws on the steady-state, single-mode level. However, the only way to produce real-life transient time histories is to use Fourier-transform inversion. On the other hand, the FE-PML can be formulated directly in the time domain.

Computational time effectiveness of FE-PML modeling can be magnified by comparing it against standard FEA of 3D elastic wave modeling. In this particular case, the computational cost is proportional to the fourth power of frequency (three from dependence of

element size on wave length and one from time/frequency discretization). Despite the increasing size of available computer memory and speed running 3D FE codes is still a burden. The proposed FE-PML significantly reduces mesh size by replacing a big part of the mesh with small-size absorbing layers.

Finite Element Analysis of Guided Elastic Waves (FEAGEW) computer code is the soft outcome of the current research work. The program can simulate wave propagation and scattering in, infinite (or finite), plates and cylinders. However, the scope of this thesis is restricted to plates and cylinders, FEAGEW can be, ultimately, used to simulate any elastic waveguide of arbitrary cross-sectional shape. Based on the reported successes in the literature, transient time histories from FEAGEW can be used to obtain waveguide dispersion properties using TFRs.

1.8 Thesis Outline

This section presents an overview of the thesis overall picture. It explains the chapters sequence and how each chapter contributes to the fulfillment of the aforementioned objectives. Basic principles of the PML and the FEM are presented in Chapter 2 by working out the details of a combined FE-PML model for the simple case of longitudinal wave propagation in a semi-infinite slender rod. Both frequency- and time-domain formulations of the model are given.

The feasibility of using the FE-PML model to predict elastic wave propagation and scattering behaviours in infinite plates is investigated in Chapter 3. The simple case of SH

waves in an infinite, isotropic plate is considered in both frequency and time domains. In Chapter 4, the results from the FE-PML model is validated against literature data and confirmed through a reciprocity check. Conclusions drawn from a numerical study of 2D elastic wave scattering in a cracked plate using the FE-PML model agreed with reported experimental findings.

The most practical situation of 3D wave propagation and scattering in plates and cylinders is covered in Chapters 5 and 6, respectively. Chapter 5 presents the FE-PML formulation in Cartesian coordinates for wave propagation and scattering in infinite rectangular-cross-section plates and beams. Example applications to elastic scattering in cracked concrete beams were given.

In Chapters 6, the FE-PML is formulated within a cylindrical coordinate frame. Numerical implementations are validated and several applications to NDI of oil and gas pipelines and composite cylindrical shells are presented. Chapter 7 summarizes overall conclusions and establish a vision for future development directions.

"*As far as laws of mathematics refer to reality, they are not certain; and as far as they are certain, they do not refer to reality*" Albert Einstein (1879-1955)

Chapter 2

Fundamentals

2.1 Introduction

The two major ingredients of the numerical modeling technique proposed in this thesis are the PML and the FEM. This chapter presents the foundations of each tool by using the scalar equation of longitudinal elastic wave motion in a semi-infinite slender rod as a simple illustrative example. First, the two basic concepts behind the PML will be introduced: impedance matching and complex coordinate transformation or stretching. While wave motion inside the computational domain will be governed by the standard, scalar wave equation, the equation is altered inside the PML region by a complex coordinate stretching along the infinite propagation direction. In order to use the PML with the FEM, one has to formulate the transformed equation inside the PML region within the FEM framework. Starting with the PDE of steady-state wave motion, a Galerkin method, which is a special variant of the method of weighted residuals (MWR), is employed to

reach a combined FE-PML formulation in the frequency domain. Time-domain, FE-PML formulation involves the following steps: 1) the displacement wavefield in a displacement-based PDE of steady-state wave motion inside the PML is split into two parts resulting in two PDEs; 2) the two PDEs are inverse Fourier transformed back into the time domain; 3) FE equations are formulated using the Galerkin method; 4) at last, a central-difference integration scheme and Euler's method are utilized to march through time steps.

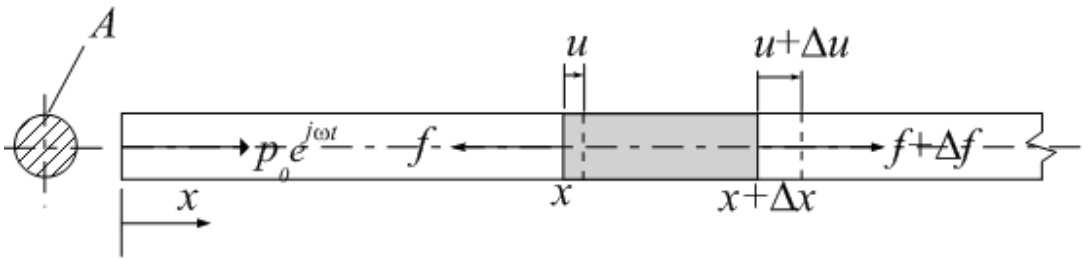

Figure 2.1 An infinitesimal element of a slender rod undergoing a longitudinal wave motion.

2.2 Longitudinal Waves in a Slender Rod

Let us consider the problem of longitudinal, elastic wave propagation in a semi-infinite, isotropic, slender rod. Transverse wave motion, coupled to longitudinal one by Poisson's ratio, ν, can be neglected based on rod slenderness. The rod is assumed to have a constant cross-sectional area, A, uniform mass density, ρ, and a Young's modulus, E. Consider an infinitesimal element of the rod extending between x and $x+\Delta x$ as shown in Figure 2.1. Net positive force acting on the element accelerates its mass according to

Newton's second law leading to the equilibrium equation expressed in terms of axial stress $\sigma = f/A$ as follows:

$$\sigma_{,x} = \rho \ddot{u}. \tag{2.1}$$

A double over-dot denotes second-order differentiation with respect to time. Axial stress σ is related to axial strain $u_{,x}$ through Hooke's law as follows:

$$\sigma = E u_{,x}. \tag{2.2}$$

Substituting Equation (2.2) into (2.1) results in:

$$u_{,xx} = \frac{1}{c^2} \ddot{u}. \tag{2.3}$$

Bar wavespeed, c , is defined as:

$$c = \sqrt{\frac{E}{\rho}}. \tag{2.4}$$

Equation (2.3) admits a steady-state propagating solution in the following closed-form:

$$u = u_0 e^{-j\xi(x-ct)}, \tag{2.5}$$

whose real part is given by

$$u = u_0 \cos\left[\xi\left(x - ct\right)\right]. \tag{2.6}$$

The bar wavespeed, c, in Equations (2.5) and (2.6) is expressed in terms of ω and ξ as follow:

$$c = \frac{\omega}{\xi}. \tag{2.7}$$

If a numerical solution to the PDE in (2.3) is sought, the problem domain has to be truncated due to limited computational resources (memory and CPU time). This truncation will results in unphysical reflection, $\hat{u}$, from the artificial boundary introduced by the confined computational domain. Let us assume that the computational domain is terminated by a rigid boundary at $x = L$ such that the following Dirichlet boundary condition applies:

$$u + \hat{u}\big|_{x=L} = 0. \tag{2.8}$$

A reflected wave, $\hat{u}$, travelling in the negative *x*- direction can be written as

$$\hat{u} = \hat{u}_0 e^{j\xi(x+ct)}. \tag{2.9}$$

Substituting Equations (2.5) and (2.9) into Equation (2.8) results in

$$R_a = \frac{u_0 e^{-j\xi L}}{\hat{u}_0 e^{j\xi L}} = -1. \tag{2.10}$$

The amplitude reflection coefficient, R_a, in (2.10) quantifies the intuitive fact that the entire wave will reflect back into the computational domain. R_a can be formulated in terms of the characteristic impedance of the rod that is analogous to the resistivity of an electrical conductor with the force, f, and velocity, $\dot{u}$ being analogous to potential and current, respectively. Let us consider a sinusoidal, tensile force applied to the rod at the origin as shown in Figure 2.1.

$$f\big|_{x=0} = p_0 e^{j\omega t}. \tag{2.11}$$

This force will excite a longitudinal wave motion in the rod that can be described by Equation (2.5). By definition, the force in the rod is given by

$$f = AEu_{,x}. \tag{2.12}$$

Substituting Equation (2.5) into Equation (2.12) and the result into Equation (2.11) will determine the unknown displacement amplitude, u_0. Thus, the displacement wavefield excited by the force in Equation (2.11) can be written as

$$u = \frac{jp_0}{AE\xi} e^{-j\xi(x-ct)}. \tag{2.13}$$

Differentiating Equation (2.13) with respective to time yields the corresponding velocity wavefield in the bar as

$$\dot{u} = -\frac{p_0\omega}{AE\xi} e^{-j\xi(x-ct)}. \tag{2.14}$$

A single over-dot denotes first order differentiation with respect to time. Therefore, the characteristic impedance of the rod is the ratio between the amplitude of force to the amplitude of velocity, i.e.

$$Z_0 = \frac{|f|}{|\dot{u}|} = \frac{AE}{c} = A\sqrt{\rho E}. \tag{2.15}$$

As we have shown earlier, if the rod is terminated by a rigid boundary at $x = L$, both positive wave, Equation (2.5), and negative-going wave, Equation (2.9), exist in the domain. In this case the impedance at any x is given by

$$Z = \frac{f + \widehat{f}}{\dot{u} + \widehat{\dot{u}}} = Z_0 \frac{\widehat{u}_0 e^{j\xi x} - u_0 e^{-j\xi x}}{\widehat{u}_0 e^{j\xi x} + u_0 e^{-j\xi x}}. \tag{2.16}$$

Therefore the impedance of the rigid boundary at $x = L$

$$Z_L = Z_0 \frac{\hat{u}_0 e^{j\xi L} - u_0 e^{-j\xi L}}{\hat{u}_0 e^{j\xi L} + u_0 e^{-j\xi L}}. \tag{2.17}$$

We can now use Equation (2.17) to express the amplitude reflection coefficient in terms of impedance as follows

$$R_a = \frac{\hat{u}_0 e^{j\xi L}}{u_0 e^{-j\xi L}} = \frac{\frac{Z_0}{Z_L} + 1}{\frac{Z_0}{Z_L} - 1}. \tag{2.18}$$

As we can see, a rigid boundary introduces infinite impedance at $x = L$. On the other hand, a matching impedance at $x = L$ will cause no reflection. This brings us to the notion of a PML.

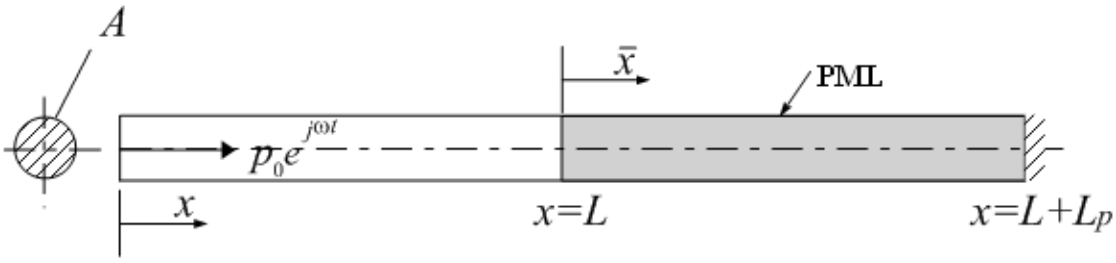

Figure 2.2 An artificial damping layer is attached to the truncated computational domain at termination boundary, $x = L$

2.3 Complex Coordinate Stretching

In a PML, a non- physical damping layer is introduced at the termination boundary of a computational domain, see Figure 2.2.

The real x-axis is mapped into the complex domain by what is known in the PML literature as complex coordinate stretching that is defined as [131]

$$\bar{x} = \int_{s=0}^{s=x} \zeta(s)\, ds. \tag{2.19}$$

Coordinate stretching function, ζ, can be written as a function of frequency and an always-positive damping profile, $d(x)$, that vanishes within the computational domain and gradually increases within the damping layer as follows:

$$\zeta(x) = 1 \quad x \le L, \tag{2.20}$$

$$\zeta(x) = 1 + \frac{d(x)}{j\omega} \quad L < x \le L + L_P. \tag{2.21}$$

According to Equations (2.20) and (2.21), the imaginary part of the complex x-coordinate, $\bar{x}$, assumes a nonzero value only within the damping layer ($L < x \le L + L_P$) and vanishes within the computational domain of interest ($x \le L$). Furthermore, The damping profile, $d(x)$, can be real or complex. A real damping profile can dampen propagating modes only. A complex damping profile can dampen both propagating and evanescent modes. In this section, a real damping profile is assumed. Introducing the complex coordinate, $\bar{x}$, into the steady-state solution in Equation (2.5) will yield the following steady-state solution inside the PML region:

$$u = u_0 e^{-\frac{\int_{s=L}^{s=x} d(s)ds}{c}} e^{-j\xi(x-ct)}. \tag{2.22}$$

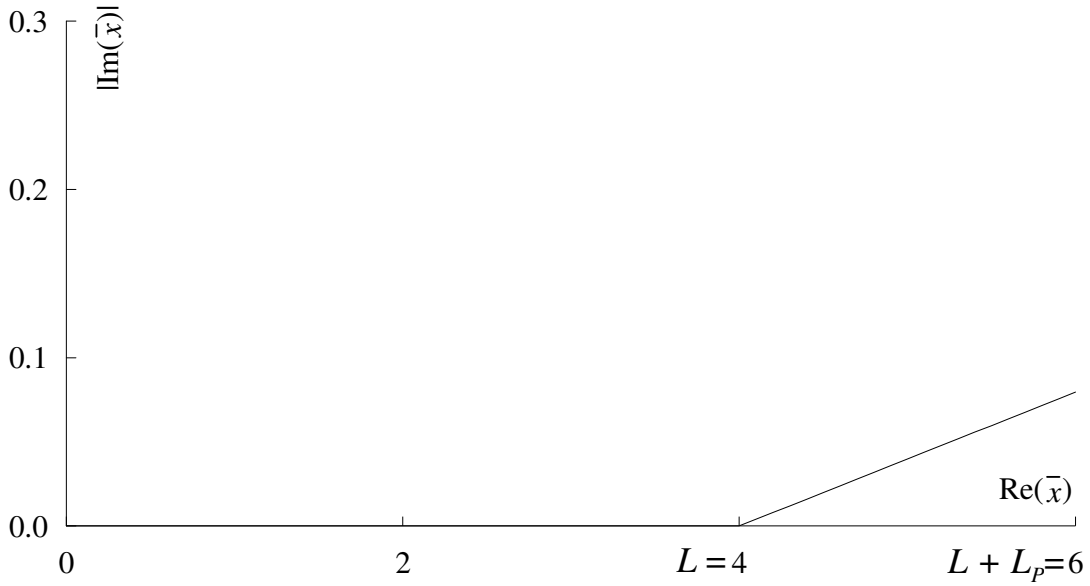

Figure 2.3 Stretched complex coordinate, $\bar{x}$, in the complex plane

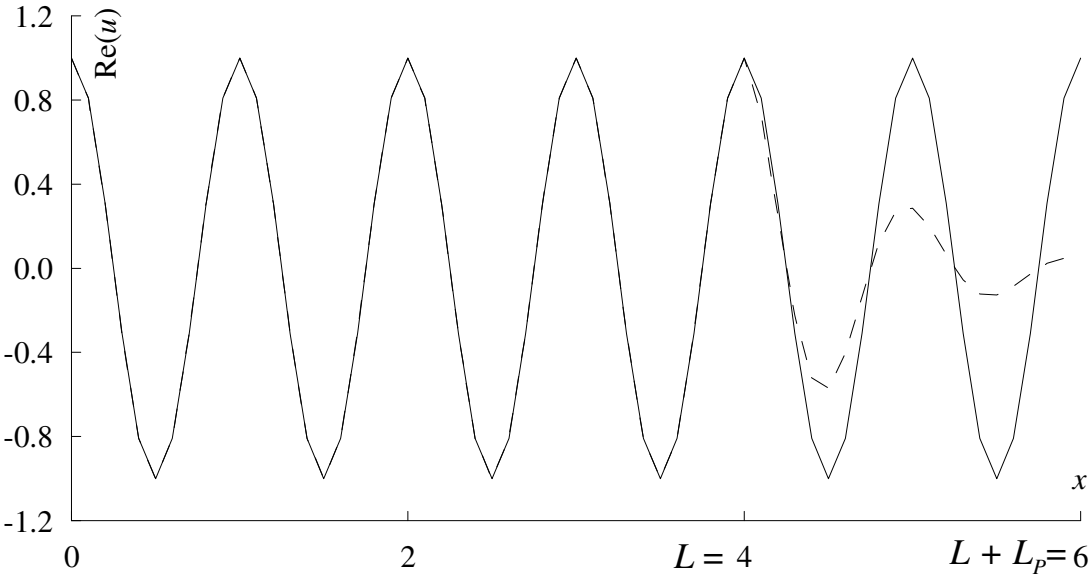

Figure 2.4 Real part of steady-state harmonic solution in the infinite physical domain (continuous) and the truncated domain with a PML (dashed)

Thus, the real part of the solution inside the PML region is

$$u = u_0 e^{-\frac{\int_{s=L}^{s=x} d(s)ds}{c}} \cos\left[\xi\left(x - ct\right)\right]. \tag{2.23}$$

Figure 2.3 shows the mapping of the coordinate x-axis into the complex plane inside a PML with a constant damping profile, $d = 0.25$, and $\omega = 2\pi$. A plot of the wave amplitudes in Equations (2.6) and Equation (2.23) versus x, for $u_0 = 1$, $d = 0.25$, $\omega = 2\pi$, and $\xi = 2\pi$ are shown in Figures 2.4. It is evident that complex coordinate stretching dampens the wave amplitude such that amplitude reflections at model boundaries are insignificant.

2.4 Governing PML Equations

Equilibrium equation and constituent relation inside the PML can be obtained from Equations (2.1) and (2.2), respectively, by replacing x with $\bar{x}$ such that

$$\sigma_{,\bar{x}} = \rho \ddot{u}, \tag{2.24}$$

$$\sigma = E u_{,\bar{x}}. \tag{2.25}$$

From Equation (2.19) we can write

$$\frac{\partial}{\partial \bar{x}} = \frac{1}{\zeta}\frac{\partial}{\partial x}. \tag{2.26}$$

Substituting Equation (2.26) into Equations (2.24) and (2.25) yields

$$\sigma_{,x} = \zeta \rho \ddot{u}, \tag{2.27}$$

$$\sigma = \frac{E}{\zeta} u_{,x}. \tag{2.28}$$

Thus, steady-state equilibrium inside the PML is governed by:

$$\sigma_{,x} = -\zeta \rho \omega^2 u. \tag{2.29}$$

Equation (2.29) is subject to the following steady-state boundary conditions

$$u\big|_{x=L+L_P} = 0, \quad \text{(Dirichlet boundary condition)} \tag{2.30}$$

$$\sigma\big|_{x=0} = p_0. \quad \text{(Neumann boundary condition)} \tag{2.31}$$

2.5 Frequency-domain FE-PML Formulation

Let us seek an approximation, $\tilde{u}(x)$, to the unknown displacement solution, $u(x)$, in terms of discrete values, $Q_l = u(x_l)$ $(l = 1,...,n_n)$, and prescribed (interpolation) basis functions, N_l $(l = 0,1,...,n_n)$ as follows

$$\tilde{u} = N_0 + \sum_{l=1}^{n_n} N_l Q_l, \tag{2.32}$$

Where n_n is the number of discrete points (or nodes) in the problem domain. The function N_0 should satisfy the prescribed Dirichlet boundary condition, i.e.

$$N_0 = u\big|_{x=L+L_P} = 0. \tag{2.33}$$

Thus, approximation $\tilde{u}$ becomes

$$\tilde{u} = \sum_{l=1}^{n_n} N_l Q_l. \tag{2.34}$$

An approximation, $\tilde{\sigma}$, to the unknown stress solution, σ, should follow from Equation (2.28) as

$$\tilde{\sigma} = \frac{E}{\zeta} \sum_{l=1}^{n_n} N_{l,x} Q_l. \tag{2.35}$$

Substituting approximate solutions, $\tilde{\sigma}$ and $\tilde{u}$, into Equation (2.29) will yield, as a result of their approximate nature, the following error or residue, $R(x)$:

$$R(x) = \tilde{\sigma}_{,x} + \zeta \rho \omega^2 \tilde{u}. \tag{2.36}$$

The residual, $R(x)$, is forced to be zero in an average sense by integrating the product of the residual, $R(x)$, by weight functions over the entire problem domain, $\Omega = [0, L + L_P]$. The number of weight functions is the same as the number of unknown discrete displacements, Q_l $(l = 1,..., n_n)$. So far, this procedure describes the well-known MWR. A special variant of MWR is Galerkin MWR, in which interpolation functions, N_k $(k = 1,..., n_n)$, are used as weight functions as well:

$$\int_{\Omega} N_k \left(\tilde{\sigma}_{,x} + \zeta \rho \omega^2 \tilde{u} \right) dx = 0; \qquad k = 1, 2, ..., n_n. \tag{2.37}$$

After expanding the differential term using integration by parts, Equation (2.37) becomes:

$$N_k \tilde{\sigma}\big|_0^{L+L_P} - \int_{\Omega} N_{k,x} \tilde{\sigma} dx = -\rho \omega^2 \int_{\Omega} N_k \zeta \tilde{u} dx; \qquad k = 1, 2, ..., n_n. \tag{2.38}$$

Substitute for Neumann boundary conditions from Equation (2.31) and for $\tilde{u}$ and $\tilde{\sigma}$ from Equations (2.34) and (2.35) into Equation (2.38) to get:

$$\int_{\Omega}\left[N_{k,x}\frac{E}{\zeta}\sum_{l=1}^{n_n}N_{l,x}Q_l-\rho\omega^2N_k\zeta\sum_{l=1}^{n_n}N_lQ_l\right]dx=-N_kp_0;\qquad k=1,2,...,n_n. \quad (2.39)$$

Exchange the sequence of integration and summation signs and factor out Q_l such that:

$$\sum_{l=1}^{n_n}\int_{\Omega}\left[N_{k,x}\frac{E}{\zeta}N_{l,x}-\rho\omega^2N_k\zeta N_l\right]dxQ_l=-N_kp_0;\qquad k=1,2,...,n_n. \quad (2.40)$$

It should be noted that the right-hand term contribute to the right-hand (load) vector only for $k=1$.

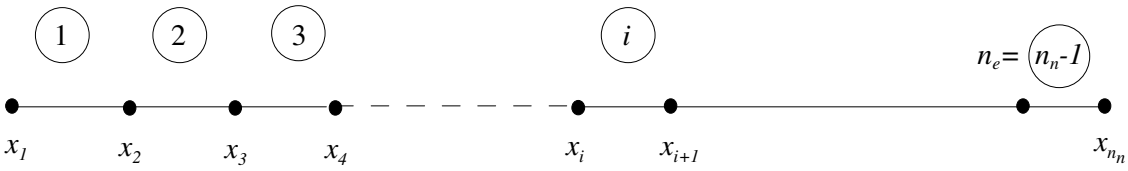

Figure 2.5 FE discretization in 1D using linear finite elements

2.6 Standard FE Procedure

In a standard FE procedure, the entire problem domain is divided into a finite number, n_e, of non-overlapping sub-domains (or elements), $\Omega_e^i=[x_i,x_{i+1}]$ $(i=1,...,n_n-1)$. Figure 2.5 shows the discretization of the domain, Ω, into $n_e=n_n-1$ linear, 1D elements; element numbers are circled. Each element, i, connect two global nodes, x_i and x_{i+1}.

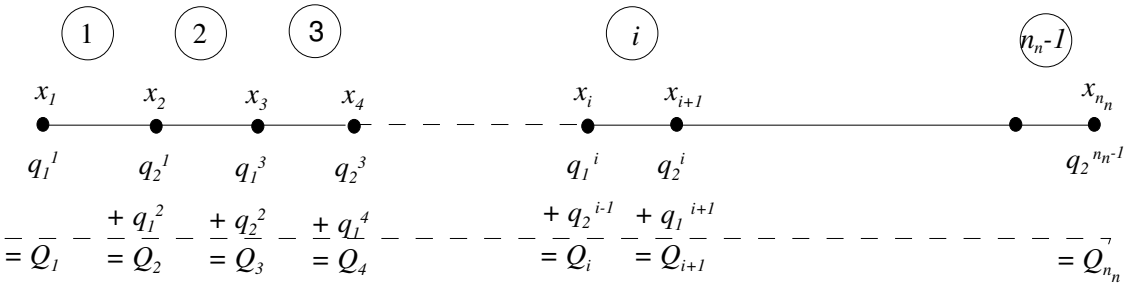

Figure 2.6 Connectivity between local and global nodal values of the solution

Equation (2.40) is integrated over each element domain rather on the entire problem domain. In so doing, global nodal values, Q_i, are defined in terms of local nodal values on each element domain. This is illustrated in Figure 2.6. Similarly, global basis functions are defined by piecewise-continuous and linearly-independent local shape functions, $n_k^i\left(i=1,...,n_n-1;\ k=1,2\right)$ as shown in Figure 2.7.

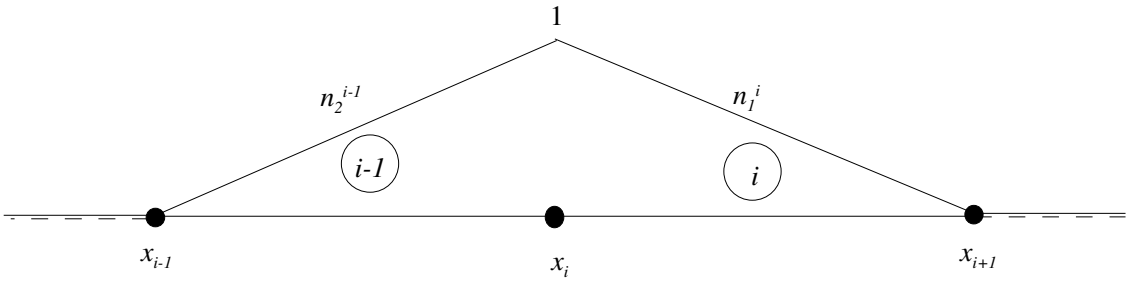

Figure 2.7 A plot of n_i as a combination of n_2^{i-1} and n_1^{i}

Local shape functions fulfill the condition:

$$n_k^i\left(x_l\right)=\begin{cases}1 & \text{for } k=l,\\ 0 & \text{for } k\neq l;\ k,l=1,2.\end{cases} \tag{2.41}$$

Approximate solution, $\tilde{u}^i$, over element domain, $\Omega_e^i = [x_i, x_{i+1}]$, can be formulated in terms of local shape functions, and local nodal variables, q_l^i, $(l = 1,2)$ as follows:

$$\tilde{u}^i = \sum_{l=1}^{2} n_l^i q_l^i. \tag{2.42}$$

Unlike the displacement wavefield, $\tilde{u}^i$, the damping profile, ζ, is not interpolated over each element domain. Rather it is evaluated globally during numerical integration of element contributions. Now, Equation (2.40) can be written after standard FE assembly of elemental contributions, denoted by Π, as follows

$$\prod_{i=1}^{n_n-1}\left\{\sum_{l=1}^{2}\int_{\Omega_e^i}\left[n_{k,x}^i\,\frac{E}{\zeta}n_{l,x}^i - \rho\omega^2 n_k^i\,\zeta\,n_l^i\right]q_l^i\,dx\right\} = -\prod_{i=1}^{n_n-1}\left\{n_k^i\,p_0\right\}; \qquad k = 1,2. \tag{2.43}$$

Equation (2.43) can be written in a matrix form as:

$$\begin{gathered}\prod_{i=1}^{n_n-1}\left[\left(\boldsymbol{k}^i - \omega^2\boldsymbol{m}^i\right)\boldsymbol{q}^i\right] = -\prod_{i=1}^{n_n-1}\boldsymbol{p}^i,\\ \boldsymbol{k}^i = \sum_{l=1}^{2}\int_{\Omega_e^i} n_{k,x}^i\,\frac{E}{\zeta}n_{l,x}^i\,dx,\ \boldsymbol{m}^i = \rho\sum_{l=1}^{2}\int_{\Omega_e^i} n_k^i\,\zeta\,n_l^i\,dx,\ \boldsymbol{p}^i = n_k^i\,p_0; \quad k = 1,2,\end{gathered} \tag{2.44}$$

where $\boldsymbol{k}^i$ and $\boldsymbol{m}^i$ are element stiffness and mass matrices. The right-hand side of Equation (2.44), $\boldsymbol{p}^i$, vanishes at inter-element boundaries (upon assembling element contributions) and must be evaluated on external boundaries where derivative boundary conditions are specified. Equation (2.44) can be made more compact by putting it in the form:

$$\begin{gathered}\left(\boldsymbol{K} - \omega^2\boldsymbol{M}\right)\boldsymbol{Q} = \boldsymbol{P},\\ \boldsymbol{K} = \prod_{i=1}^{n_n-1}\boldsymbol{k}^i,\ \boldsymbol{M} = \prod_{i=1}^{n_n-1}\boldsymbol{m}^i,\ \boldsymbol{Q} = \prod_{i=1}^{n_n-1}\boldsymbol{q}^i,\ \boldsymbol{P} = -\prod_{i=1}^{n_n-1}\boldsymbol{p}^i.\end{gathered} \tag{2.45}$$

$\boldsymbol{K}$,$\boldsymbol{M}$,$\boldsymbol{Q}$, and $\boldsymbol{P}$ are global stiffness, mass, displacement, and load vectors, respectively.

2.7 Time-domain FE-PML Formulation

Substituting Equation (2.25) into Equation (2.24) yields

$$E\left(u_{,\bar{x}}\right)_{,\bar{x}} = \rho\ddot{u}. \tag{2.46}$$

The steady-state form of Equation (2.46) can be written as:

$$E\left(u_{,\bar{x}}\right)_{,\bar{x}} = -\rho\omega^2 u. \tag{2.47}$$

Applying the chain-rule to Equation (2.47) results in the steady-state equilibrium equation terms of $\frac{\partial^i x}{\partial \bar{x}^i}$ $\left(i = 1,2\right)$ and the damping profile d as follows:

$$Eu_{,xx}\left(x_{,\bar{x}}\right)^2 + Eu_{,x}\left(x_{,\bar{x}\bar{x}}\right) = -\rho\omega^2 u. \tag{2.48}$$

Using Equations (2.19) and (2.20), $\frac{\partial^i x}{\partial \bar{x}^i}$ $\left(i = 1,2\right)$ can be written as

$$x_{,\bar{x}} = \frac{j\omega}{\left(j\omega + d\right)}, \tag{2.49}$$

$$x_{,\bar{x}\bar{x}} = \frac{\omega^2 d_{,x}}{\left(j\omega + d\right)^3}. \tag{2.50}$$

Substituting Equations (2.49) and (2.50) into (2.48) yields the following displacement-based governing equation:

$$\frac{Eu_{,xx}}{\rho\left(j\omega + d\right)^2} - \frac{Ed_{,x}u_{,x}}{\rho\left(j\omega + d\right)^3} = u. \tag{2.51}$$

Substituting for the two terms on the left-hand side of Equation (2.51) by

$$u_1 = \frac{Eu_{,xx}}{\rho\left(j\omega + d\right)^2}, \tag{2.52}$$

$$u_2 = -\frac{Ed_{,x}u_{,x}}{\rho\left(j\omega + d\right)^3}, \tag{2.53}$$

will result in

$$u = u_1 + u_2. \tag{2.54}$$

Equation (2.54) implies that the displacement wavefield, u, has been split into two components, u_1 and u_2. In order to invert Equations (2.52) and (2.53) into the time domain without convolution, the damping profile, d, is assumed real. Thus, by inspection, inverse Fourier transformation of Equations (2.52) and (2.53) can be written as

$$Eu_{,xx} = \left(\frac{\partial}{\partial t} + d\right)^2 u_1, \tag{2.55}$$

$$-Ed_{,x}u_{,x} = \left(\frac{\partial}{\partial t} + d\right)^3 u_2. \tag{2.56}$$

In order to facilitate the solution, Equation (2.56), containing a third-order differential operator, will be split into two equations: one containing a second-order differential operator and the other containing a first-order differential operator as follows:

$$-Ed_{,x}u_{,x} = \left(\frac{\partial}{\partial t} + d\right)^2 u_3, \tag{2.57}$$

$$u_3 = \left(\frac{\partial}{\partial t} + d\right) u_2. \tag{2.58}$$

Following the FE procedure outlined in the previous section, Equations (2.55), (2.57), and (2.58) can be written as

$$\ddot{\bar{\boldsymbol{Q}}}_1 = \boldsymbol{M}^{-1}\left[\boldsymbol{P} - \boldsymbol{K}_1\boldsymbol{Q}\right], \tag{2.59}$$

$$\ddot{\bar{\boldsymbol{Q}}}_3 = -\boldsymbol{M}^{-1}\boldsymbol{K}_2\boldsymbol{Q}, \tag{2.60}$$

$$\boldsymbol{Q}_3 = \dot{\bar{\boldsymbol{Q}}}_2. \tag{2.61}$$

A over-bar is combined with a single over-dot to denote the first-order differential operator $\left(\partial/\partial t + d\right)$ and a double over-dot to denote the second-order differential operator $\left(\partial/\partial t + d\right)^2$. Matrices $\boldsymbol{M}$, $\boldsymbol{K}_1$, and $\boldsymbol{K}_2$ are obtained from the following element-level counterparts by standard FE assembly procedure outlined in the previous section:

$$\begin{gathered}
\boldsymbol{K}_1 = \prod_{i=1}^{n_n-1} \boldsymbol{k}_1^i,\ \boldsymbol{K}_2 = \prod_{i=1}^{n_n-1} \boldsymbol{k}_2^i,\ \boldsymbol{M} = \prod_{i=1}^{n_n-1} \boldsymbol{m}^i,\ \boldsymbol{P} = \prod_{i=1}^{n_n-1} \boldsymbol{p}^i \\
\boldsymbol{k}_1^i = \sum_{l=1}^{2} \int_{\Omega_e^i} n_{k,x}^i En_{l,x}^i dx,\ \boldsymbol{k}_2^i = \sum_{l=1}^{2} \int_{\Omega_e^i} n_k^i d_{,x} En_{l,x}^i dx, \\
\boldsymbol{m}^i = \rho \sum_{l=1}^{2} \int_{\Omega_e^i} n_k^i n_l^i dx,\ \boldsymbol{p}^i = -n_k^i p_0;\ \ k = 1,2.
\end{gathered} \tag{2.62}$$

2.8 Explicit Time Integration

Rewrite the second-order differential equation (2.59) in its expanded form as follows:

$$\ddot{\boldsymbol{Q}}_1 + 2d\dot{\boldsymbol{Q}}_1 + d^2\boldsymbol{Q}_1 = \boldsymbol{M}^{-1}\left[\boldsymbol{P} - \boldsymbol{K}_1\boldsymbol{Q}\right]. \tag{2.63}$$

At time $t = t_{i+1}$, Equation (2.63) becomes:

$$\ddot{\boldsymbol{Q}}_{1(i+1)} + 2d\dot{\boldsymbol{Q}}_{1(i+1)} + d^2\boldsymbol{Q}_{1(i+1)} = \boldsymbol{M}^{-1}\left[\boldsymbol{P} - \boldsymbol{K}_1\boldsymbol{Q}_i\right]. \tag{2.64}$$

In a Newmark explicit time integration scheme, the velocity, $\dot{\boldsymbol{Q}}_{1(i+1)}$, and the displacement, $\boldsymbol{Q}_{1(i+1)}$, are taken as:

$$\dot{\boldsymbol{Q}}_{1(i+1)} = \dot{\boldsymbol{Q}}_{1(i)} + \left(\frac{\ddot{\boldsymbol{Q}}_{1(i)} + \ddot{\boldsymbol{Q}}_{1(i+1)}}{2}\right)\Delta t, \tag{2.65}$$

$$\boldsymbol{Q}_{1(i+1)} = \boldsymbol{Q}_{1(i)} + \left(\dot{\boldsymbol{Q}}_{1(i+1)} + \frac{\ddot{\boldsymbol{Q}}_{1(i+1)}\Delta t}{2}\right)\Delta t. \tag{2.66}$$

Substituting Equations (2.65) and (2.66) in Equation (2.64) results in

$$\begin{aligned}\ddot{\boldsymbol{Q}}_{1(i+1)} + 2d\dot{\boldsymbol{Q}}_{1(i)} + d\ddot{\boldsymbol{Q}}_{1(i)}\Delta t + d\ddot{\boldsymbol{Q}}_{1(i+1)}\Delta t + d^2\boldsymbol{Q}_{1(i)} + d^2\dot{\boldsymbol{Q}}_{1(i)}\Delta t + \ddot{\boldsymbol{Q}}_{1(i)}\frac{\left(d\Delta t\right)^2}{2} \\ +\ddot{\boldsymbol{Q}}_{1(i+1)}\left(d\Delta t\right)^2 = \boldsymbol{M}^{-1}\left[\boldsymbol{P} - \boldsymbol{K}_1\boldsymbol{Q}_i\right].\end{aligned} \tag{2.67}$$

Rearranging terms in Equation (2.67) results in the following equation that determines $\ddot{\boldsymbol{Q}}_{1(i+1)}$ in terms of $\boldsymbol{Q}_1$, $\dot{\boldsymbol{Q}}_1$, and $\ddot{\boldsymbol{Q}}_{1(i)}$

$$\ddot{\boldsymbol{Q}}_{1(i+1)} = \frac{\boldsymbol{M}^{-1}\left[\boldsymbol{P} - \boldsymbol{K}_1\boldsymbol{Q}_i\right] - d\left\{d\boldsymbol{Q}_{1(i)} + \left[1 + \frac{d\Delta t}{2}\right]\left[\ddot{\boldsymbol{Q}}_{1(i)}\Delta t + 2\dot{\boldsymbol{Q}}_{1(i)}\right]\right\}}{\left[1 + d\Delta t + \left(d\Delta t\right)^2\right]}. \tag{2.68}$$

Similarly, the first order system in Equation (2.61) can be written in general the form:

$$\dot{\boldsymbol{Q}}_2 + d\boldsymbol{Q}_2 = \boldsymbol{Q}_3. \tag{2.69}$$

Equation (2.69) can be made discrete at time $t = t_{i+1}$ as follows:

$$\frac{\boldsymbol{Q}_{2(i+1)} - \boldsymbol{Q}_{2(i)}}{\Delta t} + d\boldsymbol{Q}_{2(i+1)} = \boldsymbol{Q}_{3(i+1)}. \tag{2.70}$$

After rearranging terms, $\boldsymbol{Q}_{2(i+1)}$ can be written in terms of $\boldsymbol{Q}_{2(i)}$ and $\boldsymbol{Q}_{3(i+1)}$ as follows

$$\boldsymbol{Q}_{2(i+1)} = \frac{\left(\boldsymbol{Q}_{2(i)} + \boldsymbol{Q}_{3(i+1)}\Delta t\right)}{\left(1 + d\Delta t\right)}. \tag{2.71}$$

In this chapter we have demonstrated in details how to formulate and implement the PML within the framework of a standard FEM procedure in one dimension. In the next chapter we will consider the 2D problem of SH wave propagation and scattering in an infinite plate.

Chapter 3

SH Waves in Infinite Plates

This chapter presents FE formulations of the PML for guided SH wave motion in an infinite isotropic plate in both time- and frequency-domain. Numerical results based on these formulations are validated against: 1) exact analytical representation of the SH wave motion due to an out-of-plane uniform stress applied across the plate's thickness; 2) frequency-domain hybrid modeling of the SH wave motion due to various loading conditions; and 3) extended-mesh finite-element (EMFE) solutions of various problems in the time-domain.

3.1 Statement of the Problem

A schematic of the problem to be treated in this chapter is given in Figure 3.1. A point circumscribed by a full circle denotes an outward normal to the plane of the text. The layout depicts an infinite, stress- and body-force-free plate having a uniform dimen-

sionless thickness, h. Coordinates x and z as well as the out-of-plane y-displacement, v, are made dimensionless with respect to the plate's thickness, $\underline{h}$, as follows

$$h = \frac{\underline{h}}{\underline{h}} = 1,\ x = \frac{\underline{x}}{\underline{h}},\ z = \frac{\underline{z}}{\underline{h}},\ v = \frac{\underline{v}}{\underline{h}}. \tag{3.1}$$

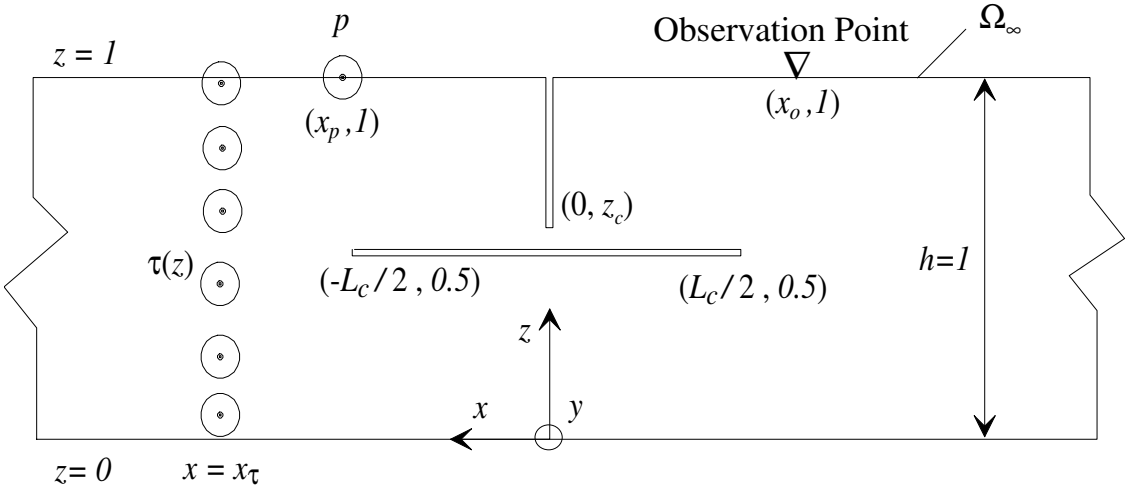

Figure 3.1 A schematic of the problem

In Equation (3.1) and the later Equations (3.2)-(3.4), dimensional variables on the right-hand side are underlined. Afterwards, only dimensionless quantities are used. The material of the plate is isotropic with shear modulus and density denoted by μ and ρ respectively. Stress, σ and surface traction, τ, are made dimensionless with respect to the dimensional shear modulus, $\underline{\mu}$, such that

$$\mu = \frac{\underline{\mu}}{\underline{\mu}} = 1,\ \sigma = \frac{\underline{\sigma}}{\underline{\mu}},\ \tau = \frac{\underline{\tau}}{\underline{\mu}}. \tag{3.2}$$

The plate could be subjected to an out-of-plane stress, τ, that is distributed uniformly across its thickness or an out-of-plane, dimensionless line load, p, acting on its top surface, see Figure 3.1. The dimensionless form of p can be written as

$$p = \underline{p} \Big/ \underline{\mu}\underline{h}. \tag{3.3}$$

Load time dependence takes either the Gaussian or one-cycle-sinusoidal forms shown in Figure 3.2. In Figure 3.2 and throughout this chapter, time, t, and angular frequency, ω, are made dimensionless with respect h, μ, and ρ as follows

$$\rho = \underline{\rho} \Big/ \underline{\rho} = 1,\ \underline{c}_s = \sqrt{\underline{\mu} \Big/ \underline{\rho}},\ c_s = \underline{c}_s \Big/ \underline{c}_s = 1,\ \omega = \underline{\omega h} \Big/ \underline{c}_s,\ \ t = \underline{t\, c}_s \Big/ \underline{h}, \tag{3.4}$$

where $\underline{c}_s$ and c_s are, respectively, dimensional and dimensionless shear wavespeed of plate's material. The plate may or may not contain a crack. If a crack exists, it can be a buried horizontal crack or a surface-breaking vertical crack.

3.2 Governing Equations

The equilibrium equation for harmonic SH wave motion in an infinite flawless plate can be written as follows:

$$\sigma_{yx,x} + \sigma_{yz,z} = \ddot{v}. \tag{3.5}$$

Applying forward Fourier transformation to Equation (3.5) produces the steady-state equilibrium equation

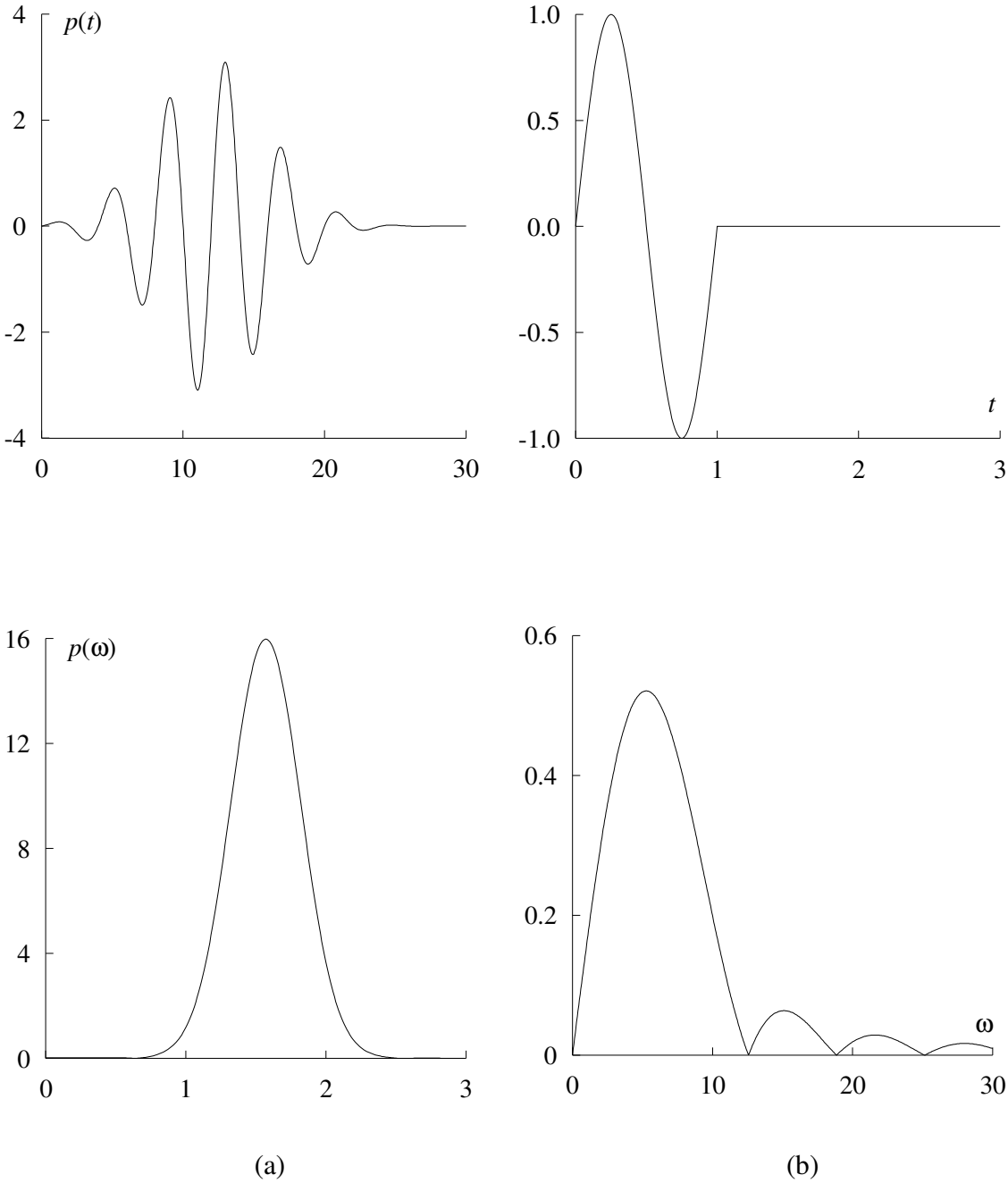

Figure 3.2 Time histories (top) and corresponding frequency spectra (bottom) of (a) a Gaussian and (b) a one-cycle sinusoidal signal

$$\sigma_{yx,x} + \sigma_{yz,z} + \omega^2 v = 0. \tag{3.6}$$

Relevant constitutive relations of the plate's isotropic material are:

$$\sigma_{yx} = v_{,x}, \quad \sigma_{yz} = v_{,z}. \tag{3.7}$$

Substituting the relations in Equation (3.7) into Equation (3.6) gives the governing displacement-based equilibrium equation as follows

$$v_{,xx} + v_{,zz} + \omega^2 v = 0. \tag{3.8}$$

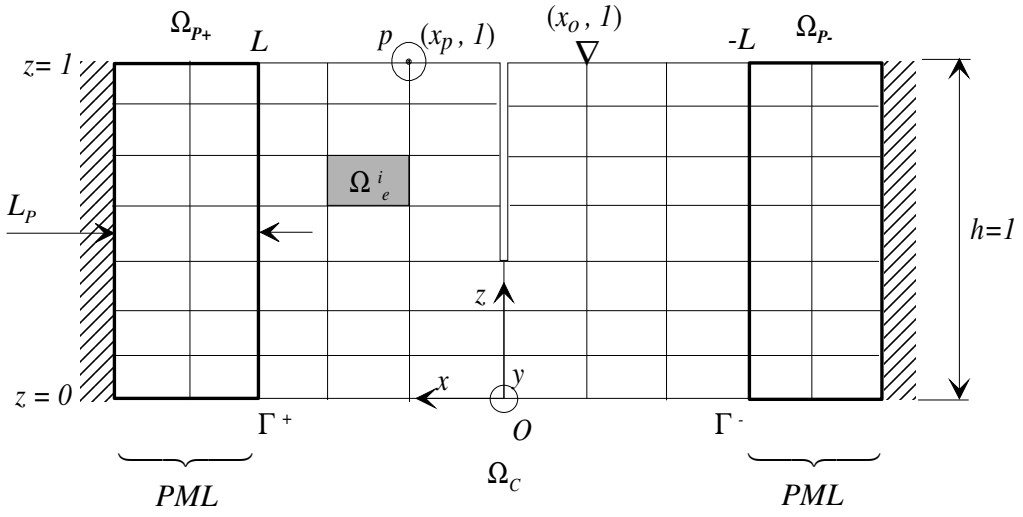

Figure 3.3 A schematic of the plate's FE-PML model

Figure 3.3 shows a layout of a combined FE-PML model of the infinite plate. The infinite physical domain of the problem, Ω_∞, is replaced by a computational domain, Ω_C, surrounded by two (thick-lined) PMLs, Ω_{P-} and Ω_{P+}, with two (left and right) interfaces, Γ^+ and Γ^-. Thus, the finite problem domain now is $\Omega = \Omega_{P-} \cup \Omega_C \cup \Omega_{P+}$

The response of the plate to applied loading is computed within the boundaries of the computational domain, Ω_C. Modeling the infinite plate shown in Figure 3.1 with a finite PML model involves a complex coordinate stretching of Equations (3.6) and (3.7) in the infinite x-direction by replacing the x-coordinate with a stretched coordinate, $\bar{x}$, as follows:

$$\sigma_{y\bar{x},\bar{x}} + \sigma_{yz,z} + \omega^2 v = 0, \tag{3.9}$$

$$\sigma_{y\bar{x}} = v_{,\bar{x}}, \quad \sigma_{yz} = v_{,y}. \tag{3.10}$$

Stretched x-coordinate, $\bar{x}$, is defined by Equations (2.19), (2.20), and the following damping profile:

$$d(x) = \begin{cases} -d(x) & -L > x \geq -(L + L_P), \\ 0 & -L \leq x \leq L, \\ d(x) & L < x \leq L + L_P. \end{cases} \tag{3.11}$$

It should be noted that a *complex* damping profile is used in conjunction with the FE-PML formulation in the frequency domain while a real damping profile is used in the time-domain, FE-PML Formulation. Using Equation (2.26), Equation (3.9) can be cast into the form

$$\sigma_{y\bar{x},x} + \zeta\sigma_{yz,z} + \omega^2 \zeta v = 0. \tag{3.12}$$

Boundary conditions applicable to Equation (3.9) in the case of an applied point load to the top surface of the plate as shown in Figure 3.3 are:

$$v(\pm(L + L_P), z) = 0, \quad \text{(Dirichlet boundary condition)} \tag{3.13}$$

$$\left.\begin{aligned}\sigma_{yz}(x,0)&=0,\\ \sigma_{yz}(x,1)&=p\delta(x_p),\end{aligned}\right\} \quad \text{(Neumann boundary conditions)} \tag{3.14}$$

where δ is the Dirac delta function.

3.3 Frequency-domain FE-PML Formulation

Let us seek an approximation, $\tilde{v}(x,z)$, to the unknown displacement solution, $v(x,z)$, in terms of discrete values, $Q_i = v(x_i, z_i)$ $(i = 1,...,n_n)$, and prescribed (interpolation) basis functions, N_l $(l = 0,1,...,n_n)$ as follows

$$\tilde{v} = N_0 + \sum_{l=1}^{n_n} N_l Q_l. \tag{3.15}$$

The function N_0 should satisfy prescribed Dirichlet boundary condition, i.e.

$$N_0 = v\left(\pm(L + L_P), z\right) = 0. \tag{3.16}$$

Thus, approximation $\tilde{v}$ becomes

$$\tilde{v} = \sum_{l=1}^{n_n} N_l Q_l. \tag{3.17}$$

Approximations, $\tilde{\sigma}_{y\bar{x}}$ and $\tilde{\sigma}_{zy}$, to the unknown stress solutions, $\sigma_{y\bar{x}}$ and σ_{yz}, should follow from Equation (3.10) as

$$\tilde{\sigma}_{y\bar{x}} = \tilde{v}_{,\bar{x}}, \quad \tilde{\sigma}_{yz} = \tilde{v}_{,z}. \tag{3.18}$$

Substituting approximations, $\tilde{\sigma}$ and $\tilde{v}$, into Equation (3.12) yields a residue:

$$R(x,y) = \tilde{\sigma}_{y\bar{x},x} + \zeta\tilde{\sigma}_{yz,z} + \omega^2\zeta\tilde{v}. \tag{3.19}$$

Using Galerkin MWR to force the residual, $R(x, y)$, to zero

$$\int_{\Omega} N_k \left(\tilde{\sigma}_{y\bar{x},x} + \zeta \tilde{\sigma}_{yz,z} + \omega^2 \zeta \tilde{v} \right) dxdz = 0; \qquad k = 1, 2, ..., n_n. \tag{3.20}$$

Expanding the differential stress terms using integration by parts yields

$$\begin{aligned} &\int_{\Omega} \left(N_{k,x} \tilde{\sigma}_{y\bar{x}} + \zeta N_{k,z} \tilde{\sigma}_{yz} - \omega^2 \zeta N_k \tilde{v} \right) dxdz \\ &\qquad = \int_{z=0}^{z=1} N_k \tilde{\sigma}_{y\bar{x}} dz \Big|_{x=-L-L_P}^{x=L+L_P} + \int_{x=-L-L_P}^{x=L+L_P} \zeta N_k \tilde{\sigma}_{yz} dx \Big|_{z=0}^{z=1}; \quad k = 1, 2, ..., n_n. \end{aligned} \tag{3.21}$$

Substituting Equations (3.14), (3.17) and (3.18) into Equation (3.21), followed by exchanging the integration and summation signs results in:

$$\sum_{l=1}^{n_n} \int_{\Omega} \left(N_{k,x} \frac{1}{\zeta} N_{l,x} + \zeta N_{k,z} N_{l,z} - \omega^2 \zeta N_k N_l \right) dxdz Q_l = N_k p; \quad k = 1, 2, ..., n_n. \tag{3.22}$$

The FE form of Equation (3.22) is obtained by following a standard FE procedure similar to the one outlined in Section 2.6 [132]. This procedure yields the element stiffness matrix, mass matrix, and load vector given, respectively, in terms of element-level shape functions, n, as follows

$$\begin{aligned} \boldsymbol{k}^i &= \sum_{l=1}^{n_n^e} \int_{\boldsymbol{\Omega}_e^i} [n_{k,x} \frac{1}{\zeta} n_{l,x} + n_{k,z} \zeta n_{l,z} - \omega^2 n_k n_l] dxdz, \\ \boldsymbol{m}^i &= \sum_{l=1}^{n_n^e} \int_{\boldsymbol{\Omega}_e^i} n_k \zeta n_l dxdz, \\ \boldsymbol{p}^i &= n_k p; \qquad k = 1, ..., n_n^e, \end{aligned} \tag{3.23}$$

After FE assembly, the governing equation can written in the form

$$\begin{gathered}\left[\boldsymbol{K}-\omega^2\boldsymbol{M}\right]\boldsymbol{Q}=\boldsymbol{P},\\ \boldsymbol{K}=\prod_{i=1}^{n_e}\boldsymbol{k}^i,\ \boldsymbol{M}=\prod_{i=1}^{n_e}\boldsymbol{m}^i,\ \boldsymbol{P}=\prod_{i=1}^{n_e}\boldsymbol{p}^i,\end{gathered} \tag{3.24}$$

where $\boldsymbol{K}$ is the global stiffness matrix, $\boldsymbol{M}$ is the global mass matrix, and $\boldsymbol{P}$ is the surface traction vector. The complex linear system in Equation (3.24) is solved for steady-state nodal displacements, $\boldsymbol{Q}$. The computer sub-program LEQT1C from the International Mathematical and Statistical Library (IMSL®) was used.

3.4 Time-domain FE-PML Formulation

A displacement-based, PML formulation of the previously stated problem can be obtained by replacing x with $\bar{x}$ in Equation (3.8) as follows

$$v_{,\bar{x}\bar{x}}+v_{,zz}+\omega^2 v=0. \tag{3.25}$$

Using the chain rule to expand the first differential term on the left side of Equation (3.25) results in

$$\left(x_{,\bar{x}}\right)^2 v_{,xx}+x_{,\bar{x}\bar{x}}v_{,x}+v_{,zz}+\omega^2 v=0. \tag{3.26}$$

Using Equations (2.49) and (2.50) along with wave equation splitting, Equation (3.26) can be written as

$$v=v_1+v_2+v_3, \tag{3.27}$$

$$\left[j\omega+d\right]^2 v_1=v_{,xx}, \tag{3.28}$$

$$\left[j\omega+d\right]^3 v_2=-d_{,x}v_{,x}, \tag{3.29}$$

$$-\omega^2 v_3 = v_{,zz}. \tag{3.30}$$

Inverse Fourier transformation of Equations (3.28) through (3.30) yields the following displacement-based governing equations in the time domain

$$\ddot{\bar{v}}_1 = v_{,xx}, \tag{3.31}$$

$$\ddot{\bar{v}}_4 = -d_{,x} v_{,x}, \tag{3.32}$$

$$v_4 = \dot{\bar{v}}_2, \tag{3.33}$$

$$\ddot{\mathrm{v}}_3 = v_{,zz}. \tag{3.34}$$

Note that Equation (3.29), which has a third-order time derivative, is split now into Equations (3.33) and (3.33) that involves only second- and first-order time derivatives, respectively. An FE representation of Equations (3.27) and (3.31) - (3.34) can be written as:

$$\boldsymbol{Q} = \boldsymbol{Q}_1 + \boldsymbol{Q}_2 + \boldsymbol{Q}_3, \tag{3.35}$$

$$\boldsymbol{M}\ddot{\bar{\boldsymbol{Q}}}_1 = -\boldsymbol{K}_1 \boldsymbol{Q}, \tag{3.36}$$

$$\boldsymbol{M}\ddot{\bar{\boldsymbol{Q}}}_4 = -\boldsymbol{K}_2 \boldsymbol{Q}, \tag{3.37}$$

$$\boldsymbol{Q}_4 = \dot{\bar{\boldsymbol{Q}}}_2, \tag{3.38}$$

$$\boldsymbol{M}\ddot{\boldsymbol{Q}}_3 = \boldsymbol{P} - \boldsymbol{K}_3 \boldsymbol{Q}. \tag{3.39}$$

Matrices $\boldsymbol{K}_i \left(i = 1, 2, 3\right)$ and $\boldsymbol{M}$ are obtained by standard FE assembly of the corresponding element-level matrices as follows:

$$\boldsymbol{K}_1 = \prod_{i=1}^{n_e} \boldsymbol{k}_1^i, \quad \boldsymbol{k}_1^i = \sum_{l}^{n_n^e} \int_{\Omega_e^i} n_{k,x} n_{l,x} dx dz, \tag{3.40}$$

$$\boldsymbol{K}_2 = \prod_{i=1}^{n_e} \boldsymbol{k}_2^i, \quad \boldsymbol{k}_2^i = \sum_{l}^{n_n^e} \int_{\Omega_e^i} n_k d_{,x} n_{l,x} dxdz, \tag{3.41}$$

$$\boldsymbol{K}_3 = \prod_{i=1}^{n_e} \boldsymbol{k}_3^i, \quad \boldsymbol{k}_3^i = \sum_{l}^{n_n^e} \int_{\Omega_e^i} n_{k,z} n_{l,z} dxdz, \tag{3.42}$$

$$\boldsymbol{M} = \prod_{i=1}^{n_e} \boldsymbol{m}^i, \quad \boldsymbol{m}^i = \sum_{l}^{n_n^e} \int_{\Omega_e^i} n_k n_l dxdz, \tag{3.43}$$

$$\boldsymbol{P} = \prod_{i=1}^{n_e} \boldsymbol{p}^i, \quad \boldsymbol{p}^i = n_k p; \quad k = 1,...,n_n^e. \tag{3.44}$$

A solution of Equations (3.35-39) can be computed at each discrete time steps as follows

$$\ddot{\boldsymbol{Q}}_{1(i+1)} = \frac{-\boldsymbol{M}^{-1}\boldsymbol{K}_1\boldsymbol{Q}_i - d\left\{ d\boldsymbol{Q}_{1(i)} + \left[1 + \frac{d\Delta t}{2}\right]\left[\ddot{\boldsymbol{Q}}_{1(i)}\Delta t + 2\dot{\boldsymbol{Q}}_{1(i)}\right]\right\}}{\left[1 + d\Delta t + (d\Delta t)^2\right]}, \tag{3.45}$$

$$\dot{\boldsymbol{Q}}_{1(i+1)} = \dot{\boldsymbol{Q}}_{1(i)} + \frac{\ddot{\boldsymbol{Q}}_{1(i)} + \ddot{\boldsymbol{Q}}_{1(i+1)}}{2}\Delta t, \tag{3.46}$$

$$\boldsymbol{Q}_{1(i+1)} = \boldsymbol{Q}_{1(i)} + \left(\dot{\boldsymbol{Q}}_{1(i+1)} + \frac{\ddot{\boldsymbol{Q}}_{1(i+1)}}{2}\Delta t\right)\Delta t, \tag{3.47}$$

$$\ddot{\boldsymbol{Q}}_{4(i+1)} = \frac{-\boldsymbol{M}^{-1}\boldsymbol{K}_2\boldsymbol{Q}_i - d\left\{ d\boldsymbol{Q}_{4(i)} + \left[1 + \frac{d\Delta t}{2}\right]\left[\ddot{\boldsymbol{Q}}_{4(i)}\Delta t + 2\dot{\boldsymbol{Q}}_{4(i)}\right]\right\}}{\left[1 + d\Delta t + (d\Delta t)^2\right]}, \tag{3.48}$$

$$\dot{\boldsymbol{Q}}_{4(i+1)} = \dot{\boldsymbol{Q}}_{4(i)} + \frac{\ddot{\boldsymbol{Q}}_{4(i)} + \ddot{\boldsymbol{Q}}_{4(i+1)}}{2}\Delta t, \tag{3.49}$$

$$\boldsymbol{Q}_{4(i+1)} = \boldsymbol{Q}_{4(i)} + \left(\dot{\boldsymbol{Q}}_{4(i+1)} + \frac{\ddot{\boldsymbol{Q}}_{4(i+1)}}{2}\Delta t\right)\Delta t, \tag{3.50}$$

$$\boldsymbol{Q}_{2(i+1)} = \frac{\left(\boldsymbol{Q}_{2(i)} + \boldsymbol{Q}_{4(i+1)}\Delta t\right)}{\left(1 + d\,\Delta t\right)}, \tag{3.51}$$

$$\ddot{\boldsymbol{Q}}_{3(i+1)} = \boldsymbol{M}^{-1}\left[\boldsymbol{P} - \boldsymbol{K}_3\boldsymbol{Q}_i\right], \tag{3.52}$$

$$\dot{\boldsymbol{Q}}_{3(i+1)} = \dot{\boldsymbol{Q}}_{3(i)} + \frac{\ddot{\boldsymbol{Q}}_{3(i)} + \ddot{\boldsymbol{Q}}_{3(i+1)}}{2}\Delta t, \tag{3.53}$$

$$\boldsymbol{Q}_{3(i+1)} = \boldsymbol{Q}_{3(i)} + \left(\dot{\boldsymbol{Q}}_{3(i+1)} + \frac{\ddot{\boldsymbol{Q}}_{3(i+1)}}{2}\Delta t\right)\Delta t. \tag{3.54}$$

The current time-domain PML formulation is simpler and more computationally efficient than the time-domain PML formulation given by Basu and Chopra [128] where viscous damping needs to be involved and a system of equations has to be solved at each time step. Formulation of exact ABCs by NME for frequency-domain FE modeling for SH wave propagation and scattering in an isotropic infinite plate is presented next.

3.5 Exact ABCs by NME

3.5.1 Free SH Waves in an Infinite Plate

Substitute the harmonic solution for the wave equation into Equation (3.9) followed by the imposition of the following boundary conditions:

$$v_{,z}\big|_{z=0,1} = 0. \tag{3.55}$$

This will result in the following dimensionless, displacement solution

$$v = \sum_{l=0}^{\infty} C_l \cos \beta_l z \; e^{-j(\xi_l x - \omega t)}. \tag{3.56}$$

Here C_l are arbitrary constants and the dimensionless wave numbers, ξ_l and β_l, of the l^{th} mode in the x and z directions, respectively, are related to the dimensionless frequency ω, by the following relationship

$$\beta_l^2 = \omega^2 - \xi_l^2 = l\pi. \tag{3.57}$$

The solution given in Equation (3.48) can be divided into symmetric and anti-symmetric motions about the plane $z = 0.5$. It can be shown [133] that the symmetric and anti-symmetric modes correspond to $l = 0, 2, 4, \ldots$ and $l = 1, 3, 5, \ldots$, respectively. The frequency spectrum of the first three pairs of symmetric and anti-symmetric SH wave modes in a plate are shown in Figure 3.4. The dimensionless displacement, v_i, at point (x_i, z_i) in the plate can be approximated by the summation, $\tilde{v}_i$, of a finite number, M, of normal modes, i.e.

$$\tilde{v}_i = \sum_{l=0}^{M} C_l \cos \beta_l z_i \; e^{-j(\xi_l x_i - \omega t)}. \tag{3.58}$$

Equation (3.47) can be written in matrix form (with a suppressed time factor, $e^{j\omega t}$) as

$$\tilde{v}_i = \boldsymbol{G}_i \boldsymbol{D}, \tag{3.59}$$

$$\boldsymbol{G}_i = \{Co_0 \quad Co_1 \quad Co_2 \quad \ldots \quad Co_l\}, \; Co_l = \cos \beta_l z_i, \tag{3.60}$$

$$\boldsymbol{D} = \{C_0 E_0 \quad C_1 E_1 \quad C_2 E_2 \quad \ldots \quad C_l E_l\}^T, \; E_l = e^{j\xi_l x_i}. \tag{3.61}$$

Using Equation (3.8), $\sigma_{yx(i)}$ can be approximated similarly as:

$$\tilde{\sigma}_{yx(i)} = \boldsymbol{H}_i \boldsymbol{D}, \tag{3.62}$$

$$\boldsymbol{H}_i = \left\{ Co_0^{'} \quad Co_1^{'} \quad Co_2^{'} \quad \ldots \quad Co_l^{'} \right\},\ Co_l^{'} = j\xi_l \cos\beta_l z_i. \tag{3.63}$$

The formulation of ABCs from the free SH wave eigendata is presented next.

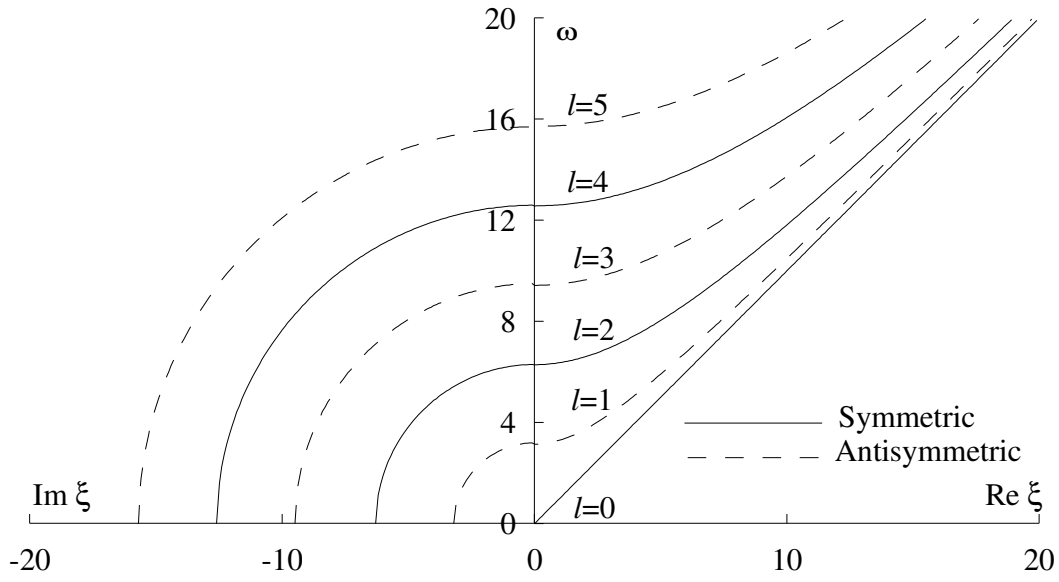

Figure 3.4 Frequency spectra of free SH waves in a plate

3.5.2 Hybrid FE-NME Formulation

In the hybrid method, the plate's infinite domain is divided into a finite region, Ω_C, surrounded by two infinite regions, $\Omega_{-\infty}$ and $\Omega_{+\infty}$, see Figure 3.5. Vertical, left and right, interface boundaries between the two regions are Γ^+ and Γ^-, respectively. If the plate is cracked, the crack should be contained inside Ω_C, while $\Omega_{-\infty}$ and $\Omega_{+\infty}$ should be crack-free. Loading can be applied either to Ω_C, $\Omega_{-\infty}$, or $\Omega_{+\infty}$ depending on material attenua-

tion and how far the observation and the load are separated. If the plate's material is highly attenuative (e.g. concrete or polyethylene), the loading and observation points must be located very closely, thus, allowing the load to be applied to the narrow Ω_C. This configuration is adopted in the current hybrid modeling to allow for a direct comparison with the FE-PML model for which loads can only be applied inside Ω_C. Application of the load to $\Omega_{-\infty}$ or $\Omega_{+\infty}$ is computationally economical for large load-observation separations. It has been considered by Zhu et al. [134] where Green's function was used to form the incident displacement and stress fields.

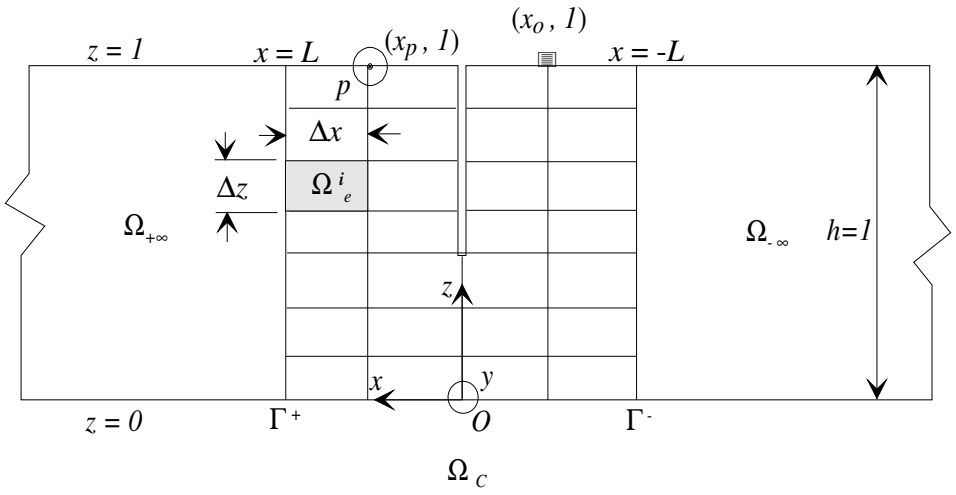

Figure 3.5 A schematic of the hybrid model. Finite elements are used to idealize the irregular computation domain, Ω_C.

Absorbing boundary conditions are enforced on the boundaries Γ^- and Γ^+ by evaluating the scattered displacements and stresses as follows

$$\boldsymbol{Q}^{\Gamma,S} = \boldsymbol{GD},\ \ \boldsymbol{S}_{yx}^{\Gamma,S} = \boldsymbol{HD}, \tag{3.64}$$

$$\boldsymbol{G} = \left\{\boldsymbol{G}_1 \quad \boldsymbol{G}_2 \quad \boldsymbol{G}_3 \quad ... \quad \boldsymbol{G}_{n_\Gamma}\right\}^T, \tag{3.65}$$

$$\boldsymbol{H} = \left\{\boldsymbol{H}_1 \quad \boldsymbol{H}_2 \quad \boldsymbol{H}_3 \quad ... \quad \boldsymbol{H}_{n_\Gamma}\right\}^T. \tag{3.66}$$

A superscript "*S*" denotes the scattered wave field. A subscript/superscript Γ refers to nodes located on the boundaries Γ^- and Γ^+. n_Γ is the number of nodes on the combined boundary, $\Gamma^- \cup \Gamma^+$, which is dictated by the FE discretization of the bounded region Ω_C. The FE form of Equation (3.6) can be obtained by following the standard FE procedure [133], in which the left side of Equation (3.6) is pre-multiplied by a trail function, N, and double integrated over Ω_C as follows:

$$\iint_{\Omega_C} \left[N_k \sigma_{yx,x} + N_k \sigma_{yz,z} + \omega^2 N_k v \right] dxdz = 0; \quad k = 1,2,...,n_n. \tag{3.67}$$

Performing the integration in Equation (3.67) by parts along with the interpolation of displacement using the same trial function, N, and the imposition of the boundary/continuity conditions on Ω_C leads to

$$\left[\boldsymbol{K}\right]\begin{Bmatrix}\boldsymbol{Q}^{\Omega} \\ \boldsymbol{Q}^{\Gamma}\end{Bmatrix} = \begin{Bmatrix}\boldsymbol{P}^{\Omega} \\ \tilde{\boldsymbol{P}}^{\Gamma,S}\end{Bmatrix}; \quad k,l = 1,2,...,n_n, \tag{3.68}$$

$$\begin{aligned}
\boldsymbol{K} &= \iint_{\Omega_C} [N_{k,x} N_{l,x} + N_{k,z} N_{l,z} - \omega^2 N_k N_l] dxdz, \\
\boldsymbol{P}^{\Omega} &= N_k p; \quad k = 1,2,...,n_\Omega, \\
\tilde{\boldsymbol{P}}^{\Gamma,S} &= \int_{\Gamma^- \cup \Gamma^+} N_k \tilde{\sigma}_{yx(k)} dz; \quad k = 1,2,...,n_\Gamma, \\
n_n &= n_\Omega + n_\Gamma.
\end{aligned} \tag{3.69}$$

$\boldsymbol{K}$ is the dynamic stiffness matrix. A subscript/superscript Ω refers to the degrees of freedom inside Ω_C. $\boldsymbol{Q}^{\Omega}/\boldsymbol{P}^{\Omega}$ and $\boldsymbol{Q}^{\Gamma}/\tilde{\boldsymbol{P}}^{\Gamma,S}$ are nodal displacements/load vectors inside Ω_C and on the combined interface boundaries $\Gamma^- \cup \Gamma^+$, respectively. n_Ω is the number of nodal points inside Ω_C. The integrals in Equation (3.69) are performed over each finite element, Ω_e^i, using local shape functions, n. Elemental contributions are, then, assembled together through a standard procedure. This will result in the dynamic stiffness, $\boldsymbol{K}$, and the internal load vector, $\boldsymbol{P}^{\Omega}$, to be defined as

$$\begin{aligned} \boldsymbol{K} &= \prod_{i=1}^{n_e} \boldsymbol{k}^i, \quad \boldsymbol{k}^i = \sum_{l=1}^{n_n^e} \iint_{\Omega_e^i} [n_{k,x} n_{l,x} + n_{k,z} n_{l,z} - \omega^2 n_k n_l] dx dz, \\ \boldsymbol{P}^{\Omega} &= \prod_{i=1}^{n_e} \boldsymbol{p}^{\Omega,i}, \quad \boldsymbol{p}^{\Omega,i} = n_k p; \quad k = 1,2,...,n_n^e. \end{aligned} \tag{3.70}$$

The boundary load vector, $\tilde{\boldsymbol{P}}^{\Gamma,S}$,

$$\begin{aligned} \tilde{\boldsymbol{P}}^{\Gamma,S} &= \boldsymbol{F}\boldsymbol{D}, \\ \boldsymbol{F} &= \left\{ \boldsymbol{F}_1 \quad \boldsymbol{F}_2 \quad \boldsymbol{F}_3 \quad ... \quad \boldsymbol{F}_{n_\Gamma} \right\}^T, \\ \boldsymbol{F}_k &= \int_{\Gamma^- \cup \Gamma^+} N_k \boldsymbol{H}_k dz \quad k = 1,2,...,n_\Gamma. \end{aligned} \tag{3.71}$$

Sub-structuring the dynamic stiffness, $\boldsymbol{K}$, in Equation (3.69) into four sub-matrices followed by the substitution of $\boldsymbol{Q}^{\Gamma,S}$ and $\tilde{\boldsymbol{P}}^{\Gamma,S}$ from Equations (3.64) and (3.71), respectively, yield the following

$$\begin{bmatrix} \boldsymbol{K}^{\Omega\Omega} & \boldsymbol{K}^{\Omega\Gamma} \\ \boldsymbol{K}^{\Gamma\Omega} & \boldsymbol{K}^{\Gamma\Gamma} \end{bmatrix} \begin{Bmatrix} \boldsymbol{Q}^{\Omega} \\ \boldsymbol{G}\boldsymbol{D} \end{Bmatrix} = \begin{Bmatrix} \boldsymbol{P}^{\Omega} \\ \boldsymbol{F}\boldsymbol{D} \end{Bmatrix}. \tag{3.72}$$

Through algebraic manipulation, Equation (3.72) can be written in terms of the unknown $\boldsymbol{Q}^{\Omega}$ and $\boldsymbol{D}$ as follows

$$\begin{bmatrix} \boldsymbol{K}^{\Omega\Omega} & \boldsymbol{K}^{\Omega\Gamma}\boldsymbol{G} \\ \boldsymbol{G}^T\boldsymbol{K}^{\Gamma\Omega} & \boldsymbol{G}^T\left(\boldsymbol{K}^{\Gamma\Gamma}\boldsymbol{G}-\boldsymbol{F}\right) \end{bmatrix} \begin{Bmatrix} \boldsymbol{Q}^{\Omega} \\ \boldsymbol{D} \end{Bmatrix} = \begin{Bmatrix} \boldsymbol{P}^{\Omega} \\ \boldsymbol{0} \end{Bmatrix}. \tag{3.73}$$

Equation (3.73) is a complex linear system of equations that is solved for $\boldsymbol{Q}^{\Omega}$ and $\boldsymbol{D}$ by lower-upper (LU) decomposition. Steady-state displacement responses are converted into time histories by using a discrete inverse Fourier transform. Numerical examples predicting the response of an infinite plate to anti-plane loading are presented next for the PML and the hybrid models.

3.6 Numerical Implementation

3.6.1 Sizing the Extended FE Mesh

In order to explain how the EMFE model is sized, let us consider the load-observation configuration shown in Figure 3.6. This load-observation configuration is symmetric about the centerline of the EMFE model with a $2L_T$ separation distance between the load and the observation. The objective is determine the minimum length, L_{EMFE}, such that reflections of the fastest wave mode traveling at maximum group velocity, $c_{g,\max}$, from

both boundaries does not show up within the time-window width of the applied load, T_e. The following inequality satisfies that condition

$$L_{EMFE} > \frac{T_e c_{g,\max}}{2} + \frac{L_T}{c_{g,\max}}. \tag{3.74}$$

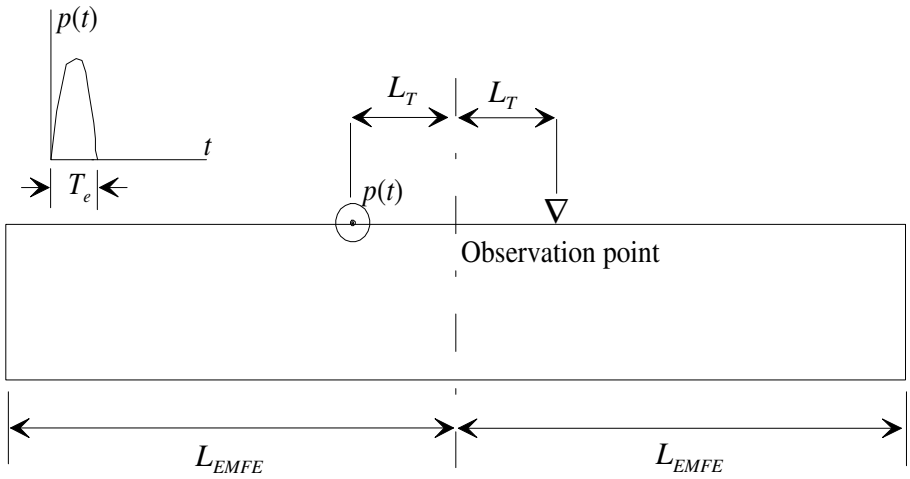

Figure 3.6 Illustration of EMFE model sizing

3.6.2 RMS Error

A measure of error in the FE-PML predictions relative to a reference prediction is considered in a root-mean-square (RMS) sense as follows:

$$\varepsilon_{RMS} = \left\{ \frac{\sum_{i=1}^{n_s} \left(s_{FE-PML}^{i} - s_R^{i} \right)^2}{\sum_{i=1}^{n} \left(s_R^{i} \right)^2} \right\}^{\frac{1}{2}}. \tag{3.75}$$

s_R^i and s_{FE-PML}^i are, respectively, the reference and FE-PML predictions at a sampling point (time or frequency), *i*, and n_s is the total number of sampling points. In this chapter, the reference predictions are the exact and the EMFE results.

3.6.3 Selection of the PML Parameters

The damping profile assumes the following empirical form:

$$d(x) = d_0 \left(\frac{x - L}{L_P} \right)^m . \tag{3.76}$$

The width of the damping layer, L_P, and the exponent, m, are selected based on a rudimentary trial-and-error procedure at all times. There are some available empirical formulae in the literature to determine the amplitude of the damping profile, d_0. Alternately, it can be determined by trial and error, which is adopted in this chapter.

3.6.4 Numerical Examples

The infinite plate considered in the following examples can be flawless, or it can contain a surface-breaking vertical crack $(z_c = 0.5)$, or a horizontal crack $(L_c = 1.0)$. Loading, $p = 1.0$ and $\tau(z) = 1.0$, are applied at $(-0.5, 1.0)$ and $(-0.5, z)$, respectively. In Examples 2 and 3, the boundaries of the EMFE model are set at $x = -15$ and $x = 15$ in order to shift the initial arrival of the shear wave reflection outside the duration of the applied

load. The response is predicted at $(0.5,1.0)$ in all examples. Linear, four-node elements are used in all FE meshes unless stated otherwise. For all types of elements, element dimensions are fixed at $\Delta x = 0.1$ and $\Delta z = 0.1$ in the x and z directions, respectively. In modeling a flawless plate or a plate containing a vertical crack, the boundaries Γ^- and Γ^+ are taken at $L = \pm 1.0$. In the case of a horizontal crack, Γ^- and Γ^+ are moved to $L = \pm 1.5$ to accommodate the lateral extent of the crack. The thickness of the absorbing layer is always $L_p = 0.5$ unless stated otherwise. It should be noted that a total number of 20 modes are used in the hybrid method throughout all examples.

Three numerical examples are considered. The first example compares the steady-state predictions made by the hybrid method and the PML method with exact analytical solutions for a flawless plate. It also contrasts the hybrid and PML predictions in terms of accuracy and computational efficiency. The second example compares FE-PML modeling results to those obtained by an EMFE. The third example considers the response of the plate to a high-frequency, wide-band, one-cycle sinusoidal signal for which a time-domain FE-PML model and an EMFE model are employed.

Example 1: ABCs versus Exact Analytical Solution

Predictions made by the hybrid method and the PML method (given that $d_0 = 10$ and $m = 1$ are assumed in Equation (3.76)) for the flawless plate's steady-state displacement response to a uniform anti-plane stress, $\tau = 1.0$, are shown in Figure 3.7. Excellent agreement is clearly evident with the exact analytical solution [133]. RMS errors in the

frequency-domain FE-PML predictions relative to exact analytical solution are 2.18% in the real part and 3.25% in the imaginary part. This numerical example was executed on an HP® Pavilion a805n, personal computer. It took 24 and 59 CPU seconds (or a ratio of 1:2.4) to produce the hybrid and the PML predictions, respectively.

In Figure 3.8a, a point load, $p = 1.0$ is applied instead. An exact analytical solution also exists for this case [133]. The hybrid method produces now somewhat less accurate results than the PML approach even when quadratic, eight-node elements are used. See Figure 3.8b. RMS errors in the hybrid predictions relative to exact analytical solution are 14.1% in the real and imaginary parts. These errors for the frequency-domain, FE-PML predictions are 3.03% and 3.13%, respectively.

Degradation of the hybrid method's accuracy as L increases has been reported previously by Zhu [135] for plane-strain, PSV, hybrid modeling in plates. On the contrary, increasing the lateral dimension of the bounded region enhances the performance of the FE-PML method [128]. In order to illustrate this observation, consider the steady-state responses to a point anti-plane load $(p = 1.0)$ of two, otherwise identical plates containing either a vertical crack or a horizontal crack. Predictions made by the PML and hybrid method are shown in Figure 3.9. The hybrid predictions in Figure 3.9a made by using $L = 1$ deviates from the FE-PML predictions by RMS errors of 13.24 % and 13.29 % in the real and imaginary parts respectively. The hybrid predictions in Figure 3.9a made by using $L = 1.5$ deviates from the FE-PML predictions by only RMS errors of 5.4 % and 5.5 % in the real and imaginary parts respectively.

This example also was executed on an HP® Pavilion a805n, personal computer. It took 25 and 96 seconds to produce the hybrid method predictions in Figures 3.9a and 3.9b, respectively. The corresponding times for the PML method are 60 and 174 seconds, or about 2.4 and 1.8 times longer. Thus, the percentage difference in CPU time between the hybrid method and the FE-PML method is lowered from 140% for a vertical crack to 82% for a horizontal crack. The FE-PML predictions shown in Figure 3.9 for $L_P = 0.5$ are superimposed in Figure 3.10 onto the corresponding curves for $L_P = 0.3$. It can be see that reducing the PML thickness affects somewhat the response of the vertically cracked plate. For a horizontally cracked plate, on the other hand, the response is hardly affected. However, the CPU time is reduced from 174 seconds to 125 seconds bringing the percentage difference between the hybrid and the FE-PML methods to 30% only.

Example 2: Time-domain PML versus windowed FE Modeling

Several results introduced in Example 1 are reproduced in this example by using direct, time-domain FE-PML analysis. Both the time-domain FE-PML formulation presented in Section 3.4 (for which $d_0 = 20$, $m = 3$, $L = 1.0$, $L_P = 5.0$ are used in Equation (3.76)) and an EMFE model. Figure 3.11 shows response time histories of a flawless plate to a uniform stress and a point load. The RMS error in the time-domain FE-PML predictions with reference to the EMFE results are 10.7% and 10.8 for Figures 3.11a and 3.11b, respectively. This numerical example was executed on a DELL PRECISION M6300 laptop. The time-domain FE-PML consumes 36 seconds while the extended FE model takes

86 seconds or about 2.9 times longer. Corresponding predictions for the two cases of a vertically- and a horizontally-cracked plate are shown in Figure 3.12. The RMS error in the time-domain FE-PML predictions with reference to the EMFE results are 11.3% and 12.5 for Figures 3.12a and 3.12b, respectively.

Wide-band signals (see Figure 3.2b) add an additional computational burden to frequency-domain methods due to the large number of discrete frequencies to be handled. This is not a problem for direct time-domain methods. Moreover, by using direct time-domain analysis, instantaneous snapshots of the time-evolving displacement field can be obtained more conveniently. This is demonstrated by the following example.

Example 3: Time-domain PML at higher frequencies

Snapshots of an infinite flawless plate's instantaneous responses to a point load, whose time dependence is a one-cycle sinusoid, see Figure 3.2, are shown in Figure 3.13. The snapshots are produced by using an EMFE model, Figure 3.13a, and a time-domain FE-PML model, Figure 3.13b.

Previously used parameters for the EMFE and FE-PML models remain in effect. The same color map is used to produce all the images presented in this example. Corresponding snapshots for the vertically- and horizontally-cracked plates are shown in Figures 3.14 and 3.15, respectively. Notice that triangles point to the surface opening of the vertical crack in Figure 3.14 and to the tips of the horizontal crack in Figure 3.15. A visual inspection suggests that the differences between the corresponding images produced by the two approaches be hardly noticeable. The presence of the vertical crack is distinguished

by a higher displacement field (a brighter spot) in its vicinity. The diffraction of the shear waves around the tips of the horizontal crack can be noticed by carefully comparing Figures 3.13 and 3.15. These observations support the assertion made in the Introduction that a crack's effect on shear waves is localized.

3.7 Conclusions

A combined FE and perfectly matched, absorbing, boundary layer approach to model SH wave propagation and scattering in infinite, isotropic plates is contrasted against exact analytical solution and exact ABCs formulated in terms of eigendata through the hybrid method. The hybrid method employs exact ABCs, however, its accuracy is a function of several parameters. Of those parameters is the width of the bounded region. It is shown that the RMS deviation in the hybrid predictions, compared to exact analytical/FE-PML solutions, dropped from 14% to 5% by increasing the width of the bounded region by 50%.

The combined FE-PML approach is implemented in both time and frequency domains. Maximum RMS error is about 3.0% in the FE-PML predictions compared to exact analytical solutions. In the time domain, a maximum RMS error of about 12% in the FE-PML predictions compared to the results of an EMFE model is observed. The frequency-domain, FE-PML model consumes more than twice as much computational time needed by the hybrid method, however, yields more accurate predictions. On the other side, the time-domain, FE-PML model require less execution time than the EMFE model.

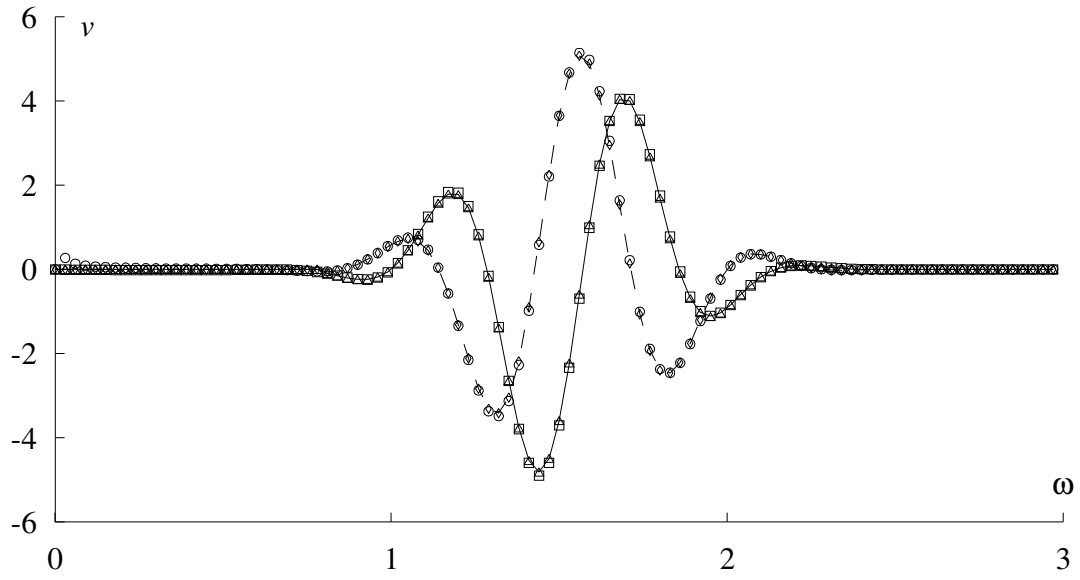

Figure 3.7 Steady-state response of a flawless infinite plate to an anti-plane load distributed uniformly across its thickness (____ Re. analytical; -------- Im. analytical; Δ Re. hybrid; ◊ Im. hybrid; □ R. FE-PML; O Im. FE-PML)

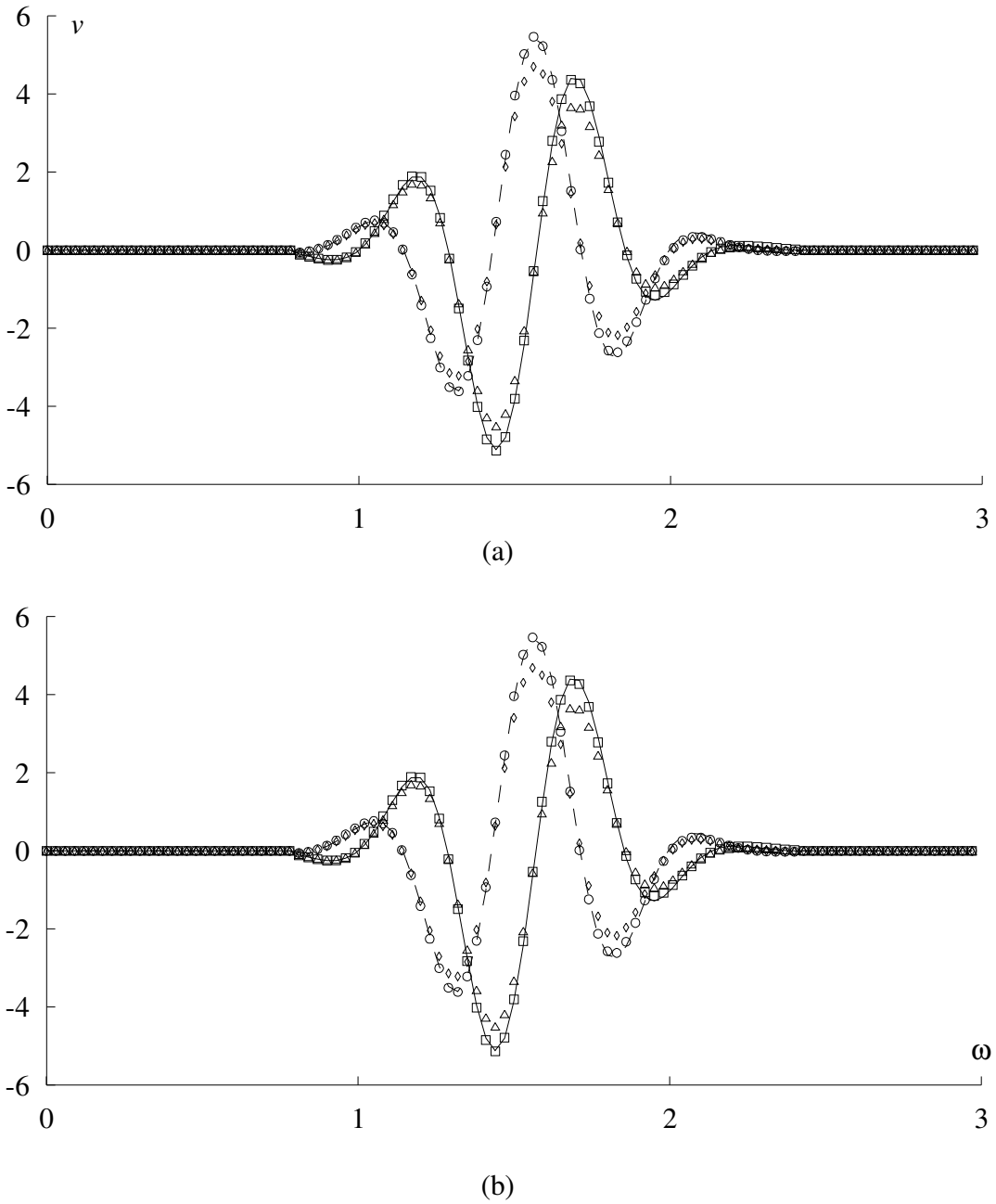

Figure 3.8 Steady-state response of a flawless infinite plate to an anti-plane point load using (a) four-node elements; and (b) eight-node elements with hybrid predictions (____ Re. analytical; -------- Im. analytical; Δ Re. hybrid; ◊ Im. hybrid; □ R. FE-PML; O Im. FE-PML)

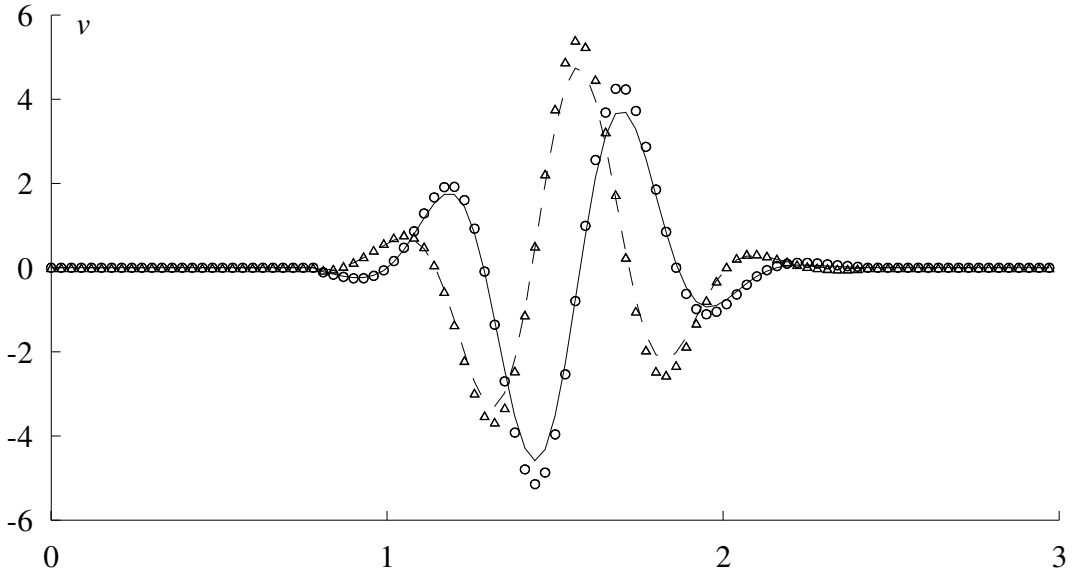

(a)

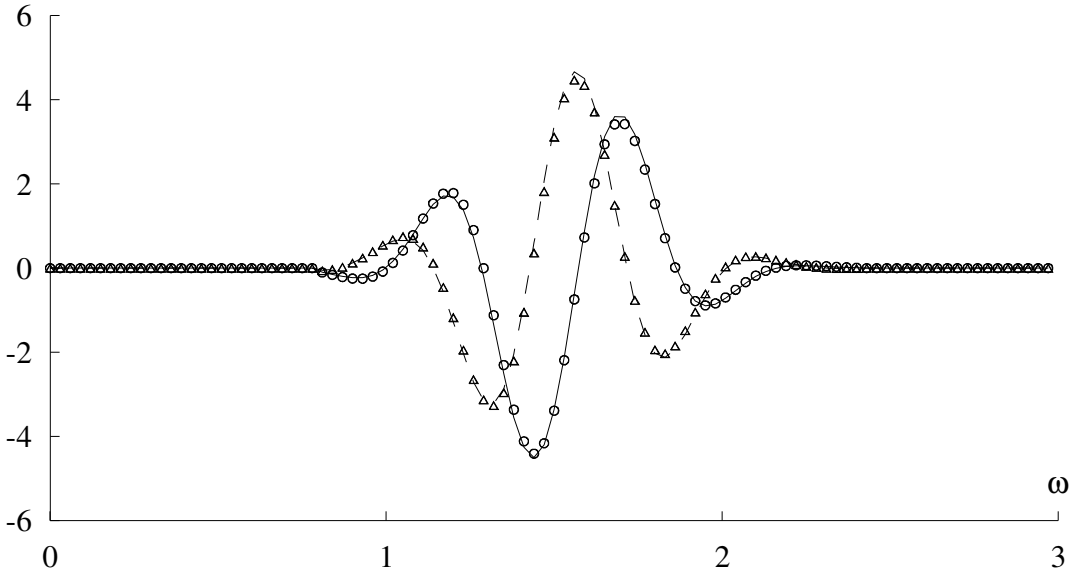

(b)

Figure 3.9 Steady-state responses of an infinite plate containing (a) surface-breaking vertical crack and (b) buried horizontal crack to an anti-plane point load (O Re. FE-PML; Δ Im. FE-PML; _____ Re. hybrid; ------- Im. hybrid)

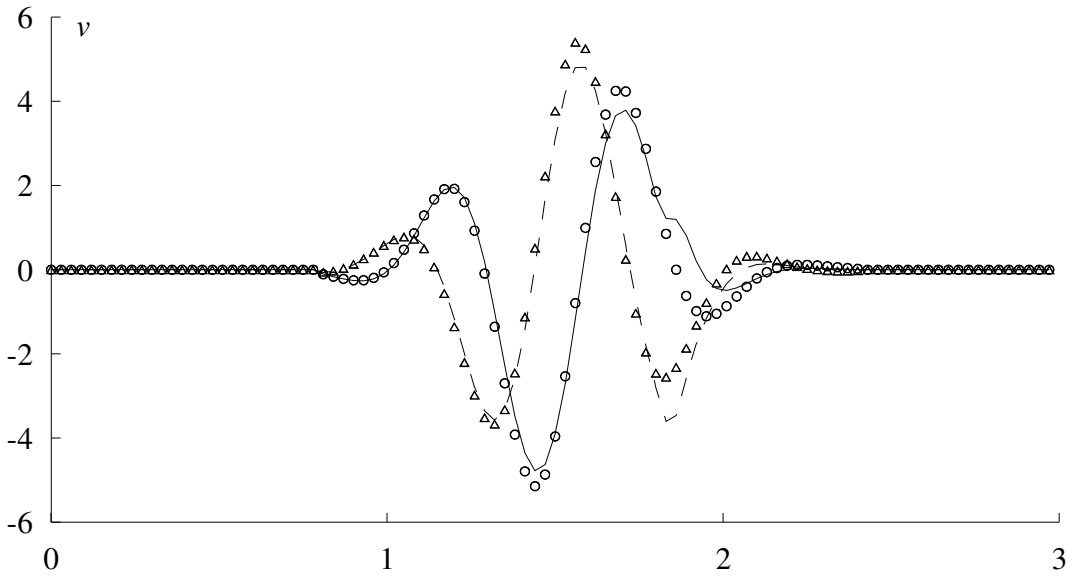

(a)

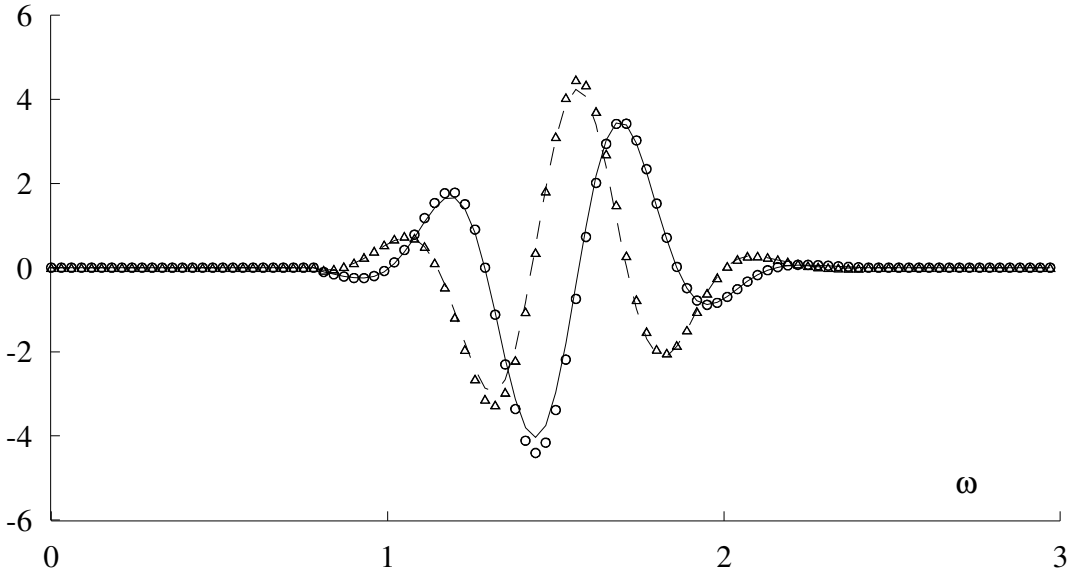

(b)

Figure 3.10 Reproduction of PML predictions given in Figure 3.9 for a reduced damping layer widths of 0.3 compared to a 0.5 in Figure 3.9 (O Re. FE-PML; Δ Im. FE-PML; _____ Re. hybrid; ------- Im. hybrid)

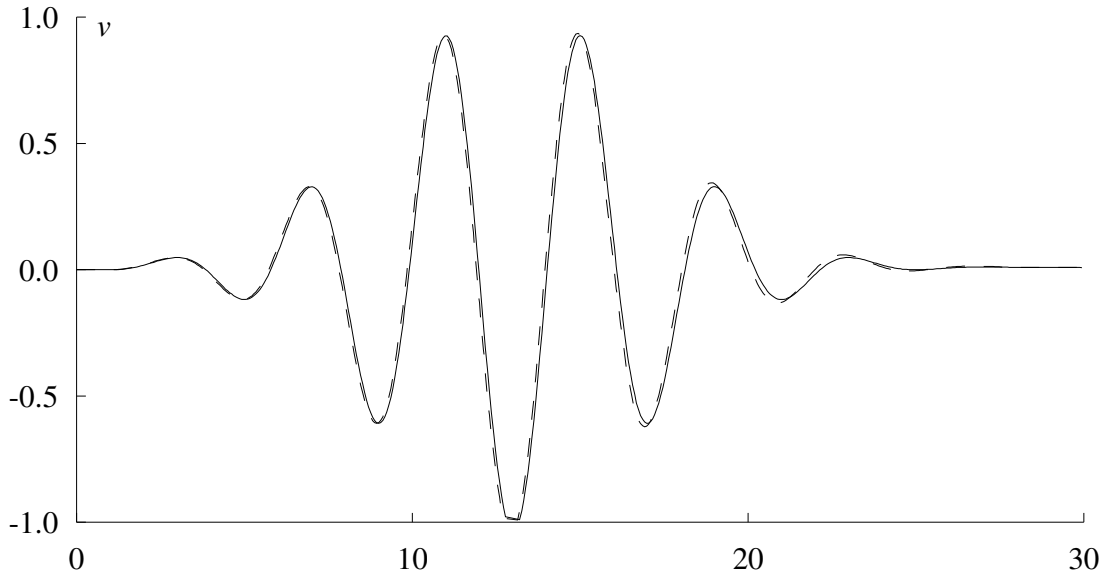

(a)

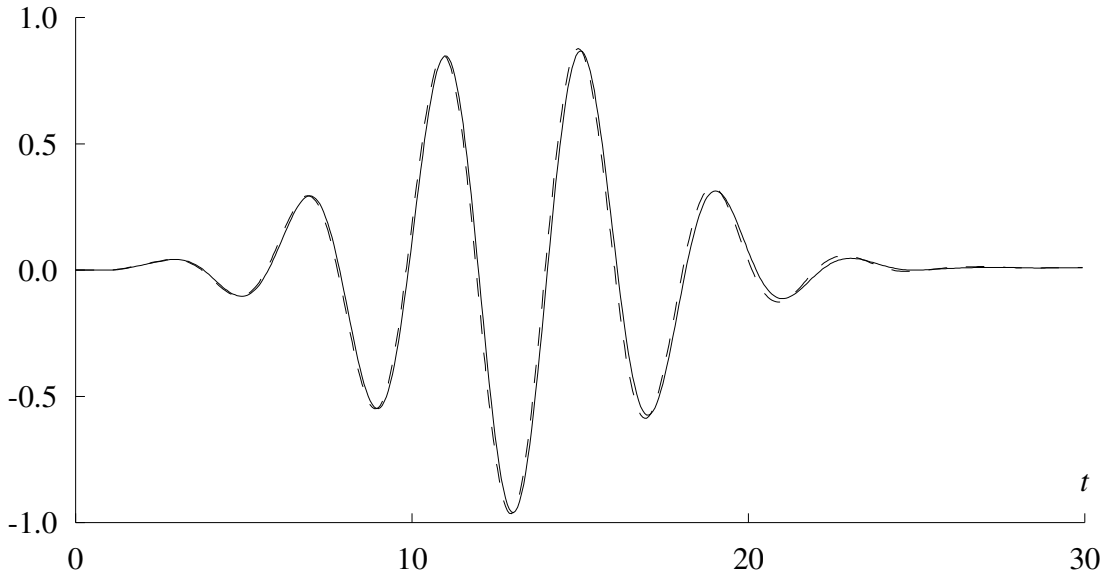

(b)

Figure 3.11 Time-history responses of a flawless infinite plate subject to an anti-plane (a) stress and (b) point load (_____ windowed FEM; ---------- FE-PML)

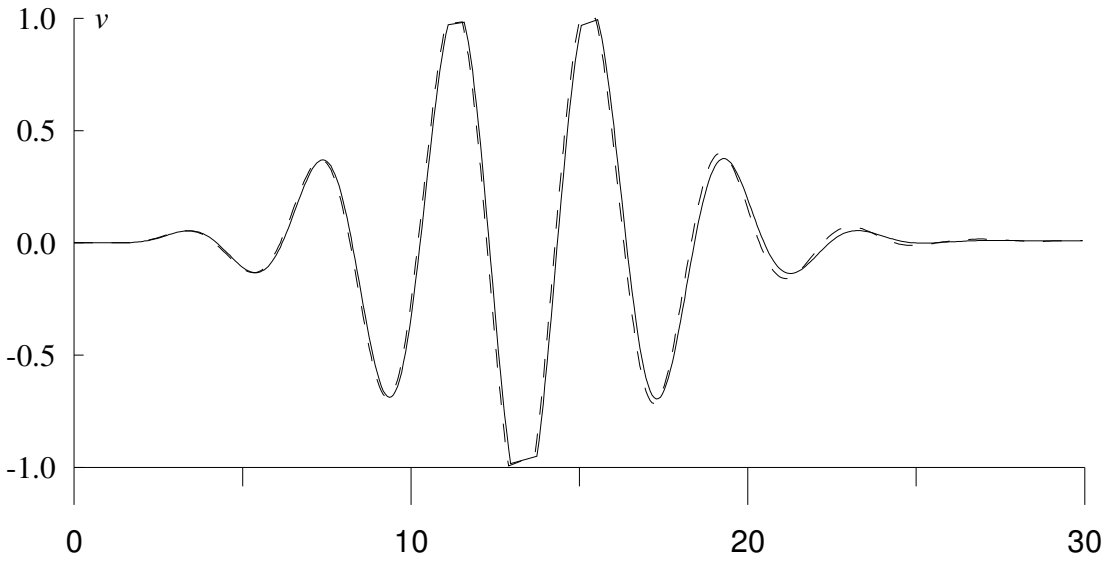

(a)

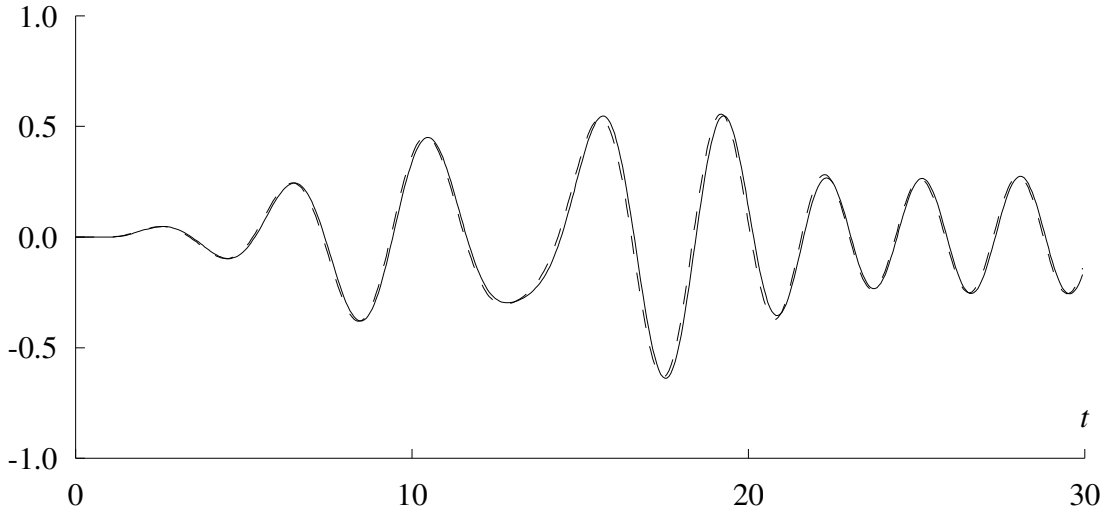

(b)

Figure 3.12 Transient response to an anti-plane point load for an infinite plate containing (a) a vertical crack and (b) a horizontal crack (_____ windowed FEM; ---------- FE-PML)

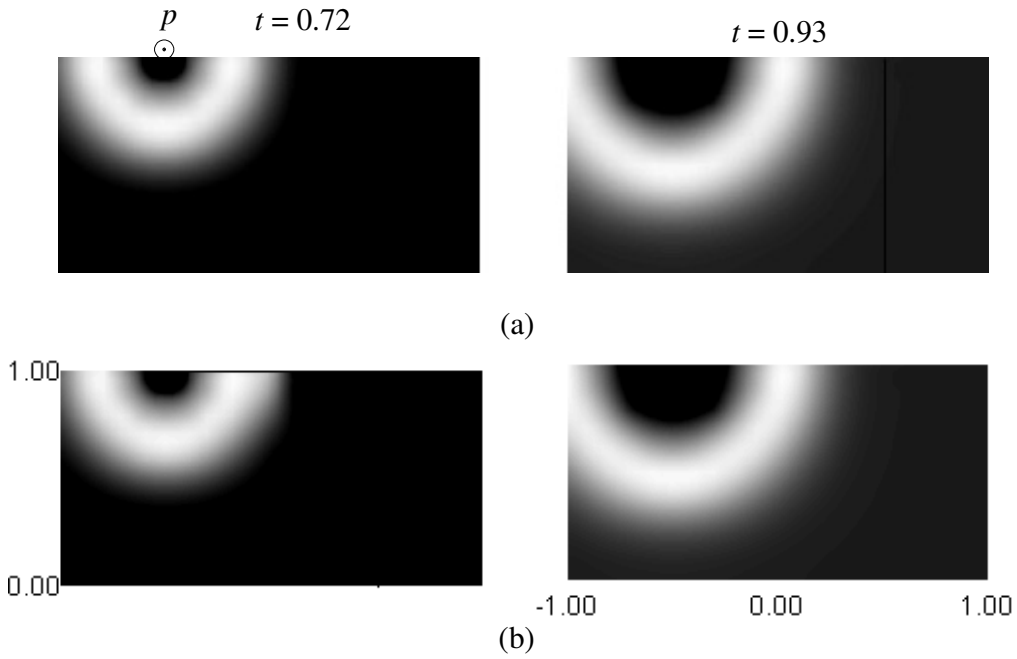

Figure 3.13 Snapshots of the displacement field in a flawless plate due to an anti-plane point load, *p*, predicted by using (a) an extended FE mesh and (b) a time-domain FE-PML.

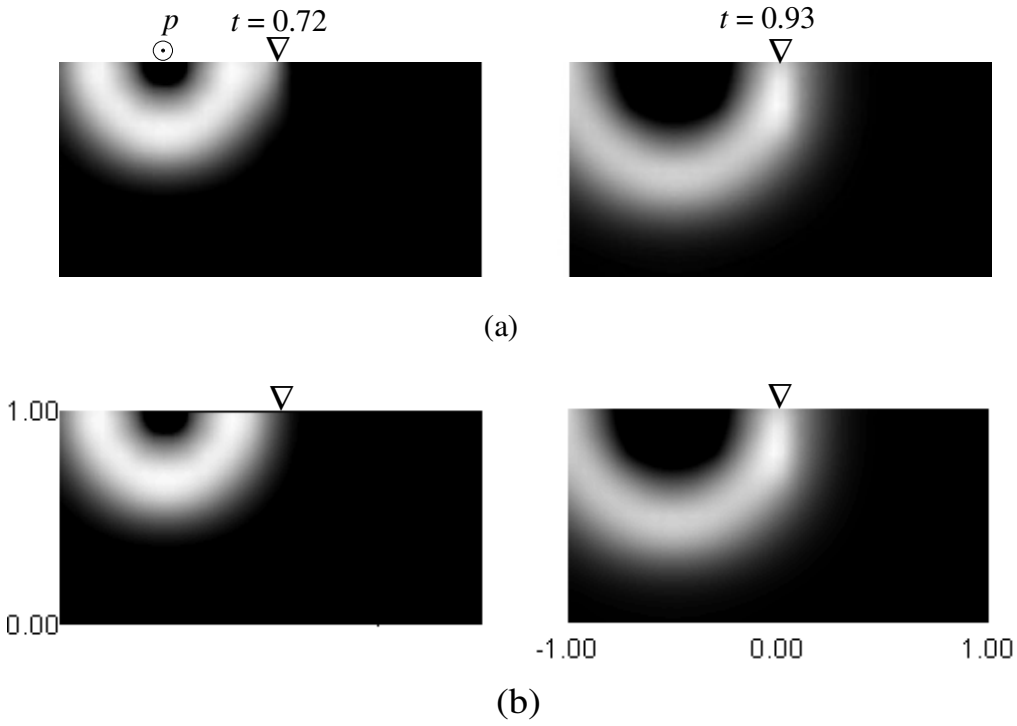

Figure 3.14 Snapshots of the displacement field in a vertically-cracked plate due to an anti-plane point load, p, predicted by using (a) an extended FE mesh and (b) a time-domain FE-PML.

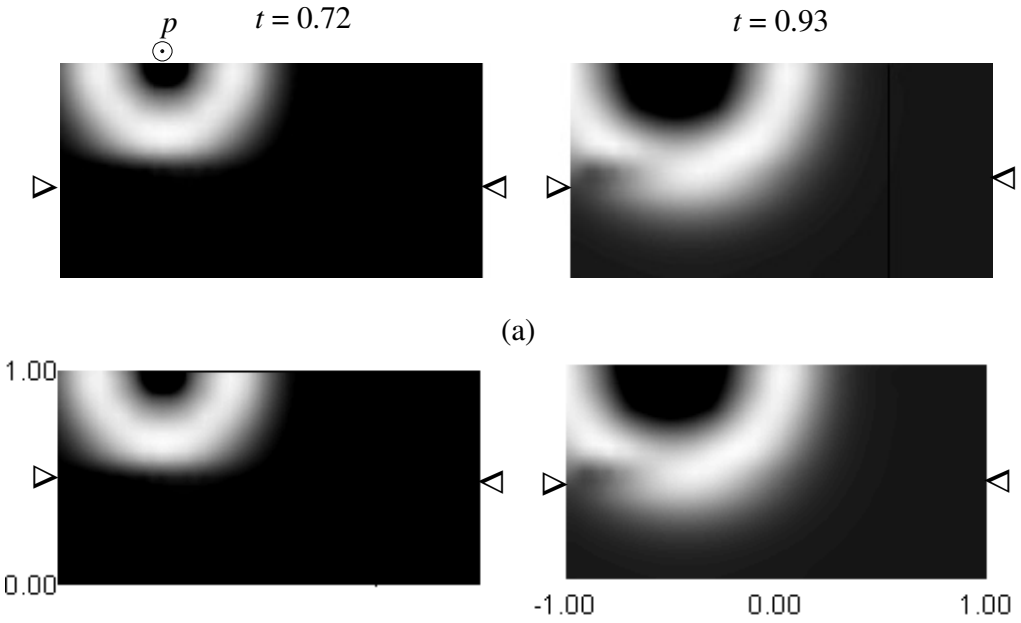

Figure 3.15 Snapshots of the displacement field in a horizontally-cracked plate due to an anti-plane point load, *p*, predicted by using (a) an extended FE mesh and (b) a time-domain FE-PML.

Chapter 4

PSV Waves in Infinite Plates

This chapter investigates the applicability of a time-domain implementation of the displacement-based, combined FE-PML formulation to numerical modeling of elastic, PSV wave propagation and scattering in infinite plates for the purpose of crack characterization. Results obtained using the proposed model satisfy reciprocity and verify available analytical and semi-analytical solutions. The results of forward scattering by cracks confirm previous experimental findings by Hudgell et al. [140] and can potentially help optimize experimental parameters.

4.1 Description of the Problem

The subject of this chapter is an infinitely-long plate having a uniform thickness, h, with and without a crack. The plate is described using a rectangular coordinate system. The origin is located on the bottom surface of the plate as shown in Figure 4.1. The infinite physical domain of the problem, Ω_∞, is a planar x-z cross section. The plate is excited

by a line load, p. A crack perpendicular to the x-z plane can be described by the (x_c, z_c) coordinates of its tip, its length, L_c, and the counter-clockwise angle, α, it makes with the positive x-axis. Displacements and lengths are made dimensionless by dividing them through plate's thickness, $\underline{h}$. Elastic constants, stresses and surface tractions are divided by $\underline{c}_{55}$ to get their dimensionless counterparts. Dimensionless line load, time, and frequency remain the same as defined by Equations (3.3) and (3.4) after replacing $\underline{\mu}$ with $\underline{c}_{55}$. In this chapter we seek the replacement of the infinite domain, Ω_∞, with a truncated domain, Ω_C and two PMLs, Ω_{P-} and Ω_{P+}, at $x = \pm L$, see Figure 4.2. As a result of the above replacement, we obtain a combined problem domain, $\Omega = \Omega_C \cup \Omega_{P-} \cup \Omega_{P+}$.

4.2 FE-PML Equations

Steady-state, PSV wave motion of the infinite plate in Figure 4.1, is governed by the following displacement-based equilibrium equation [136]:

$$\begin{aligned}
&\boldsymbol{c}_{xx}\boldsymbol{v}_{,xx} + \boldsymbol{c}_{xz}\boldsymbol{v}_{,xz} + \boldsymbol{c}_{xz}^T\boldsymbol{v}_{,zx} + \boldsymbol{c}_{zz}\boldsymbol{v}_{,zz} + \omega^2\boldsymbol{v} = \boldsymbol{0}, \\
&\boldsymbol{v} = \{u \quad w\}^T, \ \boldsymbol{c}_{ik} = \boldsymbol{I}_i^T\boldsymbol{c}\boldsymbol{I}_k; \ i,k = x,z, \\
&\boldsymbol{c} = \begin{bmatrix} c_{11} & c_{12} & 0 \\ c_{12} & c_{22} & 0 \\ 0 & 0 & c_{55} \end{bmatrix}, \ \boldsymbol{I}_x = \begin{bmatrix} 1 & 0 \\ 0 & 0 \\ 0 & 1 \end{bmatrix}, \ \boldsymbol{I}_z = \begin{bmatrix} 0 & 0 \\ 0 & 1 \\ 1 & 0 \end{bmatrix}.
\end{aligned} \tag{4.1}$$

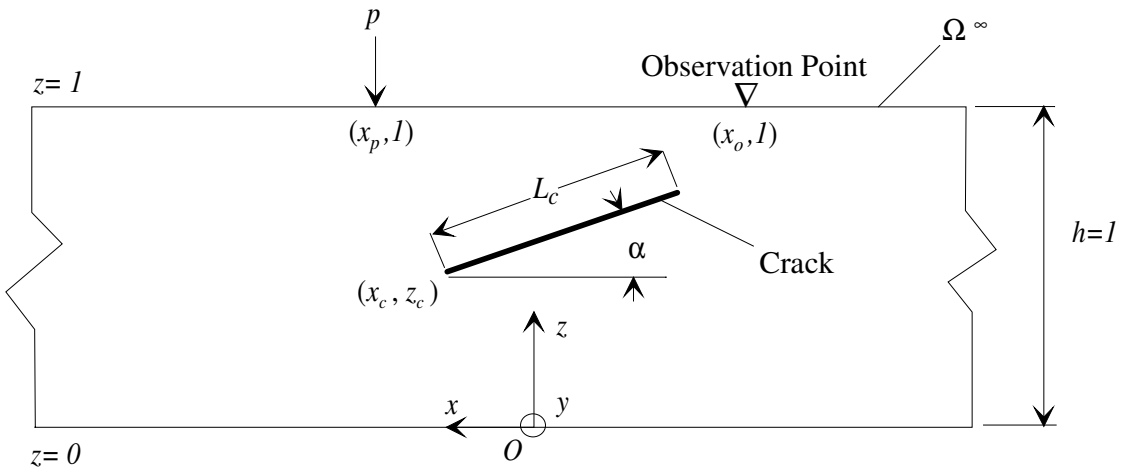

Figure 4.1 A schematic of an infinite, cracked plate subject to a line load

Computational representation of this infinite plate with a combined FE-PML model as shown in Figure 4.2, requires the replacement of the coordinate x by a stretched coordinate, $\bar{x}$, defined in Equation (2.19). Thus, frequency-domain equilibrium equation of the FE-PML model can be written as:

$$\boldsymbol{c}_{xx}\boldsymbol{v}_{,\bar{x}\bar{x}} + \boldsymbol{c}_{xz}\boldsymbol{v}_{,\bar{x}z} + \boldsymbol{c}_{xz}^{T}\boldsymbol{v}_{,z\bar{x}} + \boldsymbol{c}_{zz}\boldsymbol{v}_{,zz} + \omega^{2}\boldsymbol{v} = \boldsymbol{0}. \tag{4.2}$$

Using the chain rule to expand the first three differential terms on the left hand side of Equation (4.2) followed by the evaluation of $x_{,\bar{x}}$ and $x_{,\bar{x}\bar{x}}$ from Equations (2.49) and (2.50) results in

$$\frac{\boldsymbol{c}_{xx}}{\left[j\omega+d\right]^{2}}\boldsymbol{v}_{,xx} - \frac{d_{,x}\,\boldsymbol{c}_{xx}}{\left[j\omega+d\right]^{3}}\boldsymbol{v}_{,x} + \frac{\boldsymbol{c}_{xz}}{j\omega\left[j\omega+d\right]}\boldsymbol{v}_{,xz} + \frac{\boldsymbol{c}_{xz}^{T}}{j\omega\left[j\omega+d\right]}\boldsymbol{v}_{,zx} - \frac{\boldsymbol{c}_{zz}}{\omega^{2}}\boldsymbol{v}_{,zz} = \boldsymbol{v}. \tag{4.3}$$

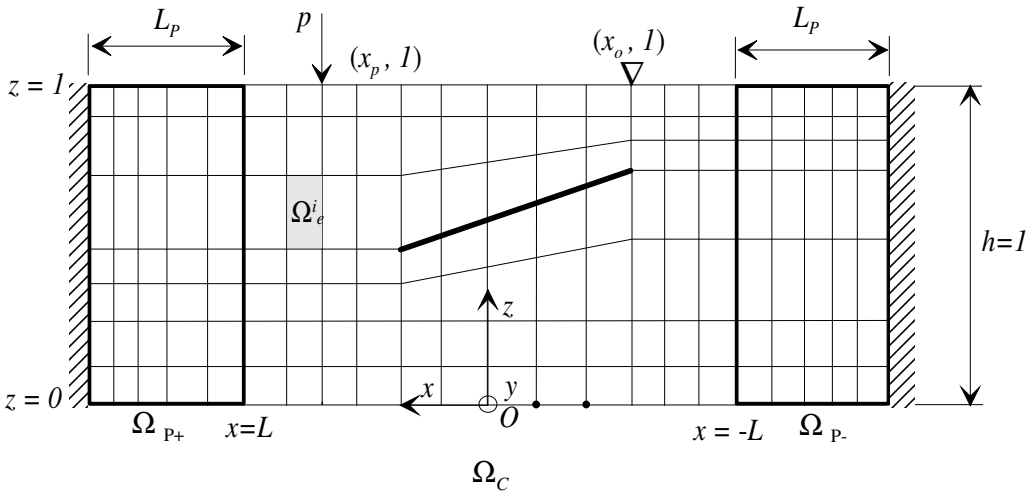

Figure 4.2 A schematic of the FE-PML model of the infinite plate in Figure 4.1

By splitting displacement wave-field [124], Equation (4.3) can be written as

$$\boldsymbol{v} = \boldsymbol{v}_1 + \boldsymbol{v}_2 + \boldsymbol{v}_3 + \boldsymbol{v}_4, \tag{4.4}$$

$$\boldsymbol{c}_{xx}\boldsymbol{v}_{,xx} = \left[j\omega + d \right]^2 \boldsymbol{v}_1, \tag{4.5}$$

$$-d_{,x}\, \boldsymbol{c}_{,xx}\boldsymbol{v}_{,x} = \left[j\omega + d \right]^3 \boldsymbol{v}_2, \tag{4.6}$$

$$\boldsymbol{c}_{xz}\boldsymbol{v}_{,xz} + \boldsymbol{c}_{xz}^T\boldsymbol{v}_{,zx} = j\omega\left[j\omega + d \right]\boldsymbol{v}_3, \tag{4.7}$$

$$\boldsymbol{c}_{zz}\boldsymbol{v}_{,zz} = -\omega^2\boldsymbol{v}_4. \tag{4.8}$$

Inverse Fourier transformation of Equations (4.5) through (4.8) yields the following displacement-based governing equations in the time domain

$$\ddot{\bar{\boldsymbol{v}}}_1 = \boldsymbol{c}_{xx}\boldsymbol{v}_{,xx}, \tag{4.9}$$

$$\ddot{\bar{\boldsymbol{v}}}_5 = -d_{,x}\boldsymbol{c}_{xx}\ \boldsymbol{v}_{,x}, \tag{4.10}$$

$$\boldsymbol{v}_5 = \dot{\bar{\boldsymbol{v}}}_2, \tag{4.11}$$

$$\boldsymbol{c}_{xz}\boldsymbol{v}_{,xz} + \boldsymbol{c}_{xz}^T\boldsymbol{v}_{,zx} = \dot{\bar{\boldsymbol{v}}}_3 = \frac{\partial}{\partial t}\left(\frac{\partial}{\partial t} + d\right)\boldsymbol{v}_3, \tag{4.12}$$

$$\boldsymbol{c}_{zz}\boldsymbol{v}_{,zz} = \ddot{\boldsymbol{v}}_4. \tag{4.13}$$

In a standard FE procedure, the entire problem domain is divided into a finite number, n_e, of non-overlapping elements, Ω_e^i $(i = 1...n_e)$. Approximations to the solutions of Equations (4.9)-(4.13) are expressed over each element in terms of element nodal values and piecewise-continuous, linearly-independent basis functions, n_l $(l = 1...n_n^e)$ with n_n^e being the number of nodes in an element. Following a Galerkin method in eliminating the integral of the weighted approximation residuals over the entire problem domain, where basis functions are used as weights, results in the following FE form of Equations (4.9)-(4.13)

$$\begin{aligned} \boldsymbol{Q} &= \boldsymbol{Q}_1 + \boldsymbol{Q}_2 + \boldsymbol{Q}_3 + \boldsymbol{Q}_4, \\ \boldsymbol{Q} &= \left\{u_1 \quad w_1 \quad ... \quad u_{n_n} \quad w_{n_n}\right\}, \\ \boldsymbol{Q}_i &= \left\{u_{i(1)} \quad w_{i(1)} \quad ... \quad u_{i(n_n)} \quad w_{i(n_n)}\right\};\ i = 1...4, \end{aligned} \tag{4.14}$$

$$\boldsymbol{M}\ddot{\boldsymbol{Q}}_1 = -\boldsymbol{K}_1\boldsymbol{Q}, \tag{4.15}$$

$$\boldsymbol{M}\ddot{\boldsymbol{Q}}_5 = -\boldsymbol{K}_2\boldsymbol{Q}, \tag{4.16}$$

$$\boldsymbol{Q}_5 = \dot{\boldsymbol{Q}}_2, \tag{4.17}$$

$$\boldsymbol{M}\dot{\boldsymbol{Q}}_3 = -\boldsymbol{K}_3\boldsymbol{Q}, \tag{4.18}$$

$$\boldsymbol{M}\ddot{\boldsymbol{Q}}^4 = \boldsymbol{P} - \boldsymbol{K}_4\boldsymbol{Q}. \tag{4.19}$$

In Equation (4.14), n_n is the number of global nodes in the FE mesh. Stiffness matrices, $\boldsymbol{K}_i$ $(i = 1...4)$, mass matrix, $\boldsymbol{M}$, and consistent load vector, $\boldsymbol{P}$, are obtained by standard FE assembly of the corresponding element-level matrices as follows:

$$\boldsymbol{K}_1 = \prod_{i=1}^{n_e} \boldsymbol{k}_1^i, \quad \boldsymbol{k}_1^i = \sum_{l=1}^{n_n^e} \int_{\Omega_e^i} n_{k,x} \boldsymbol{c}'_{xx} n_{l,x} dxdz, \tag{4.20}$$

$$\boldsymbol{K}_2 = \prod_{i=1}^{n_e} \boldsymbol{k}_2^i, \quad \boldsymbol{k}_2^i = \sum_{l=1}^{n_n^e} \int_{\Omega_e^i} n_k d_{,x} \boldsymbol{c}'_{xx} n_{l,x} dxdz, \tag{4.21}$$

$$\boldsymbol{K}_3 = \prod_{i=1}^{n_e} \boldsymbol{k}_3^i, \quad \boldsymbol{k}_3^i = \sum_{l=1}^{n_n^e} \int_{\Omega_e^i} \left[n_{k,x} \boldsymbol{c}'_{xz} n_{l,z} + n_{k,z} \boldsymbol{c}'_{xz} n_{l,x} \right] dxdz, \tag{4.22}$$

$$\boldsymbol{K}_4 = \prod_{i=1}^{n_e} \boldsymbol{k}_4^i, \quad \boldsymbol{k}_4^i = \sum_{l=1}^{n_n^e} \int_{\Omega_e^i} n_{k,z} \boldsymbol{c}'_{zz} n_{l,z} dxdz, \tag{4.23}$$

$$\boldsymbol{M} = \prod_{i=1}^{n_e} \boldsymbol{m}^i, \quad \boldsymbol{m}^i = \sum_{l=1}^{n_n^e} \int_{\Omega_e^i} n_k \boldsymbol{I}_2 \, n_l dxdz, \tag{4.24}$$

$$\boldsymbol{P} = \prod_{i=1}^{n_e} \boldsymbol{p}^i, \quad \boldsymbol{p}^i = \int_{\Omega_e^i} n_k \boldsymbol{I}_2 \, p\delta\left(x_p\right) dx; \quad k = 1,....,n_n^e, \tag{4. 25}$$

$$\boldsymbol{c}'_{kl} = \boldsymbol{I}_2 \boldsymbol{c}_{kl} \boldsymbol{I}_2; \quad \boldsymbol{I}_2 = \begin{bmatrix} 1 & 0 \\ 0 & 1 \end{bmatrix}; \quad k, l = x, z. \tag{4.26}$$

Inside Ω, standard FE equations corresponding to (4.2) can be integrated using a Newmark explicit scheme. Inside Ω_{P-} and Ω_{P+}, Equations (4-15)-(4-19) can be integrated in the followings steps:

$$\ddot{\boldsymbol{Q}}_{1(i+1)} = \frac{-\boldsymbol{M}^{-1}\boldsymbol{K}_1\boldsymbol{Q} - d\left\{ d\boldsymbol{Q}_{1(i)} + \left[1 + \frac{d\Delta t}{2}\right]\left[\ddot{\boldsymbol{Q}}_{1(i)}\Delta t + 2\dot{\boldsymbol{Q}}_{1(i)}\right]\right\}}{\left[1 + d\Delta t + (d\Delta t)^2\right]}, \tag{4.27}$$

$$\dot{\boldsymbol{Q}}_{1(i+1)} = \dot{\boldsymbol{Q}}_{1(i)} + \frac{\ddot{\boldsymbol{Q}}_{1(i)} + \ddot{\boldsymbol{Q}}_{1(i+1)}}{2}\Delta t, \tag{4.28}$$

$$\boldsymbol{Q}_{1(i+1)} = \boldsymbol{Q}_{1(i)} + \left(\dot{\boldsymbol{Q}}_{1(i+1)} + \frac{\ddot{\boldsymbol{Q}}_{1(i+1)}}{2}\Delta t\right)\Delta t, \tag{4.29}$$

$$\ddot{\boldsymbol{Q}}_{5(i+1)} = \frac{-\boldsymbol{M}^{-1}\boldsymbol{K}_1\boldsymbol{Q} - d\left\{ d\boldsymbol{Q}_{5(i)} + \left[1 + \frac{d\Delta t}{2}\right]\left[\ddot{\boldsymbol{Q}}_{5(i)}\Delta t + 2\ddot{\boldsymbol{Q}}_{5(i)}\right]\right\}}{\left[1 + d\Delta t + (d\Delta t)^2\right]}, \tag{4.30}$$

$$\dot{\boldsymbol{Q}}_{5(i+1)} = \dot{\boldsymbol{Q}}_{5(i)} + \frac{\ddot{\boldsymbol{Q}}_{5(i)} + \ddot{\boldsymbol{Q}}_{5(i+1)}}{2}\Delta t, \tag{4.31}$$

$$\boldsymbol{Q}_{5(i+1)} = \boldsymbol{Q}_{5(i)} + \left(\dot{\boldsymbol{Q}}_{5(i+1)} + \frac{\ddot{\boldsymbol{Q}}_{5(i+1)}}{2}\Delta t\right)\Delta t, \tag{4.32}$$

$$\boldsymbol{Q}_{2(i+1)} = \frac{\left(\boldsymbol{Q}_{2(i)} + \boldsymbol{Q}_{5(i+1)}\Delta t\right)}{(1 + d\Delta t)}, \tag{4.33}$$

$$\ddot{\boldsymbol{Q}}_{3(i+1)} = \frac{\text{-}\boldsymbol{M}^{-1}\boldsymbol{K}_3\boldsymbol{Q} - d\dot{\boldsymbol{Q}}_{3(i)} - \frac{d\ddot{\boldsymbol{Q}}_{3(i)}}{2}\Delta t}{\left[1 + \frac{d\Delta t}{2}\right]}, \tag{4.34}$$

$$\dot{\boldsymbol{Q}}_{3(i+1)} = \dot{\boldsymbol{Q}}_{3(i)} + \frac{\ddot{\boldsymbol{Q}}_{3(i)} + \ddot{\boldsymbol{Q}}_{3(i+1)}}{2}\Delta t, \tag{4.35}$$

$$\boldsymbol{Q}_{3(i+1)} = \boldsymbol{Q}_{3(i)} + \left(\dot{\boldsymbol{Q}}_{3(i+1)} + \frac{\ddot{\boldsymbol{Q}}_{3(i+1)}}{2}\Delta t\right)\Delta t, \tag{4.36}$$

$$\ddot{\boldsymbol{Q}}_{4(i+1)} = \boldsymbol{P} - \boldsymbol{M}^{-1}\boldsymbol{K}_4\boldsymbol{Q}, \tag{4.37}$$

$$\dot{\boldsymbol{Q}}_{4(i+1)} = \dot{\boldsymbol{Q}}_{4(i)} + \frac{\ddot{\boldsymbol{Q}}_{4(i)} + \ddot{\boldsymbol{Q}}_{4(i+1)}}{2}\Delta t, \tag{4.38}$$

$$\boldsymbol{Q}_{4(i+1)} = \boldsymbol{Q}_{4(i)} + \left(\dot{\boldsymbol{Q}}_{4(i+1)} + \frac{\ddot{\boldsymbol{Q}}_{4(i+1)}}{2}\Delta t\right)\Delta t. \tag{4.39}$$

The FE-PML model was programmed into a FORTRAN 90 computer code. The code was executed on a Dell Precision M6300 for several example problems. Results are presented and discussed next.

4.3 Numerical Implementation and Validation

Accuracy and stability of the FE modeling of elastic wave motion is dependent on element dimensions, Δx and Δz. Several recommendations [137] suggest a minimum of eight linear or four quadratic elements per shortest wave length in order to correctly cap-

ture a waveform. We will refer to this later as the eight-element rule. Moreover, stability of explicit time integration is critically dependent on time step, Δt. A stable time step is given in terms of element dimensions, Δx and Δz, and pressure wave speed, c_p, as follows [138]

$$\Delta t \le \frac{1}{c_p}\left(1/\Delta x^2 + 1/\Delta z^2\right)^{-1/2}. \tag{4.40}$$

Basu [129] has found a stable time step for the FE model to remain stable in a combined FE-PML model. The real damping profile in the PML region assumes the form given in Equation (3.76) [128]. In all numerical examples throughout this chapter, d_0 and m are tentatively kept at 10 and 1, respectively. In the following, numerical results are presented to verify reciprocity satisfaction of both the FE and the FE-PML predictions and to establish their validity against available literature data. Time history responses are predicted at $(5,1)$ due to a loading at $(-5,1)$ in the form of a modulated Gaussian signal whose time history is given by:

$$p(t) = \frac{2}{\sigma_G\sqrt{2\pi}}\exp\left[-\frac{(t-t_0)^2}{2\sigma^2}\right]\sin(\omega_c t). \tag{4.41}$$

In Equation (4.41), σ_G is a parameter controlling the width of the pulse, t_0 determines the time delay, and ω_c is the center angular frequency. In this example, parameters $\sigma_G = 0.8$, $t_0 = 3$, $\omega_c = 3.14$ are chosen. Time history and frequency spectrum of a Gaussian signal corresponding to these values are shown in Figure 4.3.

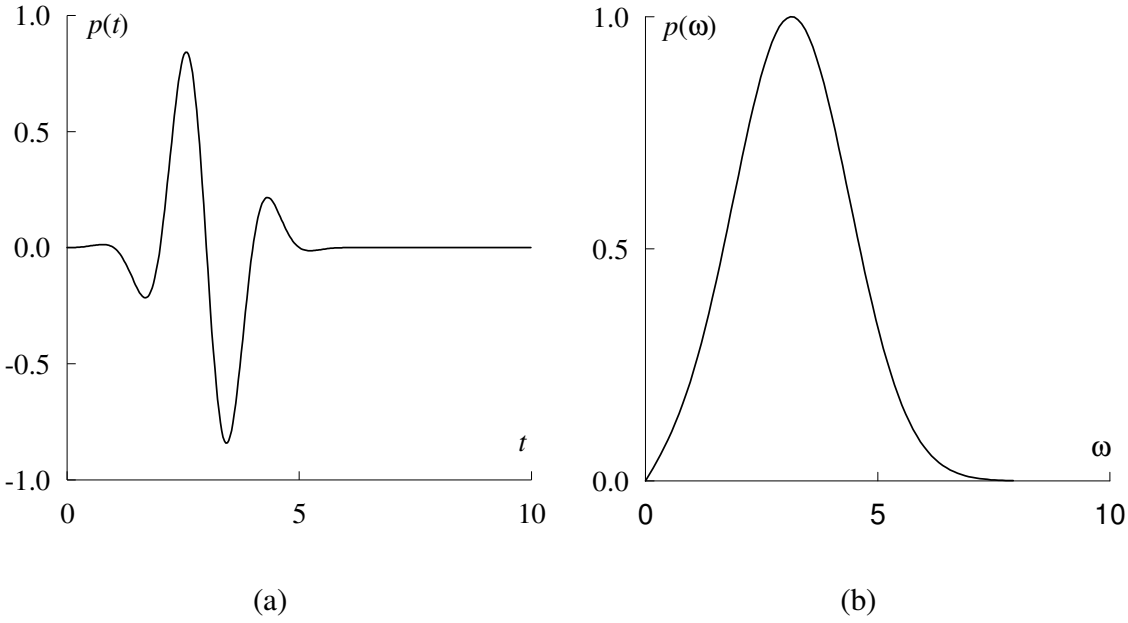

Figure 4.3 A modulated Gaussian signal (a) time history and (b) frequency spectrum

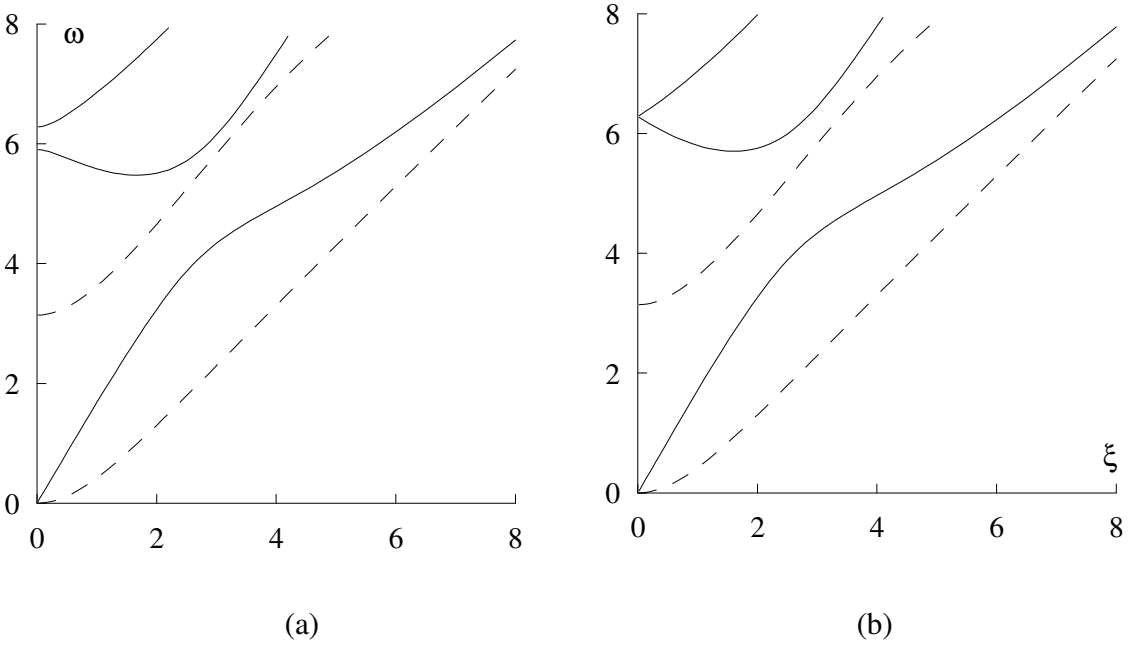

Figure 4.4 Frequency spectra for (a) the nickel layer and (b) aluminum plate (____ symmetric modes; ------- anti-symmetric modes)

Two sets of predictions were reported in the literature for this loading-observation scenario. The first was reported by Pan and Datta [35] for a $100\mu m$-thick, nickel layer whose dimensional properties were given as $\underline{c}_{11} = \underline{c}_{22} = 298.95$ GPa, $\underline{c}_{12} = 129.53$ GPa, $\underline{c}_{55} = 84.71$ GPa, and $\underline{\rho} = 8910$ kg/m^3. The second was reported by Liu and Achenbach [139] for an aluminum plate whose Poisson's ratio is $1/3$. Pan and Datta obtained their predictions analytically. Liu and Achenbach employed the SEM and corroborated their results with those of the HNM. Dimensionless frequency spectra of the nickel and aluminum plates are shown in Figure 4.4.

Frequency band upper limit of the exciting signal at $\omega = 7$, Figure 4.3b, corresponds a maximum wavenumber $\xi = 8$ for both plates, Figure 4.4, i.e. a minimum wavelength $(\lambda = 2\pi/\xi)$ of about 0.8. Following the eight-element rule and Equation (4.40), a uniform FE mesh of 0.1-by-0.1 elements and a time step of 0.03 are employed to obtain the results presented in this section. Reciprocity is verified for the FE $(L = 15)$ and FE-PML $(L = 5.1; L_p = 1.9)$ models by predicting vertical, top-surface displacement, w, at $(5,1)$ due to a vertical point load at $(-5,1)$ and vice versa. Two sets of such predictions for the nickel and the aluminum plates are shown in Figures 4.5 and 4.6, respectively. They are so indistinguishable that reciprocity is evidently satisfied. Figure 4.7a shows the horizontal top-surface displacement at $(5,1)$ in the nickel layer due to a horizontal load at $(-5,1)$. Both the FE and the FE-PML results are in good agreement with corresponding analytical

predictions reported by Pan and Datta [35]. Figure 4.7b depicts horizontal top-surface displacement at $(5,1)$ in the aluminum plate due to a horizontal load at $(-5,1)$. Similarly, the FE and the FE-PML predictions are in decent agreement with its counterparts reported by Liu and Achenbach. The CPU times elapsed during the FE (3000 elements) and the FE-PML (1400 elements) runs are: 772 and 498.2 seconds, respectively, thus saving 35.5 % of CPU time by using the latter.

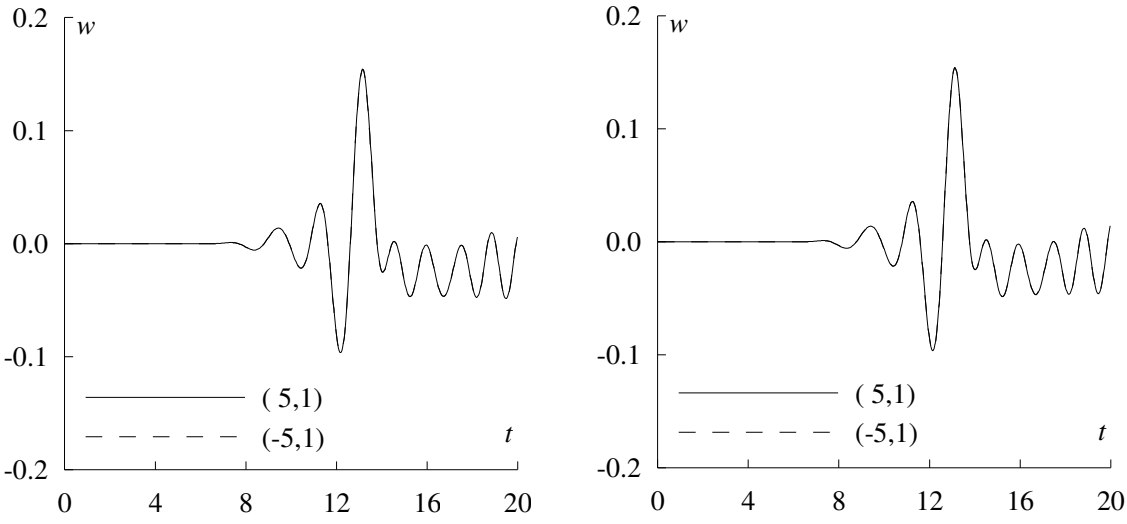

Figure 4.5. Reciprocity check of (a) FE and (b) FE-PML predictions in the nickel layer

4.4 Applications to Crack Characterization

The following numerical examples demonstrate some applications of the proposed FE-PML model to numerical modeling of elastic PSV wave scattering in the context of 2D crack characterization.

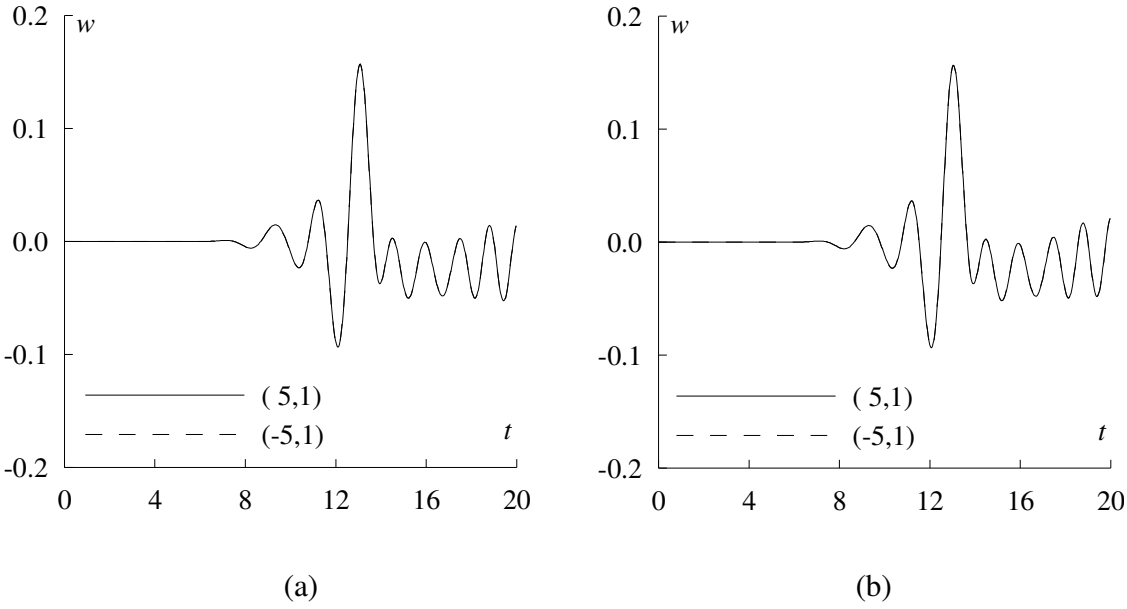

Figure 4.6 Reciprocity check of (a) FE and (b) FE-PML predictions in the aluminum plate

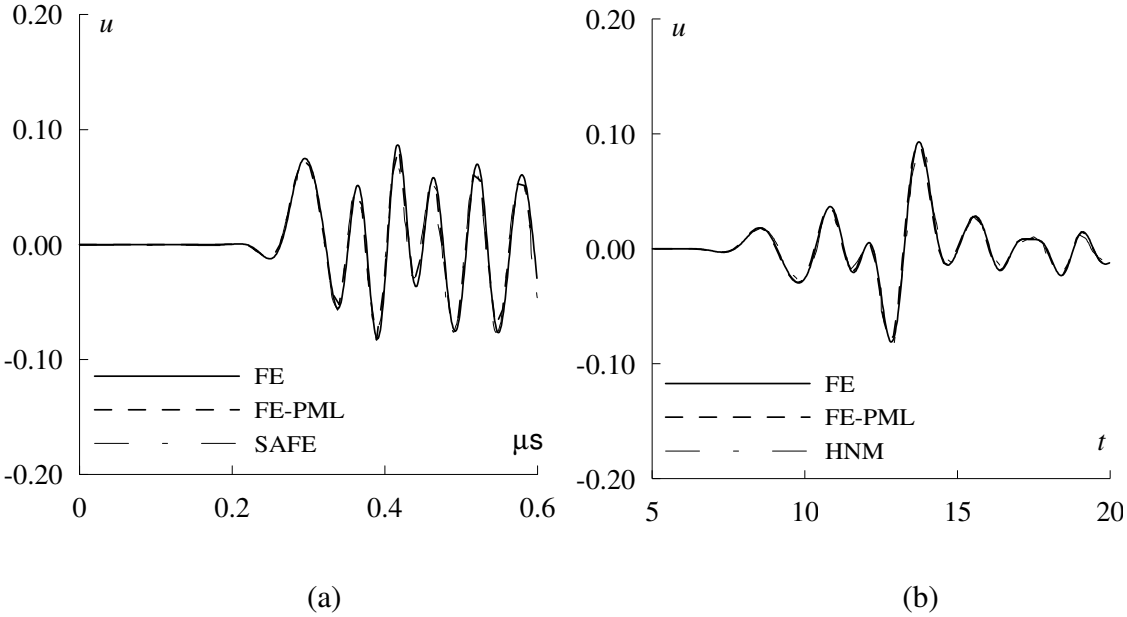

Figure 4.7 Horizontal top-surface displacements at (5,1) due to (a) a horizontal load at (-5,1) in the nickel layer and (b) a vertical load at (-5,1) in the aluminum plate.

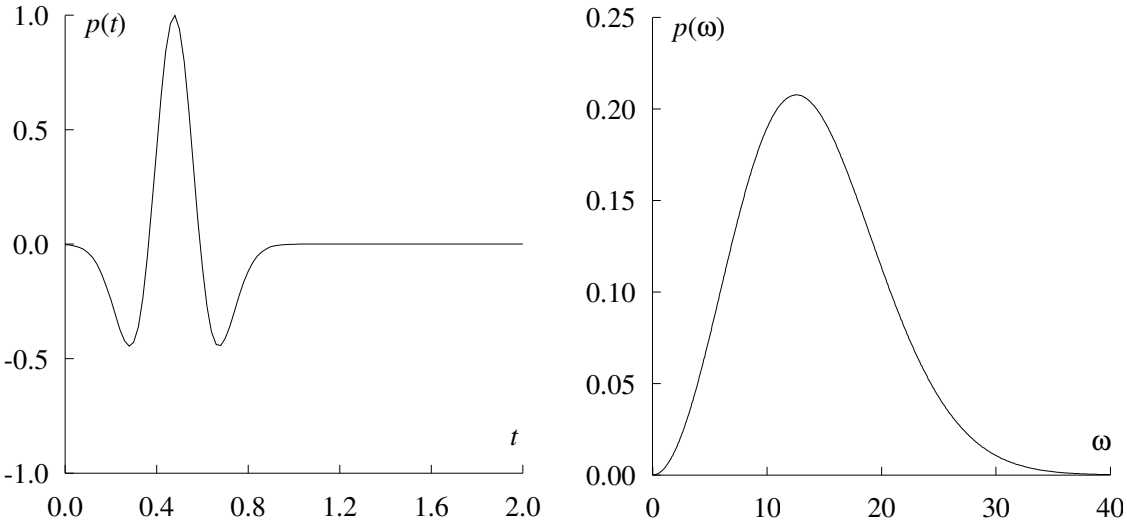

(a) (b)

Figure 4.8 A Ricker wavelet (a) time history and (b) frequency spectrum for Example 1

Example 1: A vertically cracked, 175-*mm* thick isotropic concrete slap is considered. The vertical crack opens to the bottom surface of the slab. The crack tip lies at $x_c = (0, 0.5)$, i.e. $L_c = 0.5$. Density and Poisson's ratio of concrete are taken as $2500\ \text{kg/m}^3$ and 0.15, respectively. The slab is excited by a Ricker wavelet in the form:

$$p(t) = \left[1 - 2\pi^2 \omega_{\bar{c}}^2 \left(t - \frac{3\pi}{\omega_{\bar{c}}}\right)\right] \exp\left[-\pi^2 \omega_{\bar{c}}^2 \left(t - \frac{3\pi}{\omega_{\bar{c}}}\right)\right]. \tag{4.42}$$

Time history and Fourier transform of a Ricker wavelet corresponding to $\omega_{\bar{c}} = 2$ is shown in Figure 4.8. Figure 4.9a shows frequency spectra for the concrete slab in this example. At the maximum significant frequency present in the exciting impact $\omega = 25$, see Figure 4.8b, the wavenumber is, approximately, 14. That corresponds to a wavelength of

0.45. Following the eight-element rule and Equation (4.40), a uniform mesh $(\Delta x = \Delta z = 0.05)$ and a time step of 0.008 are employed in the current example. Convergence of the FE-PML predictions of vertical top-surface displacement at $(0.1,1)$ due to a point load at $(-0.1,1)$ for this discretization values is confirmed by comparing the results for $\Delta x = \Delta z = 0.1,\ 0.05,$ and 0.04, see Figure 4.9b. Predictions of displacement time histories in response to a vertical load are obtained by FEA with PMLs $(L = 1,\ L_p = 1)$ and without PMLs $(L = 5)$. Displacement time history responses at $x_o = (0.2,1)$ to a vertical line load at $x_p = (-0.2,1)$ are shown in Figure 4.10, with very good agreement between the FE and the FE-PML predictions. It took the FE (8000 elements) and the FE-PML (1600 elements) executions 807.79 and 333.84 seconds of CPU time, respectively. That is a 58.7 % saving in CPU time. Obviously, a relatively larger FE model dictated by a high-frequency excitation and a smaller FE-PML model due to load-observation closeness resulted in a higher saving in CPU time. Thus, FE-PML can allow a comprehensive study of the effect of crack presence on response time histories at a reasonable computational cost.

Let us consider another loading-observation scenario. A vertical line load is applied to the bottom surface of the slab at $x_p = -0.1$. Time history of vertical displacement, w, on the slab's bottom surface, is predicted at $x_o = 0.1$ by the FE-PML model for several values of crack length, L_c. Predictions are shown in Figure 4.11a. The effect of the crack length on the arrival time, T, is evident. Figure 4.11b is a plot of the arrival time, T, versus the

crack length, L_c. The relationship between T and L_c is *tri-linear*. Arrival time is insensitive to crack lengths less than or equal to 0.1. For crack lengths between 0.1 and 0.7, the arrival time increases with the crack length at a constant rate. This rate increases at $L_c = 0.7$. This proportionality between the time delay of the transmitted wave and a crack's depth confirms what has been experimentally reported by Hudgell et al. [140].

Example 2: Consider a delaminated, 6.35-*mm* thick, 0^o (bottom)/90^o (top) graphite-epoxy laminate. Geometric and material properties of the laminate are given in Table 1. Results are obtained by FEA with PMLs ($L = 1.1, L_p = 0.9$) and without PMLs ($L = 6$). From Figure 4.12b and 4.13a, the shortest wavelength is calculated to be 0.4. Following the eight-element rule and Equation (4.40), a uniform 0.05-by-0.05 FE mesh and time step of 0.005 are used in this example. Convergence for these discretization values is evident from Figure 4.13b.

Time histories of top-surface displacements at $x_o = 0.75$ due to a line load at $x_p = -0.75$ are predicted by FE (4800 elements) and FE-PML (1760 elements) models with CPU time consumptions of 4299.94 seconds and 1985.96 seconds, respectively. Thus, a 53.8 % of the CPU time consumed by the former can be saved by using the latter. Results are in very good agreement as shown in Figure 4.14. The FE-PML model is further used to conduct a study of the effect of load-observation separation distance, *D*, on arrival time, *T*, of bottom-surface vertical displacement response due to a vertical line load applied to the top surface of the laminate. Four load-observation configurations considered in this

study are summarized in Table 4.2 and illustrated in Figure 4.15 *with the shadow zone of a crack geometrically illustrated.*

Table 4.1 Material and configuration of the graphite-epoxy laminate in Example 2

Lamina	$\underline{h}$	$\underline{\rho}$	$\underline{c}_{11}$	$\underline{c}_{12}$	$\underline{c}_{22}$	$\underline{c}_{55}$
	mm	$10^3 kg/m^3$	*GPa*	*GPa*	*GPa*	*GPa*
0^o	3.175	1.578	160.72	6.43	13.91	7.07
90^o	3.175	1.578	13.91	6.91	13.91	3.49

Figure 4.16a shows the time of arrival, *T*, versus crack length for the four configurations. It is evident that the closer the observation point is to the load, the more distinct the change in time of arrival becomes. It is noticeable also that each curve exhibits an abrupt increase in arrival time for different values of the crack length, L_c. Figure 4.16b shows variation in arrival time, *T*, with load-observation separation distance, *D*. As the separation distance increases, the time of arrival becomes insensitive to smaller crack lengths. This is a clear indication that a varying arrival time, *T*, belongs, indeed, to a crack-tip diffracted wave not a transmitted one. Thus, for a fixed load-observation separation, there is a critical crack length below which the observation point is no longer inside the shadow zone of the crack, see Figure 4.15. For configuration 1 and 2, these critical lengths are 0.8 and 0.4, respectively.

Table 4.2 Load-observation configurations

Configuration	1	2	3	4
Load	(-0.75,1)	(-0.50,1)	(-0.25,1)	(0,1)
Observation	(0.75,0)	(0.50,0)	(0.25,0)	(0,0)
D	1.5	1	.5	0

4.5 Conclusions

This chapter has successfully proven the applicability a combined, split-field PML and FE approach to numerical modeling of PSV wave propagation and scattering in infinite plates. Results are in good agreement with available analytical and semi analytical solutions. The FE-PML offers an economical computational tool for analyzing elastic PSV wave scattering problems in infinite plates. Saving in CPU times is application-dependent.

For applications considered in this chapter, the CPU time savings by the FE-PML model range between 29% and 87 % of the CPU time needed to run a corresponding FEA. Application of the proposed technique has been used to study the correlation between the arrival time of crack-tip diffraction and crack depth or delamination length. Such studies are crucially helpful in setting experimental parameters or analyzing measured NDT data.

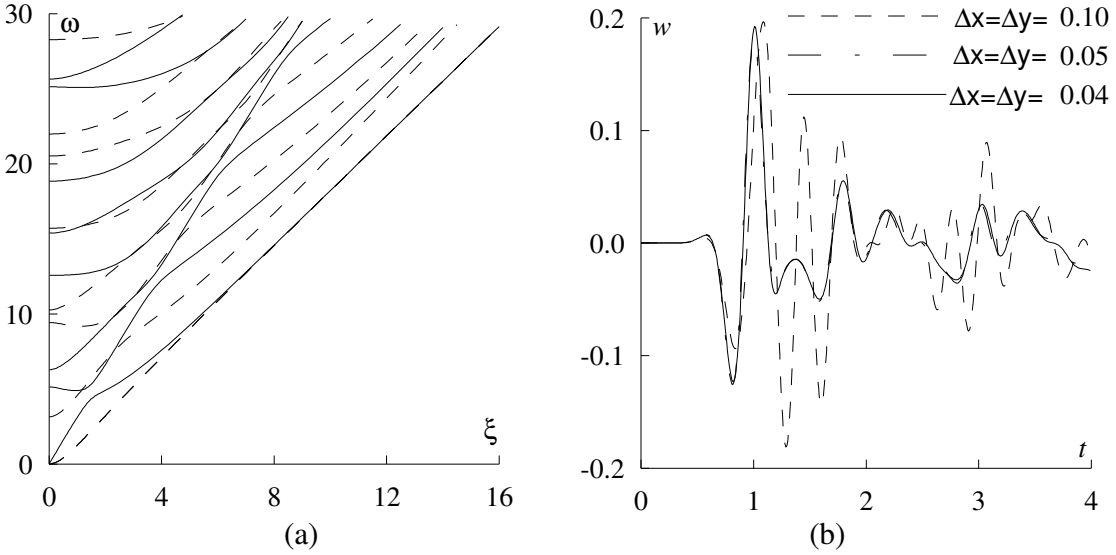

Figure 4.9 (a) Frequency spectra in the concrete slab; (b) vertical top-surface displacement at (0.1,1) due to a point load at (-0.1,1) is nearly invariant to further mesh refinement.

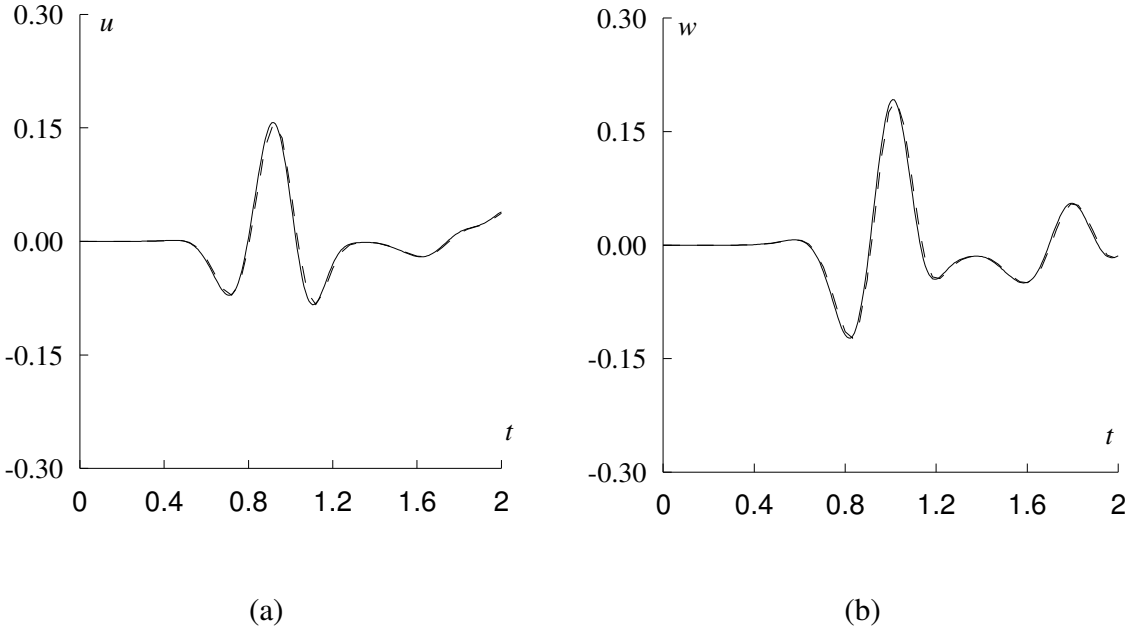

Figure 4.10 : Horizontal (a) and vertical (b) displacement time-histories at (0.2,1) due to a line load at (-0.2,1) in the flawless concrete slab predicted by FE (dashed) and FE-PML (solid)

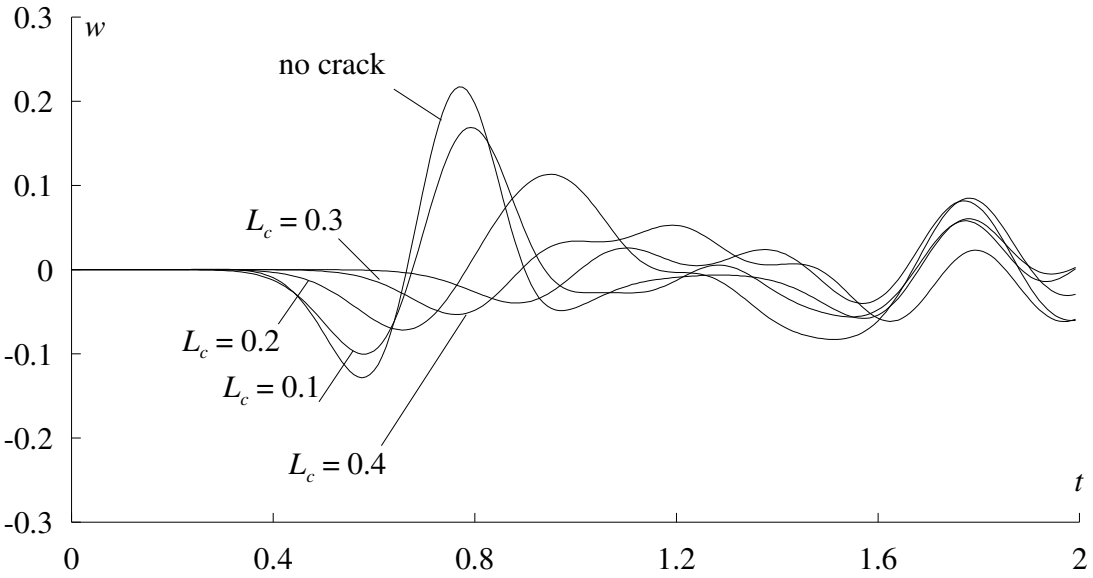

(a)

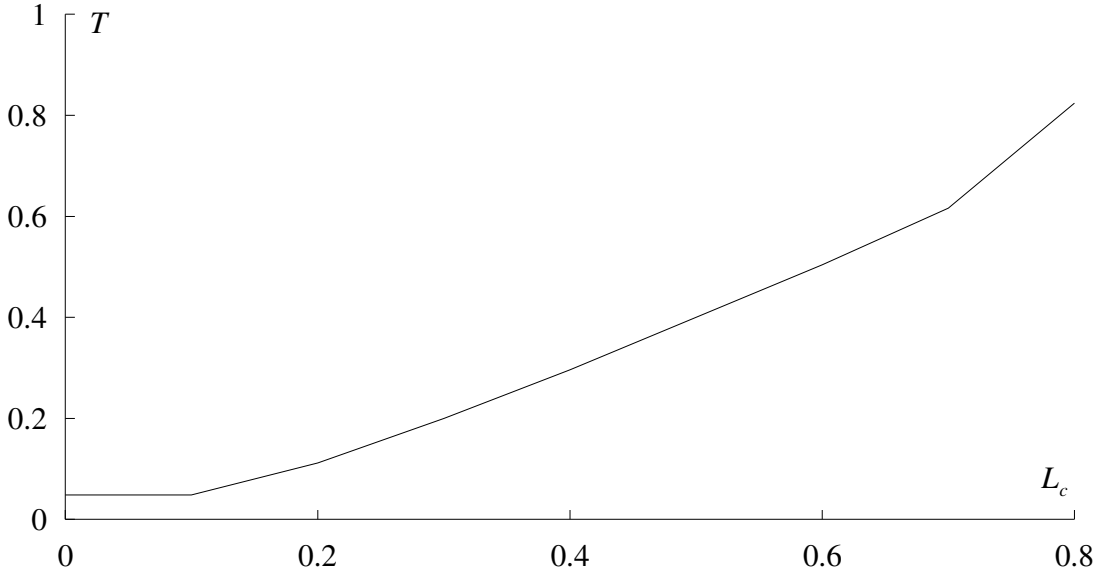

(b)

Figure 4.11 Plots of (a) vertical displacement time histories at (0.1, 0) due to a vertical line load at (-0.1, 1) for different values of crack length, L_c; (b) corresponding arrival time, T, plotted versus crack length, L_c

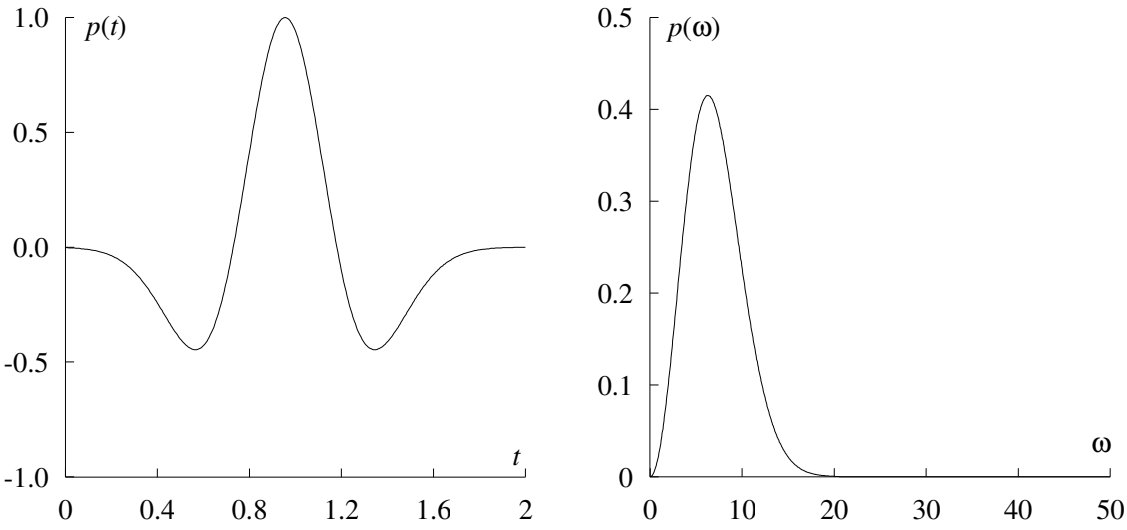

(a) (b)

Figure 4.12 A Ricker wavelet (a) time history and (b) frequency spectrum for Example 2

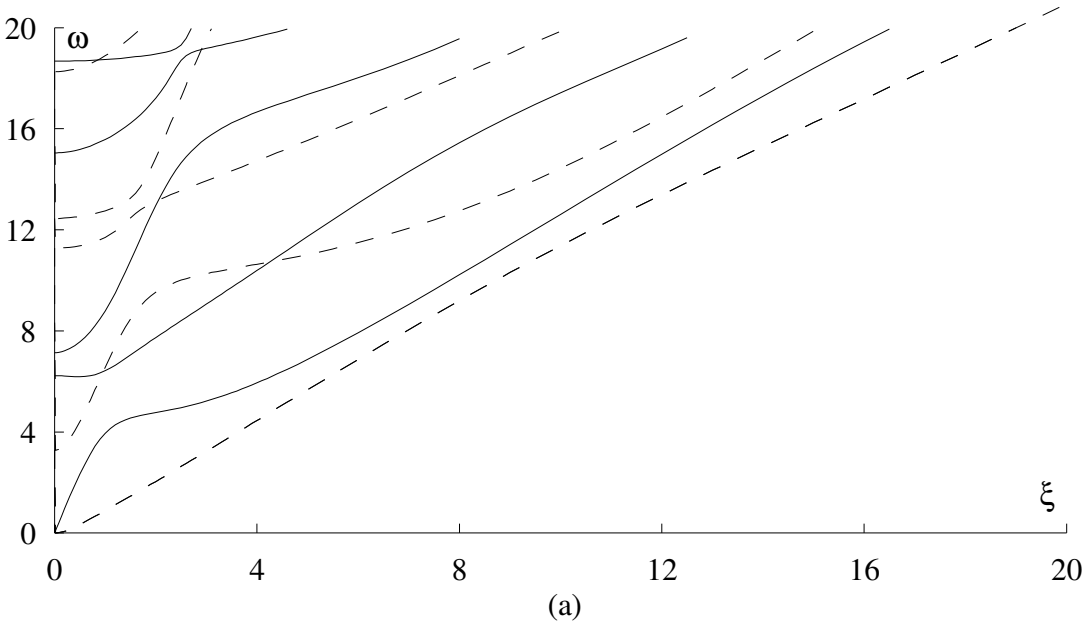

(a)

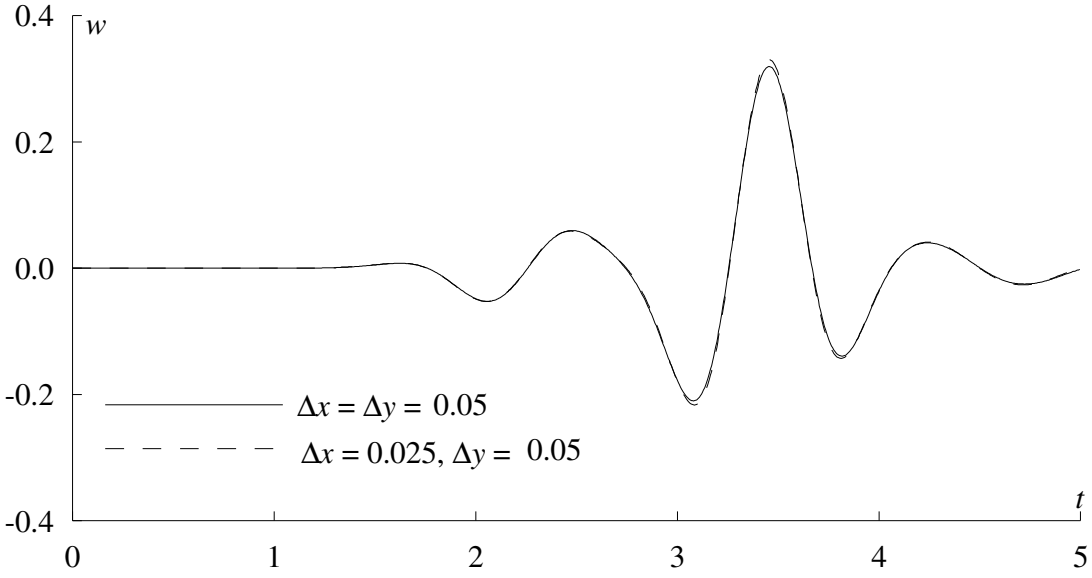

(b)

Figure 4.13 Plots of (a) frequency spectra in the graphite-epoxy laminate and (b) vertical top-surface displacement at (0.75, 1) due to a point load at (-0.75, 1) is nearly invariant to further mesh refinement.

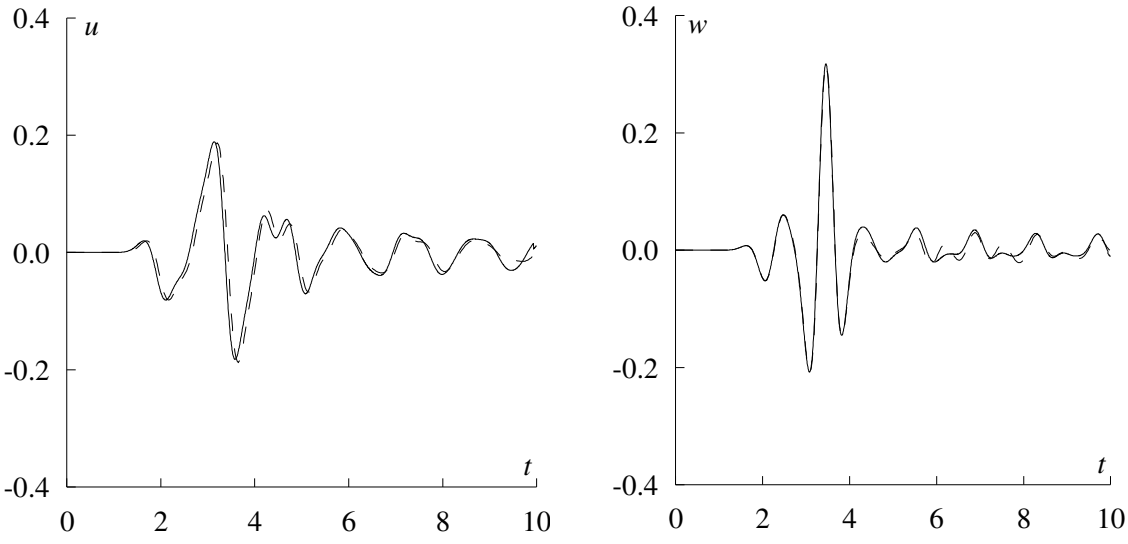

(a) (b)

Figure 4.14 (a) Horizontal and (b) vertical displacements at (0.75, 1) due to a vertical line load at (-0.75, 1) are predicted by FE (dashed line) and FE-PML (solid line)

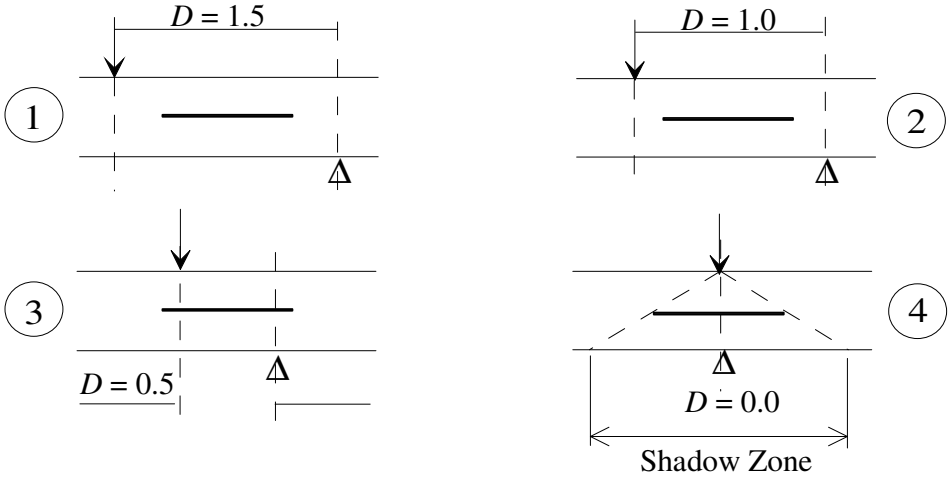

Figure 4.15 Illustrations of the load-observation configurations listed in Table 2 and what is meant by the shadow zone of a crack.

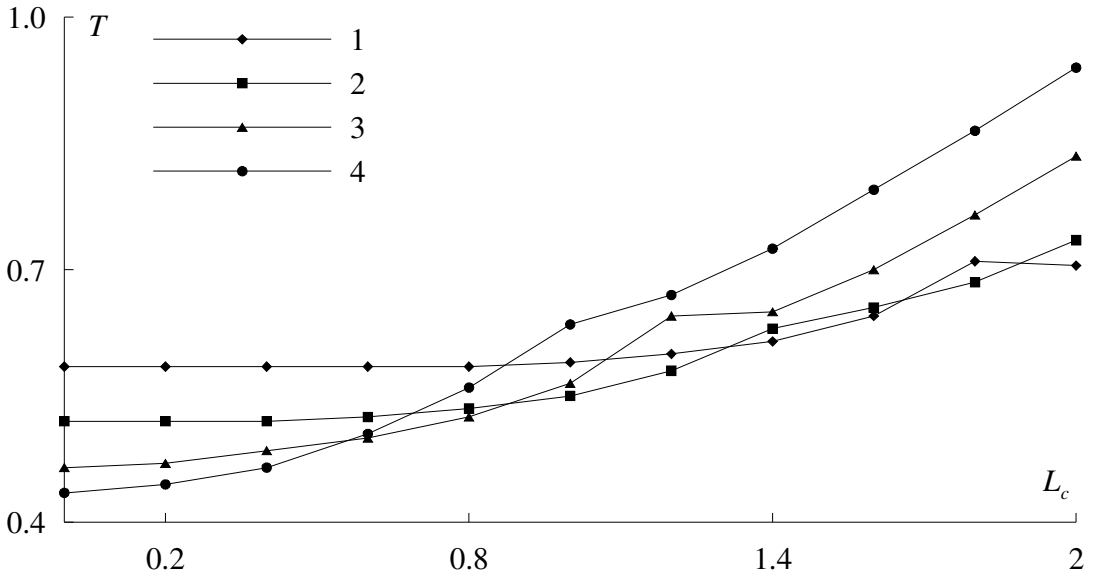

(a)

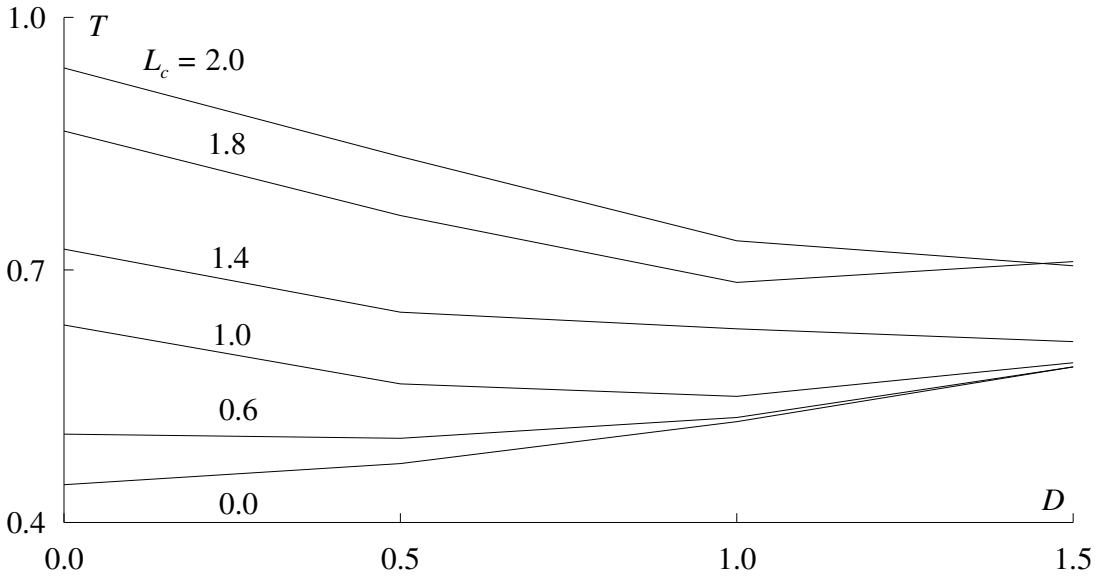

(b)

Figure 4.16 Variations in arrival time, T: (a) with load-observation separation distance, D, for several delamination lengths and (b) with delamination length for several load-observation configurations.

"Even the best needles are not sharp at both ends." Chinese Proverb

Chapter 5

3D Waves in Infinite Plates with Rectangular Cross Sections

This chapter applies the FE-PML model to 3D scattering of transient elastic waves in a cracked infinite plate with rectangular cross section. FE predictions are validated against semi-analytical literature results. The effects of PML parameters on the RMS error are evaluated against reference EMFE predictions. The proposed model is shown, through numerical examples, to offer a huge saving in real run-time at a slight degradation in accuracy. Practical applications indicate its potential in modeling elastic-wave-based NDE of engineering plate structures.

5.1 Description of the Problem

The subject of the current study is an infinite plate with a uniform dimensionless thickness, h, and a finite dimensionless width, b. The plate is described by a rectangular coordinate system (x, y, z). The x-axis lies along the plate's infinite dimension. The origin of the coordinate system coincides with the center of plate's cross section. Figure 5.1 shows a horizontally-cracked plate subject to a line load in the negative z-direction along the y-axis. The plate is assumed to be symmetrical about the y-z plane, therefore, only half of the plate is shown. Since information about propagating modes in the flawless unloaded plate are required for determining adequate FE discretization, free elastic waves in finite-width plates are discussed next.

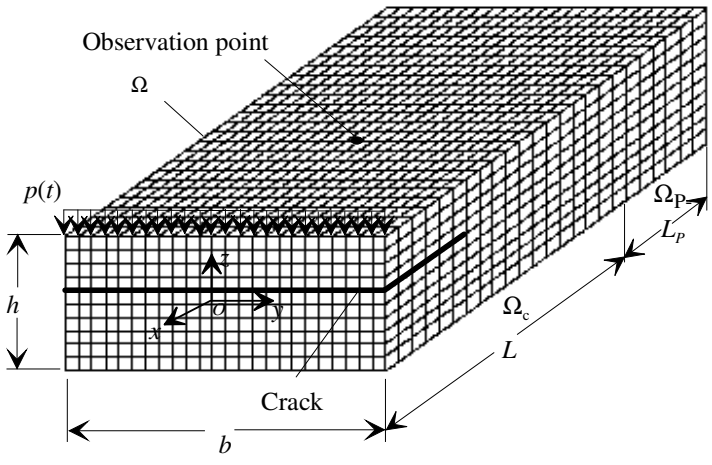

Figure 5.1 An FE-PML representation of an infinite cracked plate with rectangular cross-section subject to a vertical load along the y-axis

5.2 Free Elastic Waves in Finite-width Plates

Elastic wave propagation in finite-width plates has been studied by several researchers. Sample literature may include the early work of Nigro [141] and the latter works of Onipede and Dong [26], Taweel et al. [142], and Mukdadi et al. [143] The latter works are based on a SAFE technique. A brief description of this technique is presented here for completeness. The reader may refer to relevant literature for details. In the SAFE technique [144], the cross section of a plate is modeled by 2D finite elements. The y- and z-dependence of the displacement field is interpolated over each element in terms of element nodal displacements and Lagrangian shape functions. Propagation in the infinite, x, direction is modeled by analytical wave functions. The governing equations of motion are then derived by using Hamilton's principle leading to a generalized eigenvalue problem in the frequency-wavenumber domain. When a propagating wavenumber is specified, these equations are solved for unknown frequencies. A dispersion plot of frequencies versus wavenumbers can be used to determine the range of propagating wavelengths corresponding to an excitation frequency band.

5.3 FE-PML Formulations

We seek the replacement of the plate's infinite, physical domain, Ω_∞, with a combination of a truncated physical domain, Ω and two L_P-thick PMLs, $\Omega_P = \Omega_{P-} \cup \Omega_{P+}$, at $x = \pm L$,

see Figure 5.1. As a result of this replacement, we obtain the computational domain, $\Omega_C = \Omega \cup \Omega_P$, shown in Figure 5.1. In what follows, this computational domain is discretized by 3D finite elements. Steady-state, 3D displacement $\boldsymbol{v} = \{u \;\; v \;\; w\}^T$ within the plate, is governed by the following equilibrium equation [136]:

$$\begin{aligned} \boldsymbol{c}_{xx}\boldsymbol{v}_{,xx} + \boldsymbol{c}_{xy}\boldsymbol{v}_{,xy} + \boldsymbol{c}_{xz}\boldsymbol{v}_{,xz} + \boldsymbol{c}_{xy}^T\boldsymbol{v}_{,yx} + \boldsymbol{c}_{yy}\boldsymbol{v}_{,yy} + \\ \boldsymbol{c}_{yz}\boldsymbol{v}_{,yz} + \boldsymbol{c}_{xz}^T\boldsymbol{v}_{,zx} + \boldsymbol{c}_{yz}^T\boldsymbol{v}_{,zy} + \boldsymbol{c}_{zz}\boldsymbol{v}_{,zz} + \omega^2\boldsymbol{v} = \boldsymbol{0}. \end{aligned} \tag{5.1}$$

Elastic matrices $\boldsymbol{c}_{kl}(k,l=x,y,z)$ are given by, $\boldsymbol{c}_{kl} = \boldsymbol{J}_k^T\boldsymbol{c}\boldsymbol{J}_l$, where

$$\boldsymbol{c} = \begin{bmatrix} c_{11} & c_{12} & c_{13} & 0 & 0 & 0 \\ c_{12} & c_{22} & c_{23} & 0 & 0 & 0 \\ c_{13} & c_{23} & c_{33} & 0 & 0 & 0 \\ 0 & 0 & 0 & c_{44} & 0 & 0 \\ 0 & 0 & 0 & 0 & c_{55} & 0 \\ 0 & 0 & 0 & 0 & 0 & c_{66} \end{bmatrix}, \tag{5.2}$$

$$\boldsymbol{J}_x = \begin{bmatrix} 1 & 0 & 0 \\ 0 & 0 & 0 \\ 0 & 0 & 0 \\ 0 & 0 & 0 \\ 0 & 0 & 1 \\ 0 & 1 & 0 \end{bmatrix}, \boldsymbol{J}_y = \begin{bmatrix} 0 & 0 & 0 \\ 0 & 1 & 0 \\ 0 & 0 & 0 \\ 0 & 0 & 1 \\ 0 & 0 & 0 \\ 1 & 0 & 0 \end{bmatrix}, \boldsymbol{J}_z = \begin{bmatrix} 0 & 0 & 0 \\ 0 & 0 & 0 \\ 0 & 0 & 1 \\ 0 & 1 & 0 \\ 1 & 0 & 0 \\ 0 & 0 & 0 \end{bmatrix}. \tag{5.3}$$

Computational representation of this infinite plate with an FE-PML model requires the replacement of the x-coordinate by a stretched coordinate, $\bar{x}$, defined by Equation (2.19). Thus, frequency-domain equilibrium equation of the FE-PML model can be written as:

$$\begin{aligned}\boldsymbol{c}_{xx}\boldsymbol{v}_{,\bar{x}x}+\boldsymbol{c}_{xy}\boldsymbol{v}_{,\bar{y}y}+\boldsymbol{c}_{xz}\boldsymbol{v}_{,\bar{z}z}+\boldsymbol{c}_{xy}^{T}\boldsymbol{v}_{,y\bar{x}}+\boldsymbol{c}_{yy}\boldsymbol{v}_{,yy}+\boldsymbol{c}_{yz}\boldsymbol{v}_{,yz}+\boldsymbol{c}_{xz}^{T}\boldsymbol{v}_{,z\bar{x}}\\ +\boldsymbol{c}_{yz}^{T}\boldsymbol{v}_{,zy}+\boldsymbol{c}_{zz}\boldsymbol{v}_{,zz}+\omega^{2}\boldsymbol{v}=\boldsymbol{0}.\end{aligned} \tag{5.4}$$

Using the chain rule to expand the first three differential terms on the left hand side of Equation (5.4) followed by substituting $x_{,\bar{x}}$ and $x_{,\bar{x}x}$ from Equations (2.49) and (2.50) results in

$$\begin{aligned}\frac{\boldsymbol{c}_{xx}}{\left[j\omega+d\right]^{2}}\boldsymbol{v}_{,xx}-\frac{d_{,x}\,\boldsymbol{c}_{xx}}{\left[j\omega+d\right]^{3}}\boldsymbol{v}_{,x}+\frac{1}{j\omega\left[j\omega+d\right]}\left[\boldsymbol{c}_{xy}\boldsymbol{v}_{,xy}+\boldsymbol{c}_{xy}^{T}\boldsymbol{v}_{,yx}+\boldsymbol{c}_{xz}\boldsymbol{v}_{,xz}+\boldsymbol{c}_{xz}^{T}\boldsymbol{v}_{,zx}\right]-\\ \left[\boldsymbol{c}_{yz}\boldsymbol{v}_{,yz}+\boldsymbol{c}_{yz}^{T}\boldsymbol{v}_{,yz}+\boldsymbol{c}_{zz}\boldsymbol{v}_{,zz}\right]\frac{1}{\omega^{2}}=\boldsymbol{v}.\end{aligned} \tag{5.5}$$

By splitting displacement wave-field [124], Equation (5.5) can be written as

$$\boldsymbol{v}=\boldsymbol{v}_{1}+\boldsymbol{v}_{2}+\boldsymbol{v}_{3}+\boldsymbol{v}_{4}, \tag{5.6}$$

$$\boldsymbol{c}_{xx}\boldsymbol{v}_{,xx}=\left[j\omega+d\right]^{2}\boldsymbol{v}_{1}, \tag{5.7}$$

$$-d_{,x}\,\boldsymbol{c}_{,xx}\boldsymbol{v}_{,x}=\left[j\omega+d\right]^{3}\boldsymbol{v}_{2}, \tag{5.8}$$

$$\boldsymbol{c}_{xy}\boldsymbol{v}_{,xy}+\boldsymbol{c}_{xy}^{T}\boldsymbol{v}_{,yx}+\boldsymbol{c}_{xz}\boldsymbol{v}_{,xz}+\boldsymbol{c}_{xz}^{T}\boldsymbol{v}_{,zx}=j\omega\left[j\omega+d\right]\boldsymbol{v}_{3}, \tag{5.9}$$

$$\boldsymbol{c}_{yz}\boldsymbol{v}_{,yz}+\boldsymbol{c}_{yz}^{T}\boldsymbol{v}_{,zy}+\boldsymbol{c}_{zz}\boldsymbol{v}_{,zz}=-\omega^{2}\boldsymbol{v}_{4}. \tag{5.10}$$

Inverse Fourier transformation of Equations (5.7) through (5.10) yields the following displacement-based governing equations in the time domain

$$\ddot{\bar{\boldsymbol{v}}}_1 = \boldsymbol{c}_{xx}\boldsymbol{v}_{,xx}, \tag{5.11}$$

$$\ddot{\bar{\boldsymbol{v}}}_5 = -d_{,x}\ \boldsymbol{c}_{xx}\ \boldsymbol{v}_{,x}, \tag{5.12}$$

$$\boldsymbol{v}_5 = \dot{\bar{\boldsymbol{v}}}_2, \tag{5.13}$$

$$\boldsymbol{c}_{xy}\boldsymbol{v}_{,xy} + \boldsymbol{c}_{xy}^T\boldsymbol{v}_{,yx} + \boldsymbol{c}_{xz}\boldsymbol{v}_{,xz} + \boldsymbol{c}_{xz}^T\boldsymbol{v}_{,zx} = \dot{\bar{\boldsymbol{v}}}_3, \tag{5.14}$$

$$\boldsymbol{c}_{yz}\boldsymbol{v}_{,yz} + \boldsymbol{c}_{yz}^T\boldsymbol{v}_{,zy} + \boldsymbol{c}_{zz}\boldsymbol{v}_{,zz} = \ddot{\boldsymbol{v}}_4. \tag{5.15}$$

The FE form of Equations (5.6) and (5.11)-(5.15)

$$\boldsymbol{Q} = \boldsymbol{Q}_1 + \boldsymbol{Q}_2 + \boldsymbol{Q}_3 + \boldsymbol{Q}_4, \tag{5.16}$$

$$\boldsymbol{Q} = \left\{u_1 \quad v_1 \quad w_1 \quad \ldots \quad u_{n_n} \quad v_{n_n} \quad w_{n_n}\right\}, \tag{5.17}$$

$$\boldsymbol{Q}_i = \left\{u_{1(i)} \quad v_{1(i)} \quad w_{1(i)} \quad \ldots \quad u_{n_n(i)} \quad v_{n_n(i)} \quad w_{n_n(i)}\right\};\ i = 1...4, \tag{5.18}$$

$$\boldsymbol{M}\ddot{\bar{\boldsymbol{Q}}}_1 = -\boldsymbol{K}_1\boldsymbol{Q}, \tag{5.19}$$

$$\boldsymbol{M}\ddot{\bar{\boldsymbol{Q}}}_5 = -\boldsymbol{K}_2\boldsymbol{Q}, \tag{5.20}$$

$$\boldsymbol{Q}_5 = \dot{\boldsymbol{Q}}_2, \tag{5.21}$$

$$\boldsymbol{M}\dddot{\tilde{\boldsymbol{q}}}_3 = -\boldsymbol{K}_3\boldsymbol{q}\,, \tag{5.22}$$

$$\boldsymbol{M}\ddot{\boldsymbol{q}}^4 = \boldsymbol{P} - \boldsymbol{K}_4\boldsymbol{q}. \tag{5.23}$$

In Equation (5.17), n_n is the total number of nodes in the FE mesh. Stiffness matrices, $\boldsymbol{K}_i$ (i = 1…*4*), mass matrix, $\boldsymbol{M}$, and consistent load vector, $\boldsymbol{P}$ are obtained by standard FE assembly process of the corresponding element-level matrices as follows:

$$\boldsymbol{K}_1 = \prod_{i=1}^{i=n_e} \boldsymbol{k}_1^{\,i}, \quad \boldsymbol{k}_1^{\,i} = \sum_{l=1}^{n_n^e} \int_{\Omega_e^i} n_{k,x}\boldsymbol{c}'_{xx} n_{l,x}\,dxdydz\,, \tag{5.24}$$

$$\boldsymbol{K}_2 = \prod_{i=1}^{i=n_e} \boldsymbol{k}_2^{\,i}, \quad \boldsymbol{k}_2^{\,i} = \sum_{l=1}^{n_n^e} \int_{\Omega_e^i} n_k d_{,x}\boldsymbol{c}'_{xx} n_{l,x}\,dxdydz\,, \tag{5.25}$$

$$\boldsymbol{K}_3 = \prod_{i=1}^{i=n_e} \boldsymbol{k}_3^{\,i}, \quad \boldsymbol{k}_3^{\,i} = \sum_{l=1}^{n_n^e} \int_{\Omega_e^i} \left[n_{k,x}\boldsymbol{c}'_{xz} n_{l,z} + n_{k,z}\boldsymbol{c}'^{T}_{xz} n_{l,x} \right] dxdydz\,, \tag{5.26}$$

$$\boldsymbol{K}_4 = \prod_{i=1}^{i=n_e} \boldsymbol{k}_4^{\,i}, \quad \boldsymbol{k}_4^{\,i} = \sum_{l=1}^{n_n^e} \int_{\Omega_e^i} n_{k,z}\boldsymbol{c}'_{zz} n_{l,z}\,dxdydz\,, \tag{5.27}$$

$$\boldsymbol{M} = \prod_{i=1}^{i=n_e} \boldsymbol{m}^{\,i}; \quad \boldsymbol{m}^{\,i} = \sum_{l=1}^{n_n^e} \int_{\Omega_e^i} n_k \boldsymbol{I}_3\, n_l\,dxdydz\,, \tag{5.28}$$

$$\boldsymbol{P} = \prod_{i=1}^{i=n_e} \boldsymbol{p}^{\,i}, \quad \boldsymbol{p}^{\,i} = \sum_{l=1}^{n_n^e} \int_{\Omega_e^i} n_k \boldsymbol{I}_3\, p\delta\left(x_p\right) dxdy\,; \quad k = 1,\ldots,n_n^e, \tag{5.29}$$

$$\boldsymbol{c}'_{kl} = \boldsymbol{I}_3\boldsymbol{c}_{kl}\boldsymbol{I}_3\,,\ \boldsymbol{I}_3 = \begin{bmatrix} 1 & 0 & 0 \\ 0 & 1 & 0 \\ 0 & 0 & 1 \end{bmatrix};\ k,l = x,y,z\,. \tag{5.30}$$

Inside Ω_C, standard FE equations corresponding to Equation (5.1) can be integrated using a Newmark explicit scheme. Inside Ω_{P-} and Ω_{P+}, Equations (5.19)-(5.23) can be integrated following the steps given in Equations (4.27)-(4.39). Numerical implementation of the current FE-PML model is discussed next.

5.4 Numerical Implementation and Validation

5.4.1 Numerical Implementation

The current FE-PML model was programmed into FORTRAN 90 computer codes. The codes were compiled and executed on Polaris, a High Performance Computing (HPC) System at the University of Manitoba. Polaris is equipped with 24 1050-MHz Ultra Sparc III CPUs. Analysis of CPU time consumption throughout the code indicated that a matrix-multiplication nested do-loop at each time-integration step accounts for 98% of CPU time consumption. Therefore, the codes were compiled with an automatic parallelization flag allowing for all non-iterative do-loops to be parallelized. This resulted in 80% savings in real run-time compared to one-process execution. Moreover, all symmetric stiffness matrices were stored in a sky-line-symmetric storage mode. This allowed relatively larger problems to be run without exceeding available storage space and some additional savings in CPU time.

Stability of explicit time integration is critically dependent on a time step, Δt. A stable time step is given in terms of element dimensions, Δx, Δy and Δz, and pressure wave speed, c_p, as follows [136]:

$$\Delta t \le \frac{1}{c_p}\left(1/\Delta x^2 + 1/\Delta y^2 + 1/\Delta z^2\right)^{-1/2}. \tag{5.31}$$

Basu [129] has found a stable time step for an FE model to remain stable in an FE-PML model.

Table 5.1 Material properties of nickel in kg/m^3 and GPa

ρ	$\underline{c}_{11}$	$\underline{c}_{12}$	$\underline{c}_{13}$	$\underline{c}_{22}$	$\underline{c}_{23}$	$\underline{c}_{33}$	$\underline{c}_{44}$	$\underline{c}_{55}$	$\underline{c}_{66}$
8.9	298.5	129.5	129.5	298.9	129.5	298.9	84.7	84.7	84.7

5.4.2 Validation of the EMFE Results

The EMFE results are validated against results from the semi-analytical model reported by Mukdadi and Datta [144]. Mukdadi and Datta employed a SAFE method to compute transient responses in layered plates with rectangular cross section. They modeled the plate cross section using 2D nine-node finite elements and modeled the propagation in the infinite dimension with analytical functions. This led to an algebraic eigenvalue problem in the frequency-wavenumber domain whose solution is used to construct 3D elastodynamic Green's functions by modal summation. Transient Green's functions in the time-space domain were evaluated by a double Fourier transform inversion. They also in-

troduced an imaginary part to the frequency in order to circumvent integration difficulty at cutoff frequencies. Here, EMFE results are validated against SAFE results of a finite-width nickel plate with a width-to-height ratio of 2. Density in kg/m^3 and material constants in *GPa* of nickel are given in Table 5.1. Dispersion curves of this plate are computed following the procedure outlined in Section 2.2. Dispersion curves compared to those reported by Mukdadi and Datta [144] are in good agreement as shown in Figure 5.2. The plate is excited by a Gaussian signal whose time history is given by Equation (4.41). In this example, $\sigma_G = 0.8$, $t_0 = 5$, $\omega_c = 3.14$ are chosen. Time history and frequency spectrum of a Gaussian signal corresponding to these values are shown in Figure 5.3.

Green's functions, g_{kl}, denote displacement in k-direction due to a unit line load, p, in the l-direction applied along the y-axis at $(x_l, y_l, z_l) = (0, y, 0.5h)$. From Figure 5.2, a center frequency of 3.14 in the exciting signal corresponds, approximately, to a circular wave number of 0.5π. Using the eight-element rule, a maximum elemental increment (Δx, Δy, or Δz) of 0.1875 should be maintained in each direction. In this example, a constant elemental increment $\Delta x = \Delta y = \Delta z = 0.125$ is used. Using Equation (5.31), time integration step should be less than or equal to 0.045. The current results are obtained with an integration time step of 0.030. Green's functions, g_{kl}, are observed at $(x_k, y_k, z_k) = (10h, 0, 0)$ for extensional, flexural, and torsional modes, are shown in Figs. 4, 5, 6a, and 6b, respec-

tively. Close agreement between the EMFE predictions and the results reported by Mukdadi and Datta [144] is evident.

5.4.3 The Effect of PML Parameters on Accuracy

The empirical damping profile used by Collino and Tsogka [124] is employed in this chapter. This profile can be written as:

$$d(x) = \frac{3c_p}{2L_p} \log\left(\frac{1}{R_p}\right)\left(\frac{x-L}{L_p}\right)^m . \tag{5.32}$$

c_p is the pressure wave speed of plate's material and R_P is a theoretical reflection coefficient from PML after discretization whose value is typically 10^{-3}, which is adopted in this chapter. The RMS errors are evaluated against reference EMFE predictions. In Figures 5.7 and 5.8, the L is replaced by L-x_0, where x_0 is the x-coordinate of the observation point. Both L-x_0 and L are expressed in terms of the number of elements n_0 and n_P in each region, respectively, as follows:

$$n_0 = \frac{L-x_0}{\Delta x}, \quad n_P = \frac{L}{\Delta x}. \tag{5.33}$$

Figure 5.7 illustrates the variation of error, ε_{RMS}, in extensional g_{33} with n_P at different values of n_0. Figure 5.8 shows the variation of error, ε_{RMS}, in extensional g_{33} with n_0 at different values of n_P. These figures indicate that the error, ε_{RMS}, is inversely proportional

to n_P. However, ε_{RMS} is not very sensitive to the change in n_0. It took 467 and 128 minutes of real time to produce the EMFE and FE-PML predictions, respectively, which indicates that the FE-PML has saved 73% of the computational time needed to run an EMFE model. The measured error is utilized to investigate the effect of varying L and L_P while keeping m constant at 2.

5.5 Application Examples

In this section we present two examples of potential applications of the proposed technique in elastic-wave modeling for NDT. In both examples, a rectangular cross-section concrete beam with a width-to-depth ratio of 2 is investigated. Concrete's Poisson's ratio of 0.15 is used. Dispersion plots of the concrete beam for extensional, torsional, and flexural modes are shown in Figure 5.9.

In the first example a concrete beam with a vertical crack halfway through its thickness is considered. The beam is point-loaded at $(x_p, y_p, z_p) = (0, 0, 0.5h)$ and its z-displacement is observed at $(x_0, y_0, z_0) = (1, 0, 0.5h)$. Gaussian load time dependence shown in Figure 5.3 is assumed. Following the same steps outlined in the previous section, a constant elemental increment $\Delta x = \Delta y = \Delta z = 0.125$ integration time step of 0.030 are used in this section. An error analysis detailed in Section 5.4.3 is employed to reach the following PML parameters: $m = 2$, $L = 1$, and $L_P = 3$. However, a snapshot of the z-displacement in the x-z plane at $y = 0$ shows a distinct contrast especially at the crack tip, see Figure 5.11.

Observed z-displacement is shown in Figure 5.10. The effect of vertical crack presence on observed response is not very pronounced. In the second example, a horizontally-cracked (at $z = 0$) concrete beam is considered. The beam has the same geometry and is subject to the same loading-observation arrangement as in the first example. Several horizontal cracks having the same crack length, $L_c = 2$ and different crack widths, W_c, are simulated. Same FE discretization and PML parameters from the first example are reused in this example. Results are shown in Figure 5.12. Obviously, the vertical response is more sensitive to the presence of a horizontal crack more than a vertical crack, see Figure 5.10. Moreover, the vertical response is sensitive to the extent of a horizontal crack across beam's width.

5.6 Conclusions

A combined FE and PML model for the simulation of transient elastic wave propagation and scattering in three dimensions has been presented for the case of an infinite plate with rectangular cross section. A detailed mathematical formulation of the problem featuring a central-difference Newmark's-like time integration scheme is also provided. Numerical implementation of the proposed model involved the use of skyline storage mode of stiff-ness matrices and the exploitation of automatic, loop-level parallelization on an HPC platform. Skyline storage and loop-level parallelization resulted in 80% saving in real

run-time compared to a one-processor execution. Accuracy of the proposed model is validated against a verified EMFE model.

An RMS measure of error resulting from the termination of the FE model with a PML is formulated. According to this measure, the width of a PML has the greatest effect on its accuracy. A slight degradation in accuracy is a justifiable trade-off for a 73% saving in real run-time using FE-PML compared to EMFE. At last, two application examples demonstrate potential use of the proposed model in elastic-wave simulation for NDE of concrete beams.

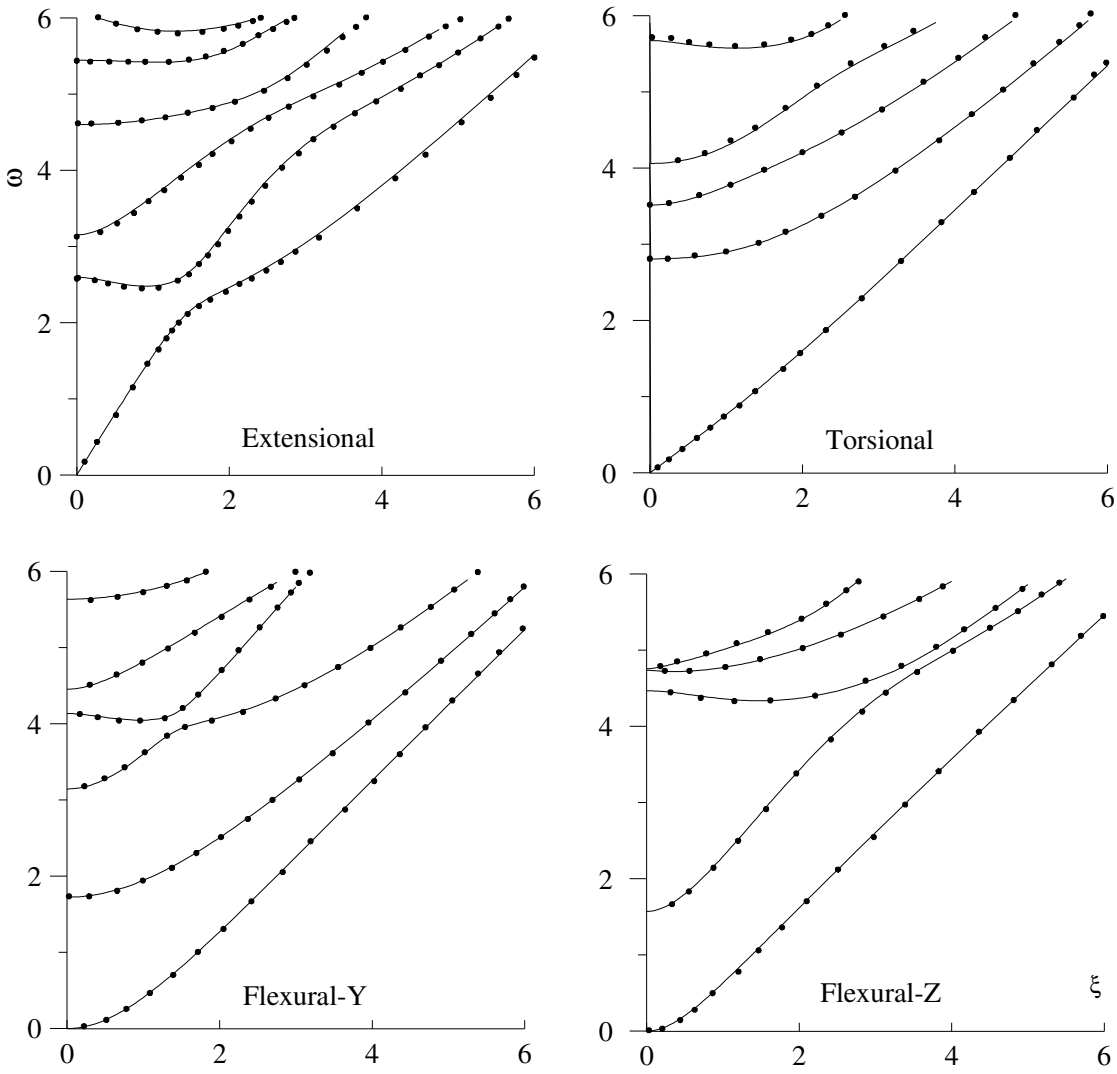

Figure 5.2 Dispersion curves for the finite-width nickel plate with a width-to-height ratio of 2. (____ Computed, • Mukdadi and Datta [144]).

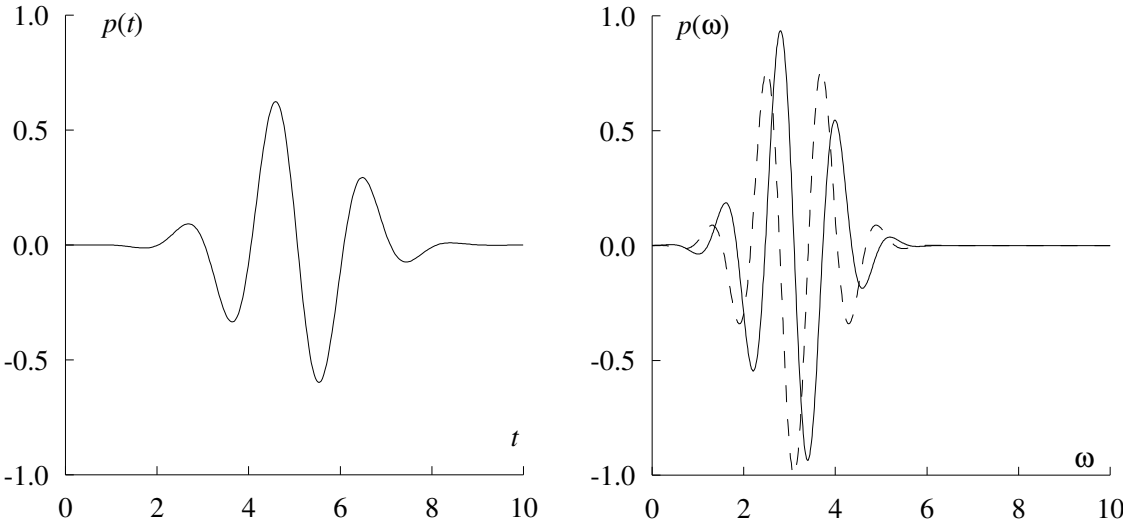

(a) (b)

Figure 5.3 Time history (a) and frequency spectrum (b) (____ Re.; ----- Im.) of the Gaussian excitation

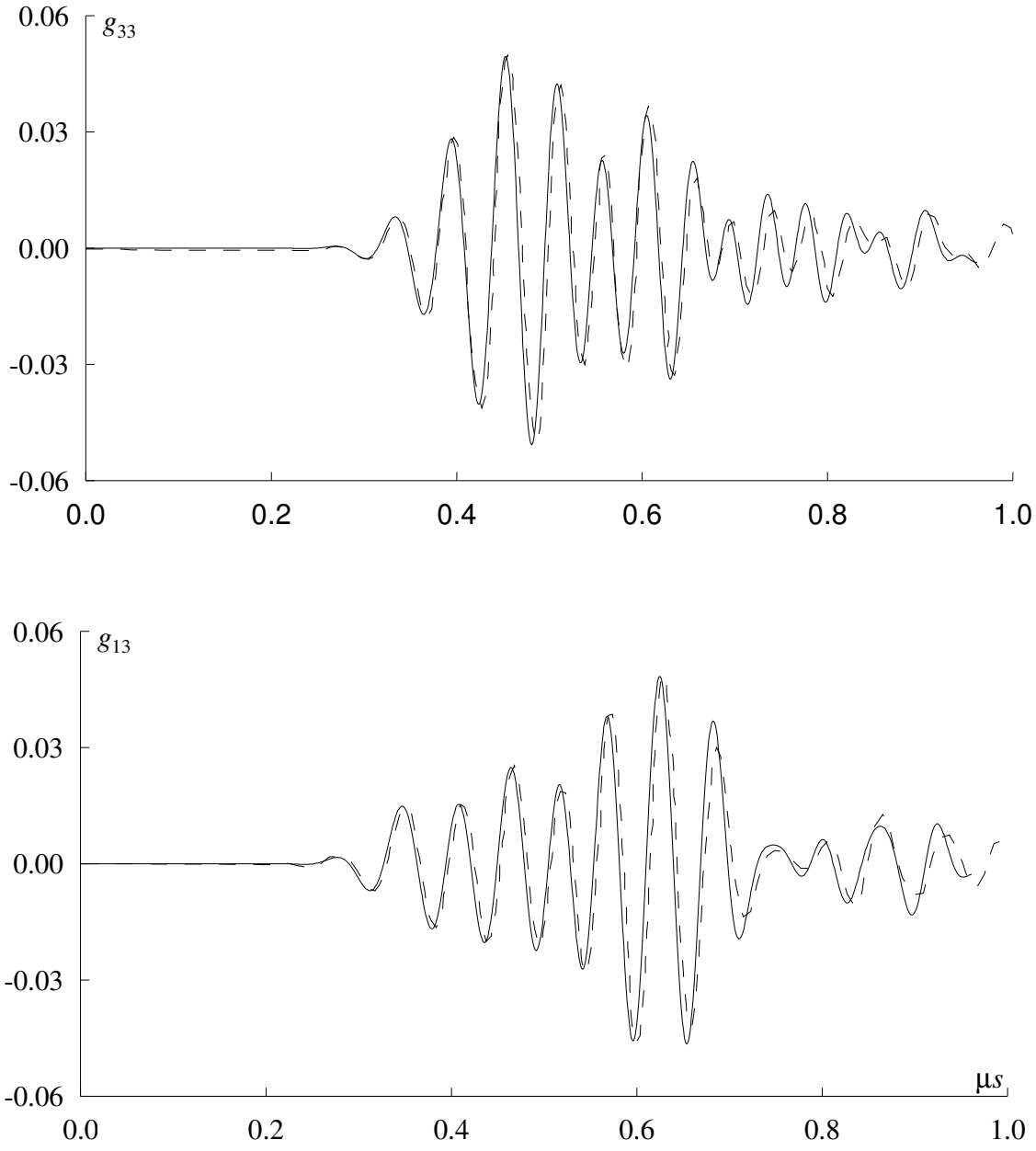

Figure 5.4 Response of extensional mode in a nickel rectangular plate with a width-to-thickness ratio of 2 (____ Mukdadi & Datta [144]; ------ EMFE)

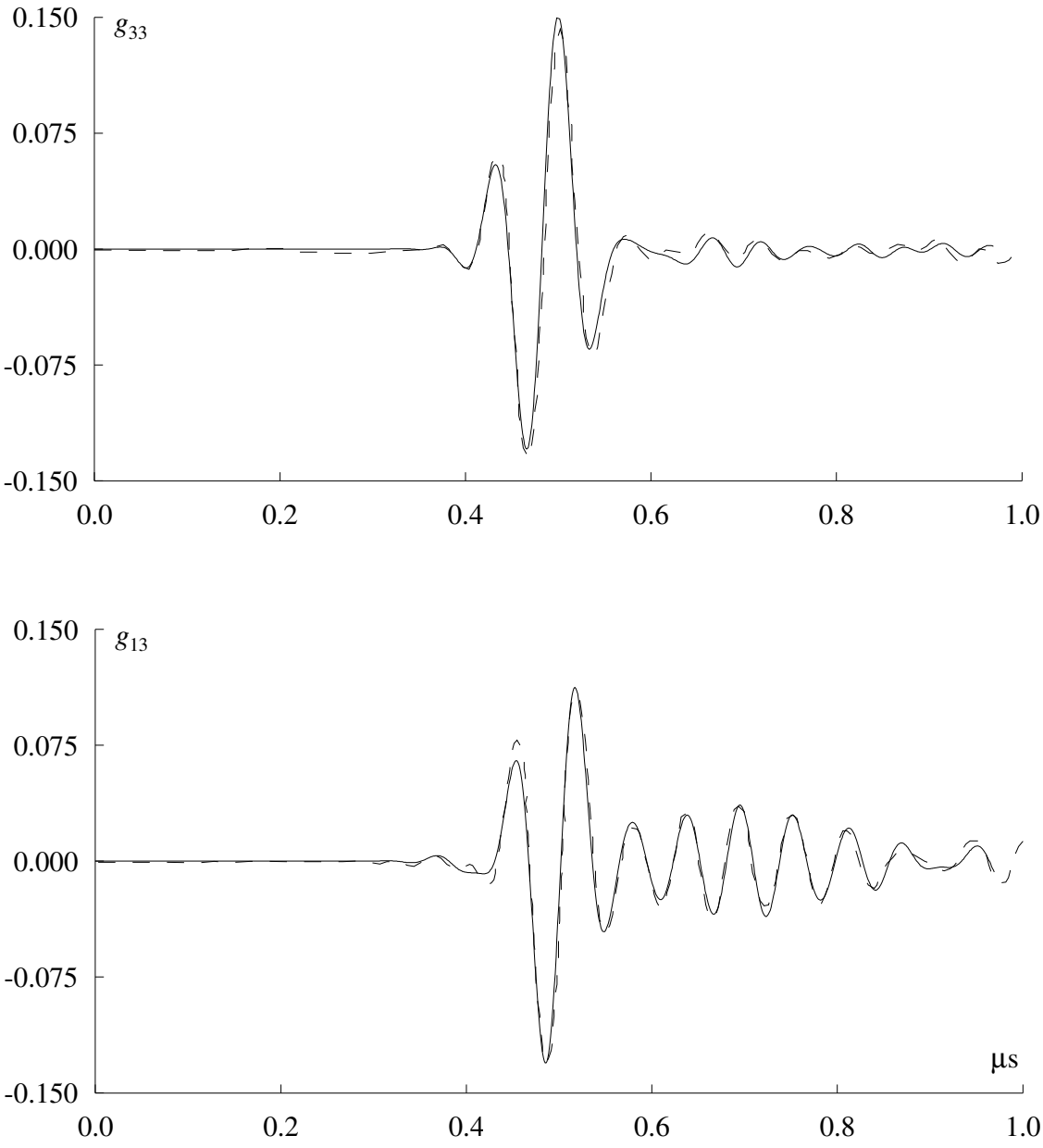

Figure 5.5 Response of flexural mode about y in nickel rectangular plate with a width-to-thickness ratio of 2 (____ Mukdadi & Datta [144]; ------ EMFE)

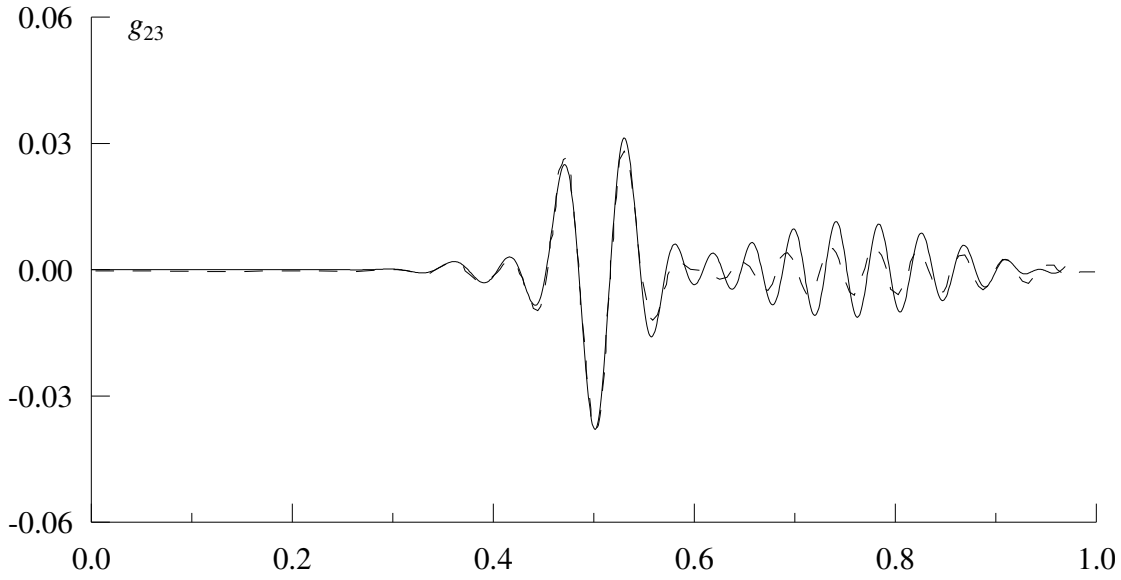

(a)

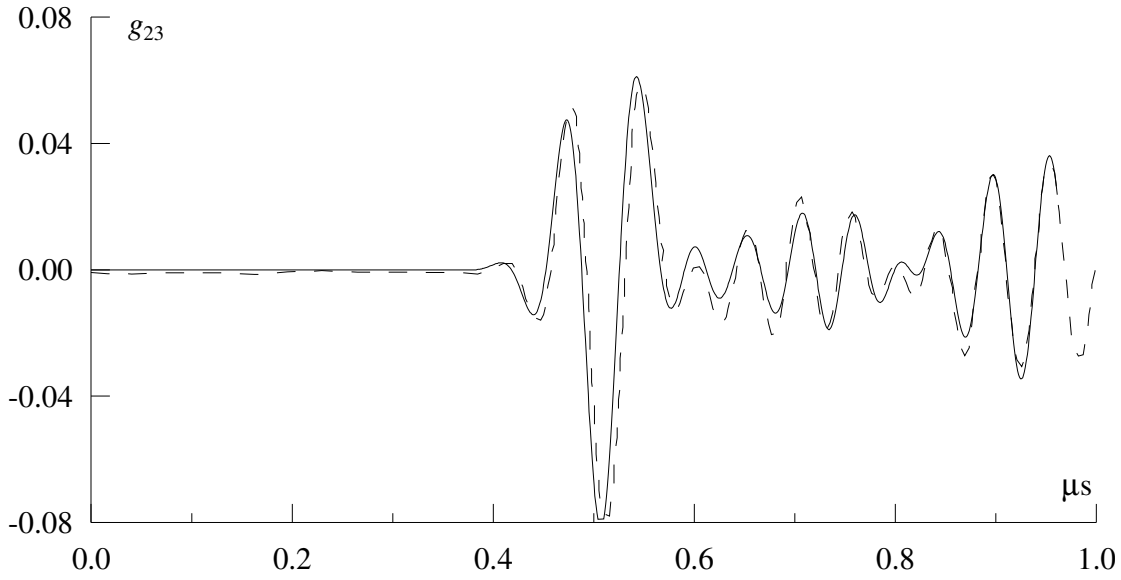

(b)

Figure 5.6 Response of flexural mode about z (a) and torsional mode (b) in nickel rectangular plate with a width-to-depth ratio of 2 (____ Mukdadi & Datta [144]; ------ EMFE)

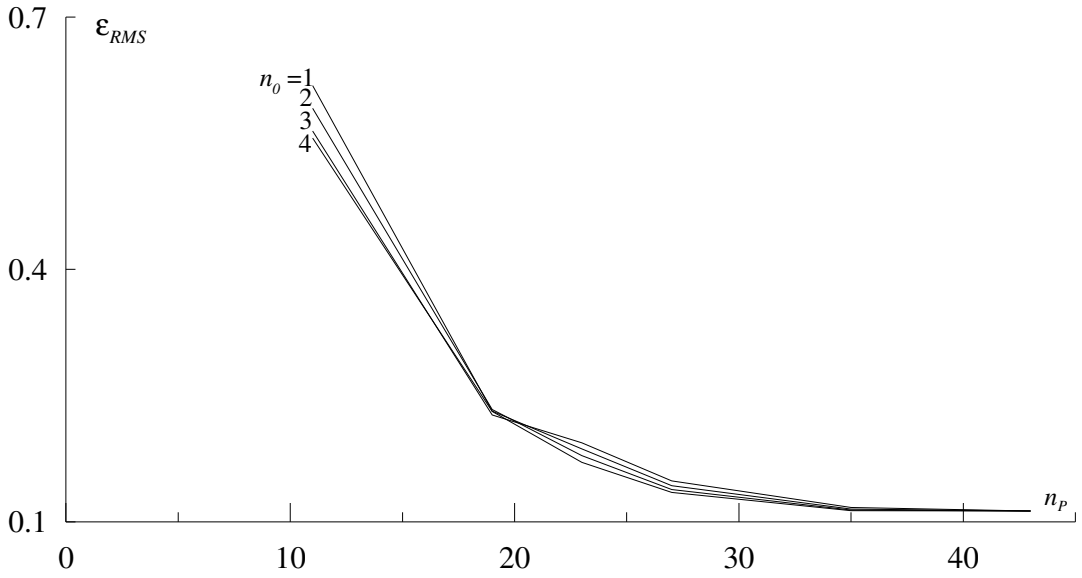

Figure 5.7 Variation of error, ε_{RMS}, with PML thickness, n_P, for several distances, n_0, between PML and observation point.

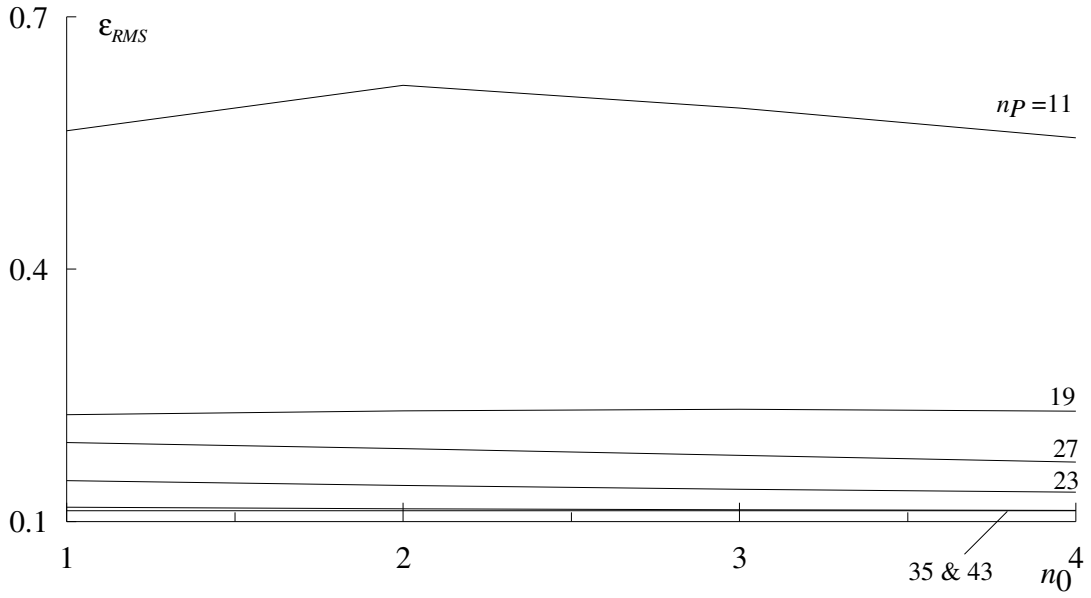

Figure 5.8 Variation of error, ε_{RMS}, with distance, n_0, between PML and observation point for several PML thicknesses, n_P.

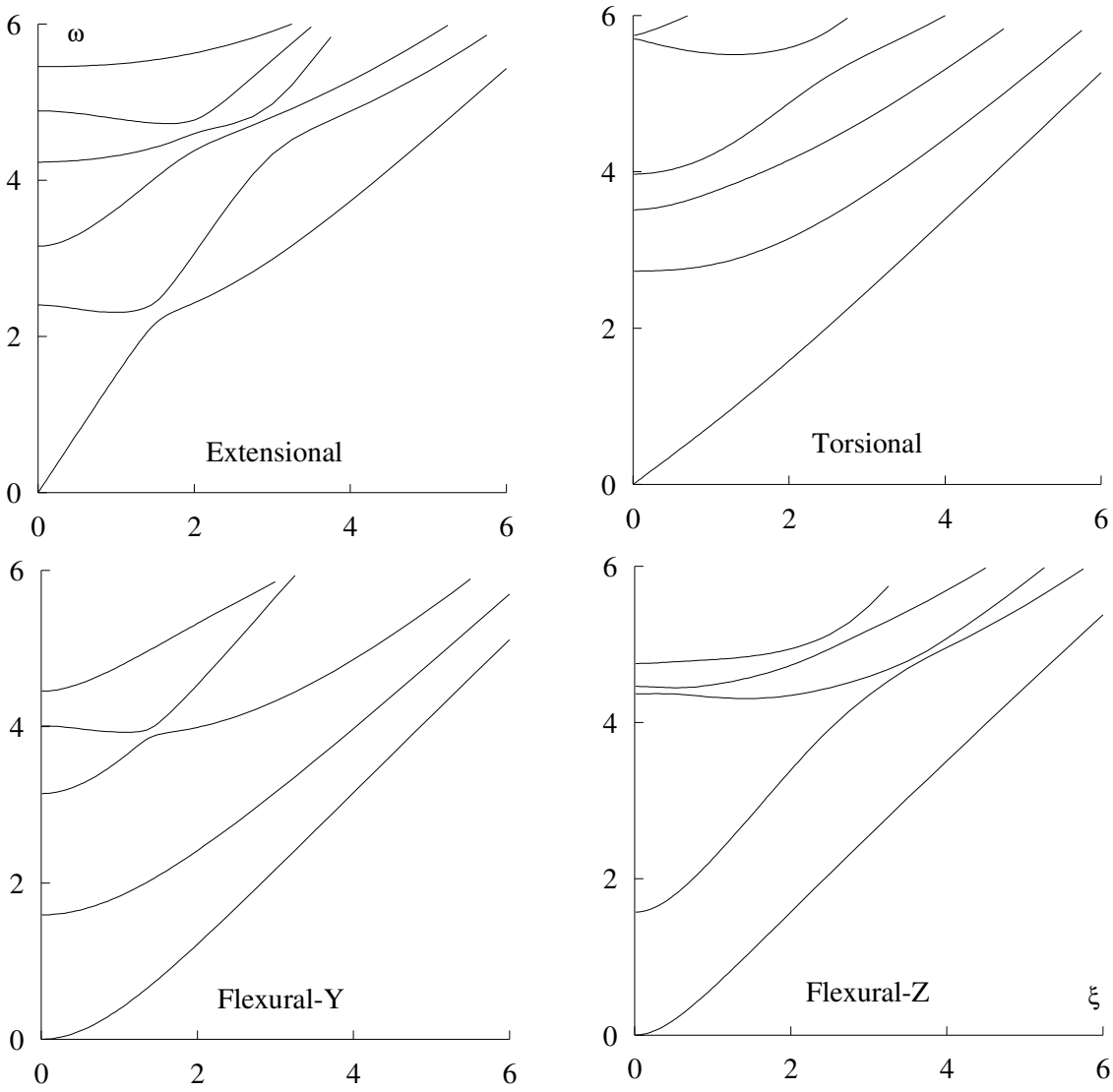

Figure 5.9 Dispersion curves for a flawless concrete beam with width-to-thickness ratio of 2

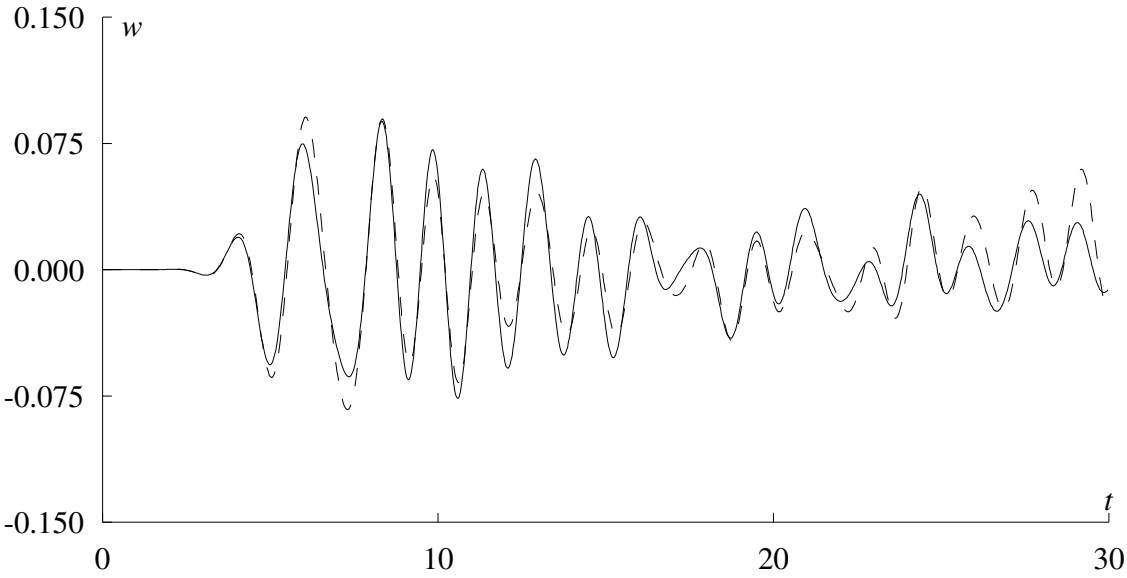

Figure 5.10 Vertical dimensionless response, *w*, of a vertically cracked concrete beam at (1, 0, 0.5) to a vertical point load at (0, 0, 0.5)

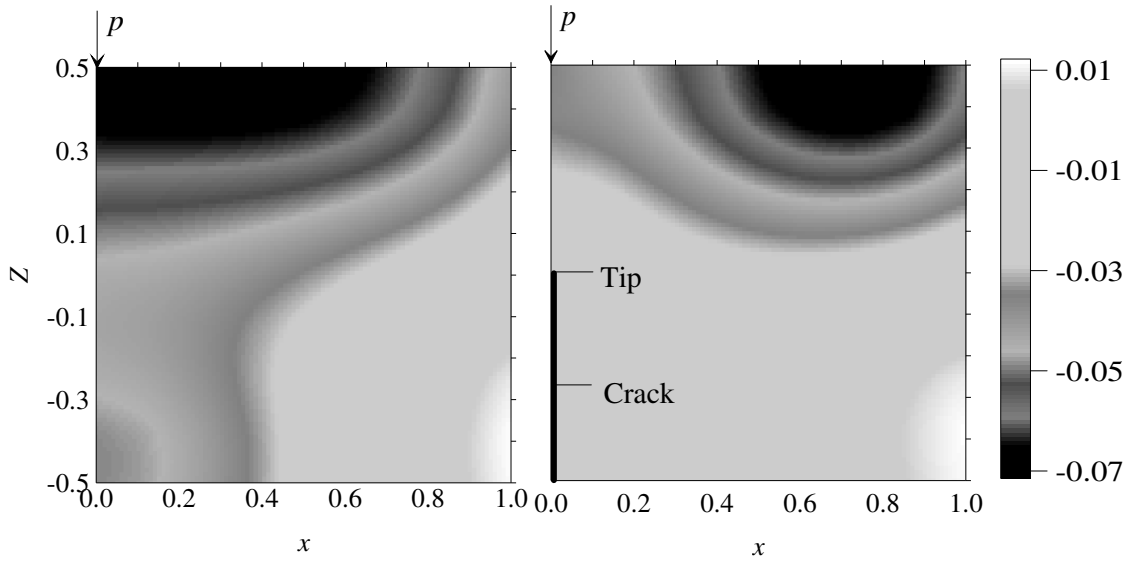

Figure 5.11 A snapshot of vertical dimensionless response, *w*, of a vertically cracked concrete beam (right) versus a flawless beam (left) at $t = 9$.

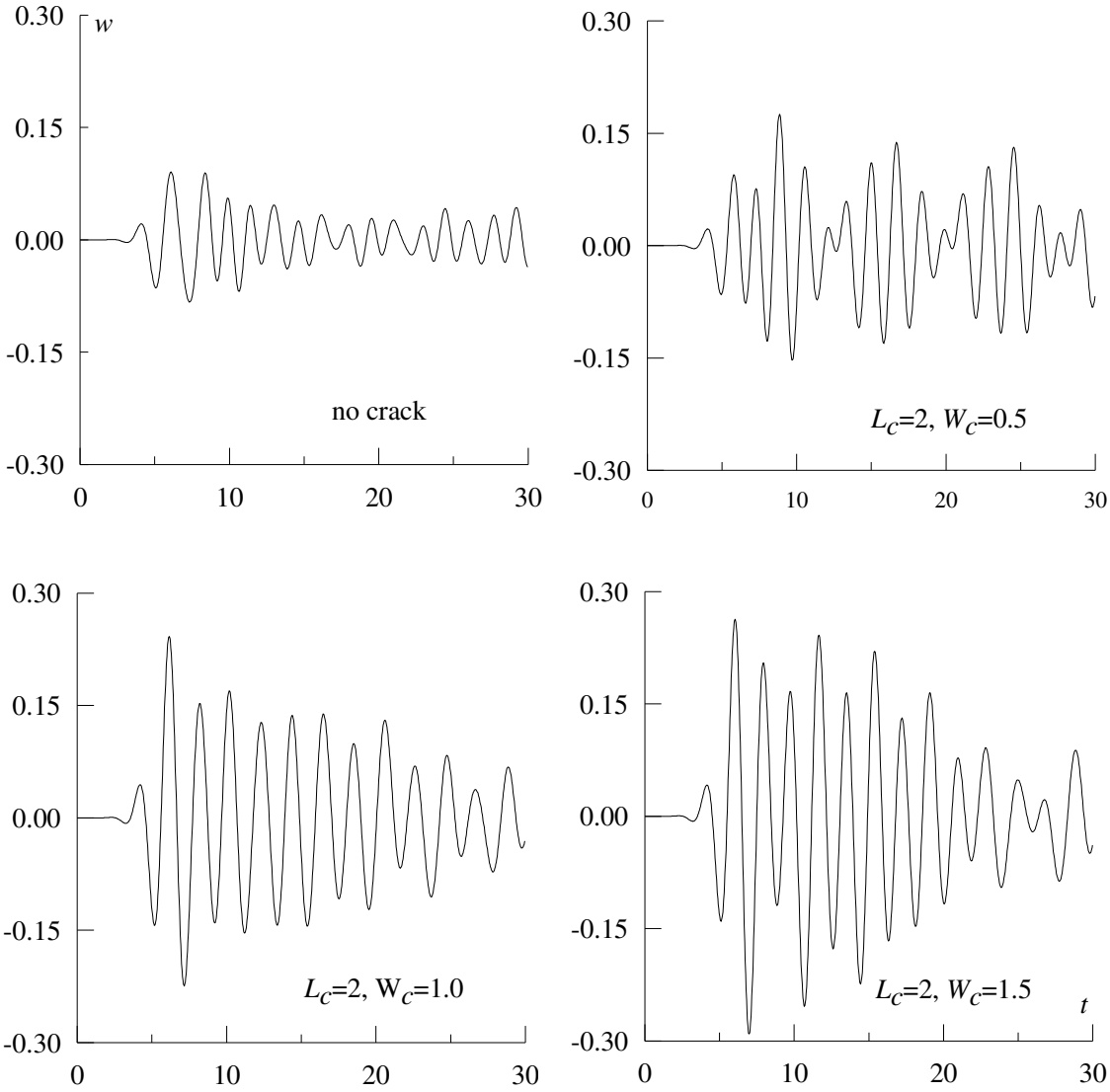

Figure 5.12 Vertical dimensionless response, *w*, of a horizontally cracked concrete beam at (1, 0, 0.5) to a vertical point load at (0, 0, 0.5) for different crack sizes

"Frequently, the difference between success and failure is the resolve to stick to your plan long enough to win" David Cottrell, a contemporary author

Chapter 6

Waves in Infinite Cylinders and Pipes

In this chapter, the formulation of the FE-PML model is extended to the case of circular cylinders and pipes. Three types of wave motion: torsional, axially symmetric, and 3D are considered. Numerical implementation of the formulation is validated through a reciprocity check. Results for the special case of a very thin cylindrical shell are validated against the results for an equivalent (same-thickness) plate obtained from a validated 2D FE-PML models. Several examples of scattering by annular and circumferential cracks in isotropic and transversely isotropic cylindrical shells and thick pipes are presented wherein results are analyzed and discussed.

6.1 Description of the Problem

Figure 6.1 shows a 3D FE-PML model of an infinite hollow circular cylinder with dimensionless inner dimensionless radius, r_i , and dimensionless wall thickness, h. The

cylinder may or may not contain a crack. The load, p, could be a concentrated point load as shown in Figure 6.1 or a uniform circumferential load in the radial or angular direction (not shown).

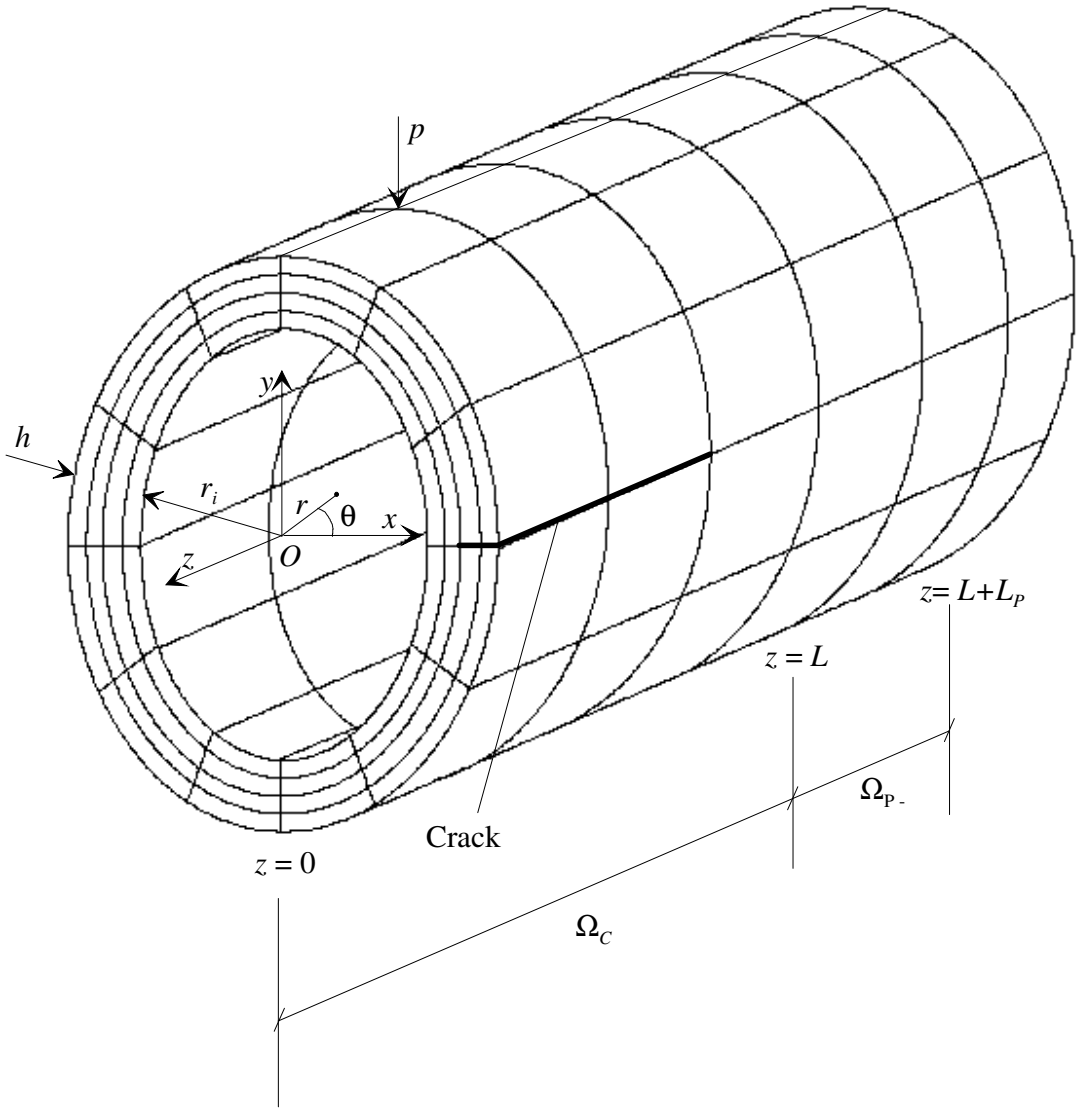

Figure 6.1 An illustration of a combined FE-PML model of an infinite pipe

A domain-of-interest is designated by Ω_C, while the PML domain is given the symbol, Ω_P. The computational domain encompassing Ω_C and Ω_P is modeled by finite elements.

6.2 Governing Equations

Consider the cylindrical coordinate frame $Or\theta z$ shown in Figure 6.1. Strain-displacement relationships at any point (r,θ,z) in the cylinder are given by [136]:

$$\begin{aligned} \boldsymbol{\varepsilon} &= \boldsymbol{J}_0 \frac{\boldsymbol{v}}{r} + \boldsymbol{J}_r \boldsymbol{v}_{,r} + \boldsymbol{J}_\theta \frac{\boldsymbol{v}_{,\theta}}{r} + \boldsymbol{J}_z \boldsymbol{v}_{,z}, \\ \boldsymbol{J}_r &= \boldsymbol{J}_x,\ \boldsymbol{J}_\theta = \boldsymbol{J}_y,\ \boldsymbol{J}_0 = \begin{bmatrix} 0 & 1 & 0 & 0 & 0 & 0 \\ 0 & 0 & 0 & 0 & 0 & -1 \\ 0 & 0 & 0 & 0 & 0 & 0 \end{bmatrix}^T . \end{aligned} \tag{6.1}$$

where $\boldsymbol{J}_x, \boldsymbol{J}_y$, and $\boldsymbol{J}_z$ are given in Equation (5.3); $\boldsymbol{\varepsilon} = \{\varepsilon_{rr} \quad \varepsilon_{\theta\theta} \quad \varepsilon_{zz} \quad \gamma_{\theta z} \quad \gamma_{rz} \quad \gamma_{r\theta}\}^T$ is the vector of strains; and $\boldsymbol{v} = \{u \quad v \quad w\}^T$ is the vector of displacements. Here u, v, and w are the displacement components in the radial, circumferential, and axial directions, respectively. Assuming a transversely isotropic material the constitutive relations between strain, $\boldsymbol{\varepsilon}$, and stress, $\boldsymbol{\sigma} = \{\sigma_{rr} \quad \sigma_{\theta\theta} \quad \sigma_{zz} \quad \sigma_{\theta z} \quad \sigma_{rz} \quad \sigma_{r\theta}\}^T$, can be written in terms of material constants as

$$\boldsymbol{\sigma} = \boldsymbol{\varepsilon c},$$

$$\boldsymbol{c} = \begin{bmatrix} c_{11} & c_{12} & c_{13} & 0 & 0 & 0 \\ c_{12} & c_{22} & c_{23} & 0 & 0 & 0 \\ c_{13} & c_{23} & c_{33} & 0 & 0 & 0 \\ 0 & 0 & 0 & c_{44} & 0 & 0 \\ 0 & 0 & 0 & 0 & c_{55} & 0 \\ 0 & 0 & 0 & 0 & 0 & c_{66} \end{bmatrix}. \tag{6.2}$$

Steady-state equilibrium at any point (r, θ, z) inside the cylinder is governed by the following equations:

$$\boldsymbol{J}_r^T \boldsymbol{\sigma}_{,r} + \frac{\boldsymbol{J}_\theta^T}{r} \boldsymbol{\sigma}_{,\theta} + \boldsymbol{J}_z^T \boldsymbol{\sigma}_{,z} + \frac{(\boldsymbol{J}_x - \boldsymbol{J}_0)^T}{r} \boldsymbol{\sigma} = -\rho \omega^2 \boldsymbol{v}. \tag{6.3}$$

When the geometry of the cylinder and the applied load are both axially symmetric around z the following conditions apply:

$$v = 0, \ \frac{\partial}{\partial \theta} = 0. \tag{6.4}$$

Thus, Equations (6.1) and (6.3) can be reduced, for axisymmetric wave motion, to the following:

$$\boldsymbol{\varepsilon} = \boldsymbol{J}_0' \frac{\boldsymbol{v}}{r} + \boldsymbol{J}_r' \boldsymbol{v}_{,r} + \boldsymbol{J}_z' \boldsymbol{v}_{,z}, \quad \boldsymbol{\varepsilon} = \{\varepsilon_{rr} \quad \varepsilon_{\theta\theta} \quad \varepsilon_{zz} \quad \gamma_{rz}\}^T, \quad \boldsymbol{v} = \{u \quad w\}^T,$$

$$\boldsymbol{J}_0' = \begin{bmatrix} 0 & 0 \\ 1 & 0 \\ 0 & 0 \\ 0 & 0 \end{bmatrix}, \boldsymbol{J}_r' = \begin{bmatrix} 1 & 0 \\ 0 & 0 \\ 0 & 0 \\ 0 & 1 \end{bmatrix}, \boldsymbol{J}_z' = \begin{bmatrix} 0 & 0 \\ 0 & 0 \\ 0 & 1 \\ 1 & 0 \end{bmatrix}, \tag{6.5}$$

$$\boldsymbol{\sigma} = \boldsymbol{c}\,\boldsymbol{\varepsilon},$$
$$\boldsymbol{\sigma} = \{\sigma_{rr} \quad \sigma_{\theta\theta} \quad \sigma_{zz} \quad \sigma_{rz}\}^T, \tag{6.6}$$
$$\boldsymbol{c} = \begin{bmatrix} c_{11} & c_{12} & c_{13} & 0 \\ c_{12} & c_{22} & c_{23} & 0 \\ c_{13} & c_{23} & c_{33} & 0 \\ 0 & 0 & 0 & c_{55} \end{bmatrix},$$

$$\boldsymbol{J}_r'^T \boldsymbol{\sigma}_{,r} + \boldsymbol{J}_z'^T \boldsymbol{\sigma}_{,z} + \frac{(\boldsymbol{J}_r' - \boldsymbol{J}_0')^T}{r}\boldsymbol{\sigma} = -\rho\omega^2 \boldsymbol{v}\,. \tag{6.7}$$

Furthermore, if the geometry of the cylinder is axially symmetric about z while the load is uniformly applied around its circumference in the θ direction, purely torsional waves are generated and the following conditions apply:

$$u = w = 0, \ \frac{\partial}{\partial\theta} = 0. \tag{6.8}$$

Application of the conditions in (6.8) to Equations (6.1) to (6.3) reduces them to the following forms:

$$\gamma_{\theta z} = v_{,z}\,, \ \gamma_{\theta r} = v_{,r} - \frac{v}{r}, \tag{6.9}$$

$$\sigma_{\theta z} = c_{44}\gamma_{\theta z}\,, \ \sigma_{r\theta} = c_{66}\gamma_{\theta r}\,, \tag{6.10}$$

$$\sigma_{r\theta,r} + \frac{2\sigma_{r\theta}}{r} + \sigma_{\theta z,z} = -\rho\omega^2 v\,. \tag{6.11}$$

Formulation of the FE-PML model for 3D, axisymmetric, and torsional wave motion in cylinders is presented next.

6.3 Formulations

6.3.1 3D Waves in Cylinders

Displacement-based equilibrium equation of 3D elastic wave motion in cylindrical coordinates can be obtained by substituting Equation (6.1) into Equation (6.2) and the result into Equation (6.3). Replacing all z-derivatives in the resulting equilibrium equation with $\bar{z}$-derivatives, where $\bar{z}$ is a transformed complex z-coordinate, yield the corresponding equation of equilibrium inside the PML region as follows:

$$\begin{aligned}\boldsymbol{c}_{rr}\boldsymbol{v}_{,rr}+\boldsymbol{c}_{rr}\frac{\boldsymbol{v}_{,r}}{r}-\boldsymbol{c}_{r0}\frac{\boldsymbol{v}}{r}+\boldsymbol{c}_{r\theta}\frac{\boldsymbol{v}_{,r\theta}}{r}+\boldsymbol{c}_{rz}\boldsymbol{v}_{,r\bar{z}}+\boldsymbol{c}_{r\theta}^{T}\frac{\boldsymbol{v}_{,\theta r}}{r}+\boldsymbol{c}_{\theta\theta}\frac{\boldsymbol{v}_{,\theta\theta}}{r^{2}}+\boldsymbol{c}_{\theta 0}\frac{\boldsymbol{v}_{,\theta}}{r^{2}}+\\ \boldsymbol{c}_{\theta z}\frac{\boldsymbol{v}_{,\theta\bar{z}}}{r}+\boldsymbol{c}_{rz}^{T}\boldsymbol{v}_{,\bar{z}r}+\boldsymbol{c}_{\theta z}^{T}\frac{\boldsymbol{v}_{,\bar{z}\theta}}{r}+\boldsymbol{c}_{zz}\boldsymbol{v}_{,\bar{z}\bar{z}}+\boldsymbol{c}_{z0}\frac{\boldsymbol{v}_{,\bar{z}}}{r}=-\omega^{2}\boldsymbol{v}\,.\end{aligned} \tag{6.12}$$

$\boldsymbol{c}_{kl}\ \left(k,l=0,r,\theta,z\right)$ are given by:

$$\boldsymbol{c}_{kl}=\boldsymbol{J}_{k}^{T}\boldsymbol{c}\boldsymbol{J}_{l}\,. \tag{6.13}$$

Expand the $\bar{z}$-derivatives in Equation (6.12) in terms of z-derivatives. Following the procedure by splitting the displacement vector, $\boldsymbol{v}$, and applying inverse Fourier transformation to the resulting equation, will yield the following time-domain split equations:

$$\boldsymbol{v}=\boldsymbol{v}_{1}+\boldsymbol{v}_{2}+\boldsymbol{v}_{3}+\boldsymbol{v}_{4}, \tag{6.14}$$

$$\ddot{\bar{\boldsymbol{v}}}_{1}=\boldsymbol{c}_{zz}\boldsymbol{v}_{,zz}\,, \tag{6.15}$$

$$\ddot{\bar{\boldsymbol{v}}}_{5}=-d_{,z}\,\boldsymbol{c}_{zz}\,\boldsymbol{v}_{,z}, \tag{6.16}$$

$$\boldsymbol{v}_5 = \dot{\bar{\boldsymbol{v}}}_2, \tag{6.17}$$

$$\boldsymbol{c}_{rz}\boldsymbol{v}_{,rz} + \boldsymbol{c}_{\theta z}\frac{\boldsymbol{v}_{,\theta z}}{r} + \boldsymbol{c}_{z0}^T\frac{\boldsymbol{v}_{,z}}{r} + \boldsymbol{c}_{rz}^T\boldsymbol{v}_{,zr} + \boldsymbol{c}_{\theta z}^T\frac{\boldsymbol{v}_{,z\theta}}{r} = \dot{\bar{\boldsymbol{v}}}_3, \tag{6.18}$$

$$\boldsymbol{c}_{rr}\boldsymbol{v}_{,rr} + \boldsymbol{c}_{rr}\frac{\boldsymbol{v}_{,r}}{r} - \boldsymbol{c}_{r0}\frac{\boldsymbol{v}}{r} + \boldsymbol{c}_{r\theta}\frac{\boldsymbol{v}_{,r\theta}}{r} + \boldsymbol{c}_{r\theta}^T\frac{\boldsymbol{v}_{,\theta r}}{r} + \boldsymbol{c}_{\theta\theta}\frac{\boldsymbol{v}_{,\theta\theta}}{r^2} + \boldsymbol{c}_{\theta 0}\frac{\boldsymbol{v}_{,\theta}}{r^2} = \ddot{\boldsymbol{v}}_4. \tag{6.19}$$

The FE form of Equations (6.14)-(6.19) is given by

$$\boldsymbol{Q} = \boldsymbol{Q}_1 + \boldsymbol{Q}_2 + \boldsymbol{Q}_3 + \boldsymbol{Q}_4, \tag{6.20}$$

$$\boldsymbol{Q} = \left\{u_1 \quad v_1 \quad w_1 \quad \ldots \quad u_{n_n} \quad v_{n_n} \quad w_{n_n}\right\}, \tag{6.21}$$

$$\boldsymbol{Q}_i = \left\{u_{1(i)} \quad v_{1(i)} \quad w_{1(i)} \quad \ldots \quad u_{n_n(i)} \quad v_{n_n(i)} \quad w_{n_n(i)}\right\};\ i = 1\ldots4, \tag{6.22}$$

$$\boldsymbol{M}\ddot{\bar{\boldsymbol{Q}}}_1 = -\boldsymbol{K}_1\boldsymbol{Q}, \tag{6.23}$$

$$\boldsymbol{M}\ddot{\bar{\boldsymbol{Q}}}_5 = -\boldsymbol{K}_2\boldsymbol{Q}, \tag{6.24}$$

$$\boldsymbol{Q}_5 = \dot{\boldsymbol{Q}}_2, \tag{6.25}$$

$$\boldsymbol{M}\dot{\bar{\boldsymbol{Q}}}_3 = -\boldsymbol{K}_3\boldsymbol{Q}; \tag{6.26}$$

$$\boldsymbol{M}\ddot{\boldsymbol{Q}}_4 = \boldsymbol{P} - \boldsymbol{K}_4\boldsymbol{Q}. \tag{6.27}$$

In Equation (6.21), n_n is the total number of nodes in the FE mesh. Stiffness matrices, $\boldsymbol{K}_i$ (i = 1…*4*), mass matrix, $\boldsymbol{M}$, and consistent load vector, $\boldsymbol{P}$ are obtained by standard FE assembly process of the corresponding element-level matrices as follows:

$$\boldsymbol{K}_1 = \prod_{i=1}^{i=n_e} \boldsymbol{k}_1^{\,i}, \quad \boldsymbol{k}_1^{\,i} = \sum_{l=1}^{n_n^e} \int_{\Omega_e^i} n_{k,z} \boldsymbol{c}'_{zz} n_{l,z} \, r dr d\theta dz, \tag{6.28}$$

$$\boldsymbol{K}_2 = \prod_{i=1}^{i=n_e} \boldsymbol{k}_2^{\,i}, \quad \boldsymbol{k}_2^{\,i} = \sum_{l=1}^{n_n^e} \int_{\Omega_i^e} n_k d_{,z} \boldsymbol{c}'_{zz} n_{l,z} \, r dr d\theta dz, \tag{6.29}$$

$$\begin{aligned} \boldsymbol{K}_3 = \prod_{i=1}^{i=n_e} \boldsymbol{k}_3^{\,i}, \quad \boldsymbol{k}_3^{\,i} = \sum_{l=1}^{n_n^e} \int_{\Omega_e^i} \Bigg[& n_{k,r} \boldsymbol{c}'_{xz} n_{l,z} + \frac{n_{k,\theta}}{r} \boldsymbol{c}'_{yz} n_{l,z} + n_{k,z} \boldsymbol{c}'_{z0} \frac{n_l}{r} + n_{k,z} \boldsymbol{c}'^{T}_{xz} n_{l,r} + \\ & n_{k,z} \boldsymbol{c}'^{T}_{yz} \frac{n_{l,\theta}}{r} \Bigg] r dr d\theta dz, \end{aligned} \tag{6.30}$$

$$\begin{aligned} \boldsymbol{K}_4 = \prod_{i=1}^{i=n_e} \boldsymbol{k}_4^{\,i}, \quad \boldsymbol{k}_4^{\,i} = \sum_{l=1}^{n_n^e} \int_{\Omega_e^i} \Bigg[& n_{k,r} \boldsymbol{c}'_{x0} \frac{n_l}{r} + n_{k,r} \boldsymbol{c}'_{xx} n_{l,r} + n_{k,r} \boldsymbol{c}'_{xy} \frac{n_{l,\theta}}{r} + \frac{n_{k,\theta}}{r} \boldsymbol{c}'_{y0} \frac{n_l}{r}; \\ & + \frac{n_{k,\theta}}{r} \boldsymbol{c}'^{T}_{xy} n_{l,r} + \frac{n_{k,\theta}}{r} \boldsymbol{c}'_{yy} \frac{n_{l,\theta}}{r} \Bigg] r dr d\theta dz, \end{aligned} \tag{6.31}$$

$$\boldsymbol{M} = \prod_{i=1}^{i=n_e} \boldsymbol{m}^{\,i}, \quad \boldsymbol{m}^{\,i} = \sum_{l=1}^{n_n^e} \int_{\Omega_e^i} n_k \boldsymbol{I}_3 n_l \, r dr d\theta dz, \tag{6.32}$$

$$\boldsymbol{P} = \prod_{i=1}^{i=n_e} \boldsymbol{p}^{\,i}, \quad \boldsymbol{p}^{\,i} = \sum_{l=1}^{n_n^e} \int_{\Omega_e^i} n_k \boldsymbol{I}_3 \, p \delta\left(z_p\right) r dr d\theta; \quad k = 1, \ldots, n_n^e, \tag{6.33}$$

$$\boldsymbol{c}'_{kl} = \boldsymbol{I}_3 \boldsymbol{c}_{kl} \boldsymbol{I}_3, \; \boldsymbol{I}_3 = \begin{bmatrix} 1 & 0 & 0 \\ 0 & 1 & 0 \\ 0 & 0 & 1 \end{bmatrix}; \; k, l = 0, r, \theta, z. \tag{6.34}$$

Inside Ω_C, standard FE equations corresponding to Equation (6.12) can be integrated using a Newmark explicit scheme. Inside Ω_{P-} and Ω_{P+}, Equations (6.28)-(6.33) can be integrated in the steps given in Equations (4.27)-(4.39).

6.3.2 Axisymmetric Waves in Cylinders

Following the same procedure used in the previous section, the FE form of the governing equation describing axisymmetric wave motion inside the PML region of an FE-PML model of a circular cylinder can be summarized as:

$$\boldsymbol{Q} = \boldsymbol{Q}_1 + \boldsymbol{Q}_2 + \boldsymbol{Q}_3 + \boldsymbol{Q}_4, \tag{6.35}$$

$$\boldsymbol{Q} = \left\{ u_1 \quad w_1 \quad \ldots \quad \ldots \quad \ldots \quad u_{n_n} \quad w_{n_n} \right\}, \tag{6.36}$$

$$\boldsymbol{Q}_i = \left\{ u_{1(i)} \quad w_{1(i)} \quad \ldots \quad \ldots \quad \ldots \quad u_{n_n(i)} \quad w_{n_n(i)} \right\};\ i = 1...4, \tag{6.37}$$

$$\boldsymbol{M}\ddot{\boldsymbol{Q}}_1 = -\boldsymbol{K}_1\boldsymbol{Q}, \tag{6.38}$$

$$\boldsymbol{M}\ddot{\boldsymbol{Q}}_5 = -\boldsymbol{K}_2\boldsymbol{Q}, \tag{6.39}$$

$$\boldsymbol{Q}_5 = \dot{\boldsymbol{Q}}_2, \tag{6.40}$$

$$\boldsymbol{M}\dot{\boldsymbol{Q}}_3 = -\boldsymbol{K}_3\boldsymbol{Q}, \tag{6.41}$$

$$\boldsymbol{M}\ddot{\boldsymbol{Q}}_4 = \boldsymbol{P} - \boldsymbol{K}_4\boldsymbol{Q}. \tag{6.42}$$

Stiffness matrices, $\boldsymbol{K}_i$ (i = 1…*4*), mass matrix, $\boldsymbol{M}$, and consistent load vector, $\boldsymbol{P}$ are obtained by standard FE assembly process of the corresponding element-level matrices as follows:

$$\boldsymbol{K}_1 = \prod_{i=1}^{i=n_e} \boldsymbol{k}_1^i, \quad \boldsymbol{k}_1^i = \sum_{l=1}^{n_n^e} \int_{\Omega_e^i} n_{k,z} \boldsymbol{c}'_{zz} n_{l,z} \, r dr dz, \tag{6.43}$$

$$\boldsymbol{K}_2 = \prod_{i=1}^{i=n_e} \boldsymbol{k}_2^i, \quad \boldsymbol{k}_2^i = \sum_{l=1}^{n_n^e} \int_{\Omega_i^e} n_k d_{,z} \boldsymbol{c}'_{zz} n_{l,z} \, r dr dz, \tag{6.44}$$

$$\begin{aligned} \boldsymbol{K}_3 = \prod_{i=1}^{i=n_e} \boldsymbol{k}_3^i, \quad \boldsymbol{k}_3^i = \sum_{l=1}^{n_n^e} \int_{\Omega_e^i} \Big[& n_{k,r} \boldsymbol{c}'_{rz} n_{l,z} + n_{k,z} \boldsymbol{c}'_{z0} \frac{n_l}{r} \\ & + n_{k,z} \boldsymbol{c}'^{T}_{rz} n_{l,r} \Big] r dr dz, \end{aligned} \tag{6.45}$$

$$\boldsymbol{K}_4 = \prod_{i=1}^{i=n_e} \boldsymbol{k}_4^i, \quad \boldsymbol{k}_4^i = \sum_{l=1}^{n_n^e} \int_{\Omega_e^i} \left[n_{k,r} \boldsymbol{c}'_{r0} \frac{n_l}{r} + n_{k,r} \boldsymbol{c}'_{rr} n_{l,r} \right] r dr dz, \tag{6.46}$$

$$\boldsymbol{M} = \prod_{i=1}^{i=n_e} \boldsymbol{m}^i, \quad \boldsymbol{m}^i = \sum_{l=1}^{n_n^e} \int_{\Omega_e^i} n_k \boldsymbol{I}_2 \, n_l \, r dr dz, \tag{6.47}$$

$$\boldsymbol{P} = \prod_{i=1}^{i=n_e} \boldsymbol{p}^i, \quad \boldsymbol{p}^i = \sum_{l=1}^{n_n^e} \int_{\Omega_e^i} n_k \boldsymbol{I}_2 \, p \delta(z_p) r dr; \quad k = 1, \ldots, n_n^e, \tag{6.48}$$

$$\boldsymbol{c}'_{kl} = \boldsymbol{I}_2 \boldsymbol{c}_{kl} \boldsymbol{I}_2, \; \boldsymbol{I}_2 = \begin{bmatrix} 1 & 0 \\ 0 & 1 \end{bmatrix}; \; k, l = 0, r, z. \tag{6.49}$$

6.3.3 Torsional Waves in Cylinders

For torsional waves in cylinders, the FE forms of the governing equations inside the PML region after splitting are:

$$\boldsymbol{Q} = \boldsymbol{Q}_1 + \boldsymbol{Q}_2 + \boldsymbol{Q}_3, \tag{6.50}$$

$$\boldsymbol{Q} = \left\{ v_1 \quad v_2 \quad \ldots \quad \ldots \quad \ldots \quad v_{n_n - 1} \quad v_{n_n} \right\}, \tag{6.51}$$

$$\boldsymbol{Q}_i = \left\{ v_{1(i)} \quad v_{2(i)} \quad \ldots \quad \ldots \quad \ldots \quad v_{n_n - 1(i)} \quad v_{n_n(i)} \right\}; \; i = 1 \ldots 3, \tag{6.52}$$

$$\boldsymbol{M}\ddot{\boldsymbol{Q}}_1 = -\boldsymbol{K}_1\boldsymbol{Q}, \tag{6.53}$$

$$\boldsymbol{M}\ddot{\boldsymbol{Q}}_4 = -\boldsymbol{K}_2\boldsymbol{Q}, \tag{6.54}$$

$$\boldsymbol{Q}_4 = \dot{\boldsymbol{Q}}_2, \tag{6.55}$$

$$\boldsymbol{M}\ddot{\boldsymbol{Q}}_3 = \boldsymbol{P} - \boldsymbol{K}_3\boldsymbol{Q}_3. \tag{6.56}$$

Stiffness matrices, $\boldsymbol{K}_i$ (i = 1…*3*), mass matrix, $\boldsymbol{M}$, and consistent load vector, $\boldsymbol{P}$ are obtained by standard FE assembly process of the corresponding element-level matrices as follows:

$$\boldsymbol{K}_1 = \prod_{i=1}^{i=n_e} \boldsymbol{k}_1^{\,i}, \quad \boldsymbol{k}_1^{\,i} = \sum_{l=1}^{n_n^e} \int_{\Omega_e^i} n_{k,z}\boldsymbol{c}_{44} n_{l,z}\, r dr dz, \tag{6.57}$$

$$\boldsymbol{K}_2 = \prod_{i=1}^{i=n_e} \boldsymbol{k}_2^{\,i}, \quad \boldsymbol{k}_2^{\,i} = \sum_{l=1}^{n_n^e} \int_{\Omega_e^i} n_k d_{,z}\boldsymbol{c}_{44} n_{l,z}\, r dr dz, \tag{6.58}$$

$$\begin{aligned}\boldsymbol{K}_3 = \prod_{i=1}^{i=n_e} \boldsymbol{k}_3^{\,i}, \quad \boldsymbol{k}_3^{\,i} = \sum_{l=1}^{n_n^e} \int_{\Omega_e^i} \Bigg[& \frac{n_k}{r}\boldsymbol{c}_{66}\frac{n_l}{r} + n_{k,r}\boldsymbol{c}_{66} n_{l,r} \\ & - \frac{n_k}{r}\boldsymbol{c}_{66} n_{l,r} - n_{k,r}\boldsymbol{c}_{66}\frac{n_l}{r} \Bigg] r dr dz,\end{aligned} \tag{6.59}$$

$$\boldsymbol{M} = \prod_{i=1}^{i=n_e} \boldsymbol{m}^{\,i}, \quad \boldsymbol{m}^{\,i} = \sum_{l=1}^{n_n^e} \int_{\Omega_e^i} n_k n_l\, r dr dz, \tag{6.60}$$

$$\boldsymbol{P} = \prod_{i=1}^{i=n_e} \boldsymbol{p}^{\,i}, \quad \boldsymbol{p}^{\,i} = \sum_{l=1}^{n_n^e} \int_{\Omega_e^i} n_k\; p\,\delta\left(z_p\right) r dr; \quad k = 1,\ldots,n_n^e. \tag{6.61}$$

Numerical implementation of the FE-PML formulations presented in this section is discussed next.

6.4 Model Implementation and Validation

The FE-PML models formulated in Section 6.3 have been programmed in Fortran 90. In order to validate the program an isotropic cylindrical shell with Poisson's ration of 1/3 and an inner-radius-to-thickness ratio, r_i/h, of 100 has been considered. Results are anticipated to compare very closely to those obtained for a plate of the same material and thickness due to the high r_i/h ratio. Two comparisons are made. In the first comparison, response time history of tangential displacement, v, due to a tangential line load uniformly distributed around the outer circumference of the shell is compared to response time history of anti-plane displacement in the plate excited by an anti-plane line load [145]. In the second comparison, radial displacement, u, due to a radial line load is compared to vertical displacement in a plate excited by a vertical line load [146]. In both comparisons, time history response of the shell is predicted by both 2D and 3D models. Figure 6.2 shows time history of tangential displacement in the thin shell at z = 5 due to a tangential line load applied at z = -5. Load time history is given in Figure 3.2a. Both 2D and 3D time-history predictions in the thin shell compare closely, as expected, to response time history of anti-plane displacement in the plate. Figure 6.3 shows time history of radial displacement at z = 5 due to a radial line load at z = -5. Load time dependence is represented by Equation (4.41). The radial displacement in thin shell due to a radial line load is in very good agreement with vertical displacement time history in the plate due to a vertical line load.

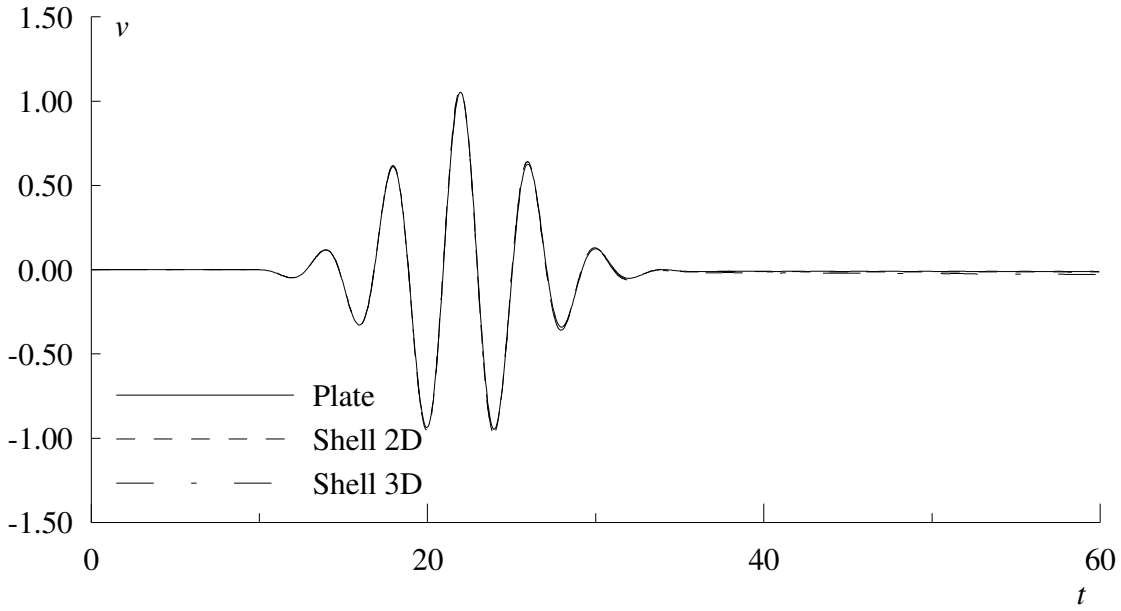

Figure 6.2 Tangential (anti-plane) displacement time histories in the shell (plate)

6.5 Results and Discussion

In this section numerical results are given for an isotropic pipe and a transversely isotropic cylindrical shell. The pipe material has a modulus of elasticity, $\underline{E}$, and Poisson's ration, ν, of $210\ GPa$ and 0.29, respectively. The longitudinal and torsional (shear) wave speeds are calculated to be $\underline{c_p} = 32.6\times10^3$ and $\underline{c_s} = 5.96\times10^3$. The inner radius and wall thickness of the cylinder are $\underline{r_i} = 38$ and $\underline{h} = 5.5\ mm$, respectively.

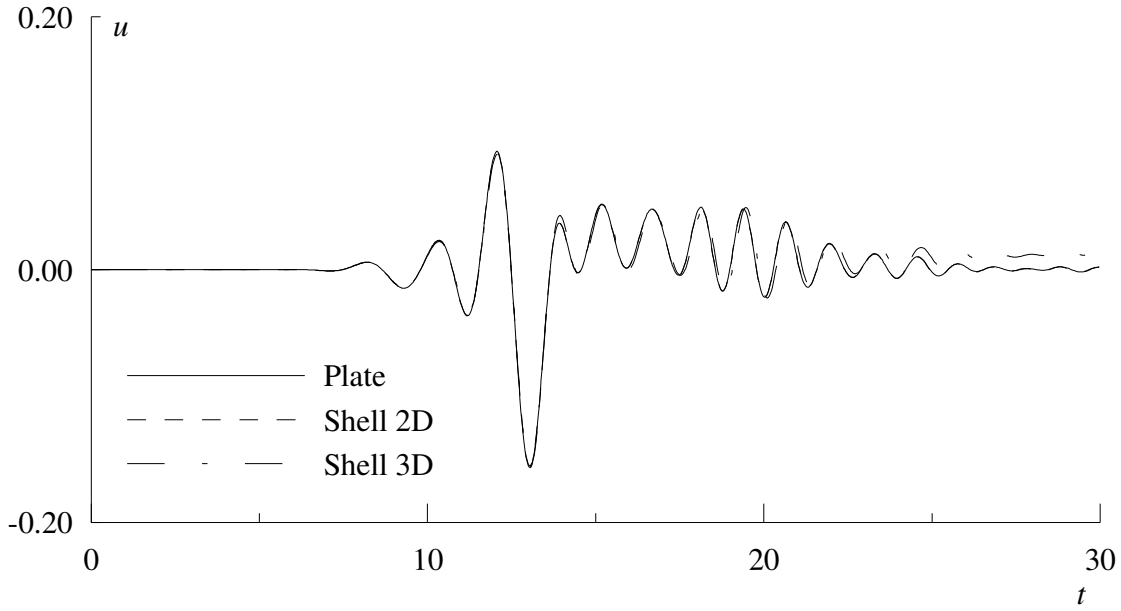

Figure 6.3 Radial (vertical) displacement time histories in the shell (plate)

The cylindrical shell has r_i/h ratio of 20. The cylindrical shell's composite material is a $[G90/G0]_S$ glass/epoxy. The letter "G" represents the glass/epoxy composite. The following number indicates the azimuthal angle of the fibre orientation with respect to the z-axis. The subscript "S" denotes that glass/epoxy layers are stacked symmetrically around the middle surface of the shell. Properties of glass epoxy are taken from Liu et al. [32]; they are listed in Table 6.1 for convenience.

Table 6.1 Material properties of glass/epoxy composite in *GPa* and g/cm^3

Property	$\underline{E}_1$	$\underline{E}_2$	$\underline{G}_{12}$	$\underline{\nu}_{12}$	$\underline{\nu}_{23}$	$\underline{\rho}$
Value	38.49	9.367	3.414	0.291	0.507	2.66

Three numerical examples are presented in this section. In all numerical examples, a Gaussian load time dependence in the form of Equation (4.41) is assumed. The following parameters used in Equation (4.34) $\sigma_G = 1.2$, $t_0 = 5$, $\omega_{\bar{c}} = 3.14$ are chosen. A Gaussian signal that corresponds to these values is the same as shown in Figure 5.3.

6.5.1 Simulating PE Detection of Welds and Welding Defects

This section presents an example application of using the proposed FE-PML model in simulating pulse-echo (P-E) detection of welds and welding defects in a steel pipe. The steel pipe, in this example, is welded with an orthotropic weldment. Mechanical properties of the weld orthotropic material are taken from Rattanawangcharoen et al. [80] and summarized in Table 6.2. A schematic illustration of the welded pipe with an ideal weldment is shown in Figure 6.4a. Two defected welds are shown in Figure 6.4b: a weld with an incomplete penetration or what is called root defect and a weld containing trapped gas pores. The latter defect is assumed, here, to cause percentage degradation in elastic constants and mass density of welding filler.

Table 6.2 Material properties of glass/epoxy composite in *GPa* and g/cm^3

Property	$\underline{c}_{11}$	$\underline{c}_{13}$	$\underline{c}_{33}$	$\underline{c}_{55}$	$\underline{c}_{66}$	$\underline{\rho}$
Value	229	160	262	82	81	7.8

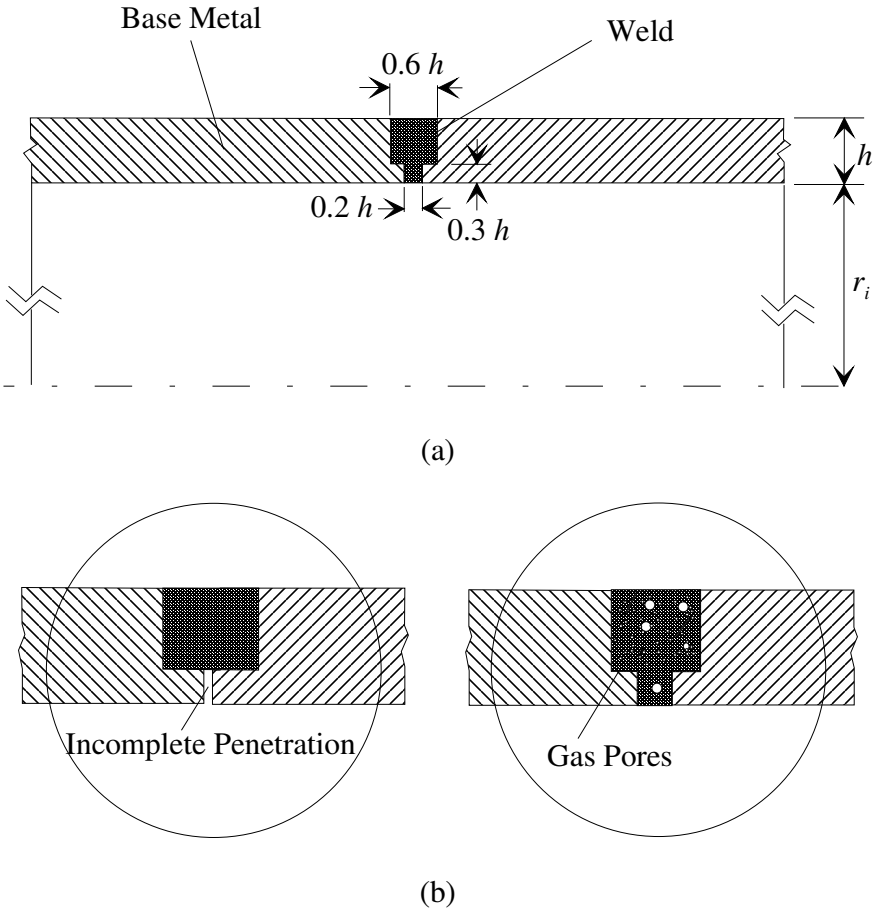

Figure 6.4 Schematics of a steel pipe with (a) ideal weld and (b) weld defects

The radial line load was applied uniformly to the outer surface of the pipe at z = -6. Outer surface displacements are observed at z =-5.5. The problem is modeled by an axisymmetric FE-PML model. The damping profile in Equation (5.32) is used along with the following parameters: L = 6.1; L_p = 1.9 and m = 2. Square, linear quadrilateral elements having a (dimensionless) size of 0.1 are used to idealize the problem based on convergence study.

The effect of introducing an inhomogeneity to the pipe is investigated by predicting radial and axial displacements for the seamless and ideally-welded case. The weld demonstrates its presence very clearly in the time history response of radial displacement shown in Figure 6.5. Next, the effects of the two types of welding defects shown in Figure 6.4 on radial displacement time history are investigated. Incomplete penetration of welding filler usually occurs when the gap between the two welded pipes is small. Here, four incomplete penetration gap sizes: 0.02 h, 0.04 h, 0.06 h, and 0.08 h are considered.

Figure 6.6 shows very clearly the reflections arriving from the gaps getting larger and larger as the gap width increases. Finally, the effect of gas pores presence inside the weld and the related weld material degradation is studied next.

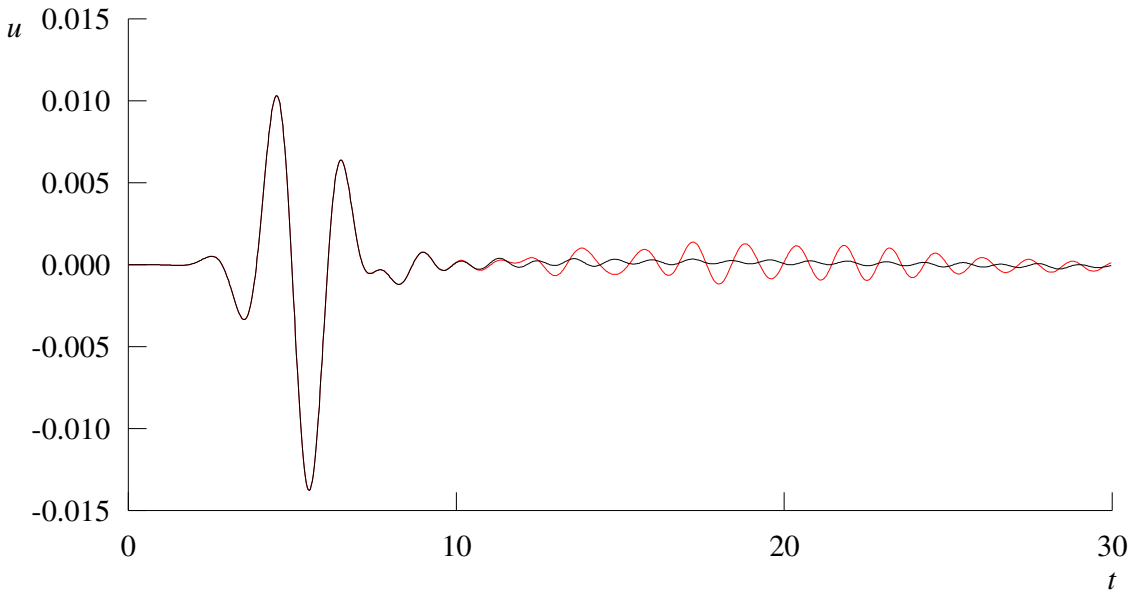

Figure 6.5 A comparison of radial displacements in a seamless (black) and a welded (red) steel pipe. Reflection from weld is obvious.

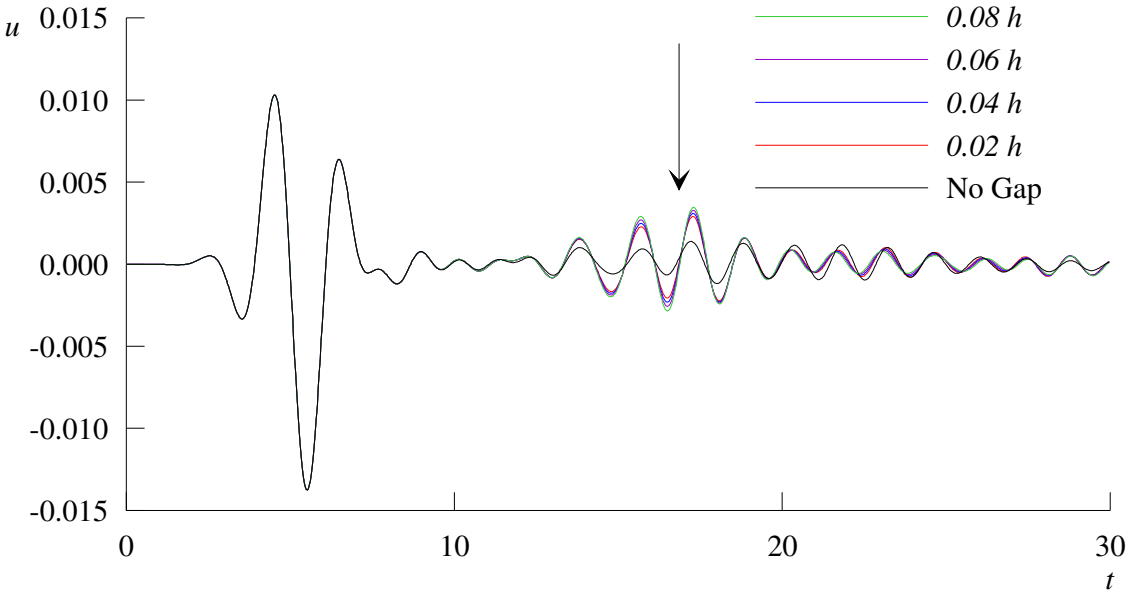

Figure 6.6 A comparison of radial displacements in weld with different incomplete penetration gaps. A reflection from the gap is getting larger as the gap width increases.

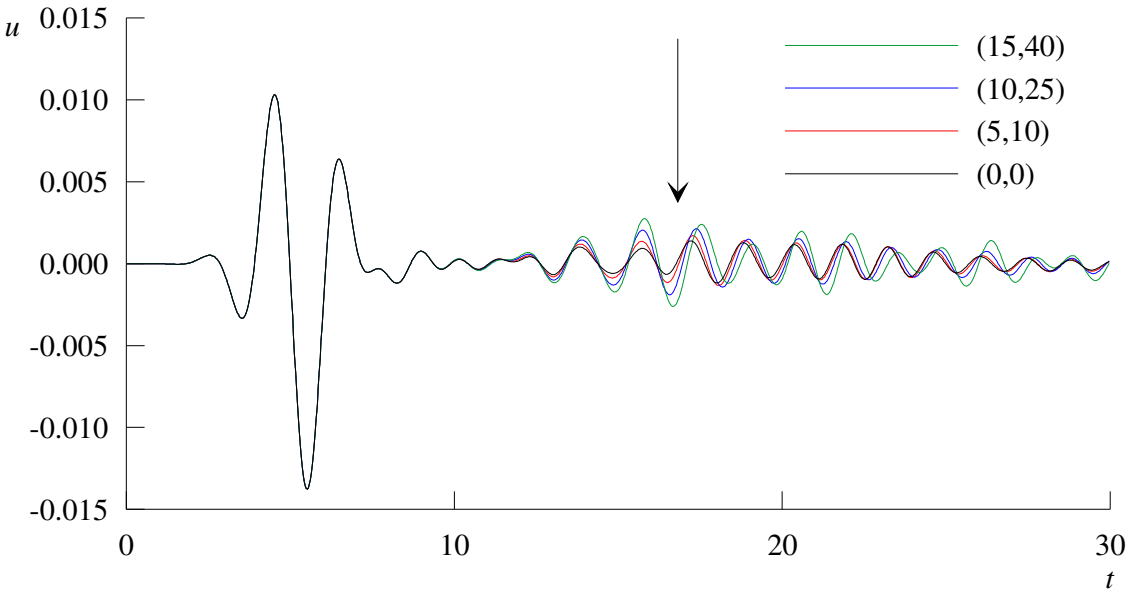

Figure 6.7 Reflection form welds flawed with different levels of material degradation due to gas pores. See Table 6.3 for notation.

Table 6.3 Representation of weld material degradation due to gas pores

Notation	Percentage Degradation	
	Mass Density	Elastic Constants
(0,0)	0	0
(5,10)	5	10
(10,25)	10	25
(15,40)	15	40

Table 6.3 explains the notation used to denote percentage degradation in mass density and elastic constants due to the presence of gas pores in a weld. Figure 6.7 shows reflections from various gas-pore degraded welds. The size of the echo is very sensitive to the level of gas-pore degradation.

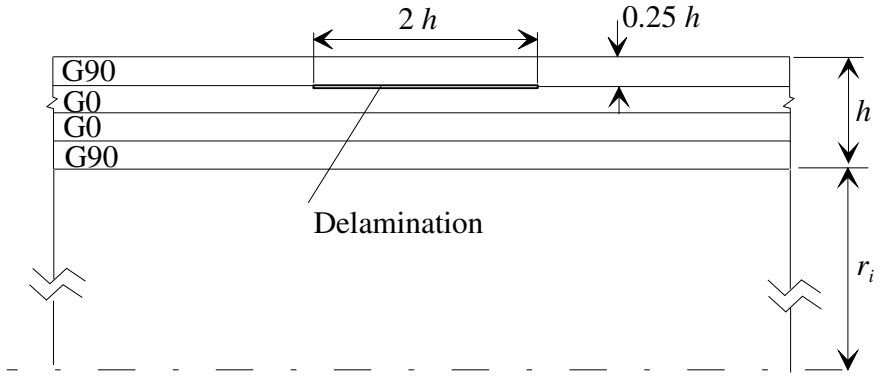

Figure 6.8 A schematic of a glass/epoxy cylindrical shell with delamination

A P-E technique is suitable for a structure that is accessible only from one side. In the following section a composite cylindrical shell that is accessible from both sides is simulated during a pitch-catch (P-C) inspection.

6.5.2 Simulating P-C Identification of a Delamination Defect

In this example, the effect of delamination on the dynamic response of a delaminated glass/epoxy cylindrical shell to a radial line load is investigated. A schematic of the delamination geometry is depicted in Figure 6.8.

The load is uniformly distributed around the circumference of the shell at z = -2 and -1 while radial displacements are observed on the opposite inner surface of the shell at z = -2 and -1, respectively. Figure 6.9 demonstrates a clear contrast between observed radial displacements in a flawless versus a delaminated shell. Figure 6.9 shows the distinct reflection from the delamination's edge observed at z = -2 grows stronger and closer to through-thickness transmission as the P-C points are drawn nearer to the delamination at z = -1. When the delamination lies across the P-C points, one should expect a delay in the received signal as it gets around the delamination. Such an expectation is confirmed by placing the P-C points at z = 0; radial displacement time history is shown in Figure 6.10. Transforming response time histories to frequency spectra through an inverse Fourier transformation can be a very useful means to identifying and locating delamination.

6.5.3 Simulating Corrosion Identification in Steel Pipes

Non-destructive identification of inaccessible corroded surfaces is a challenging task motivated by several practical applications. One of the primary drivers is inner-surface corrosion of steel pipelines in the oil and gas industry.

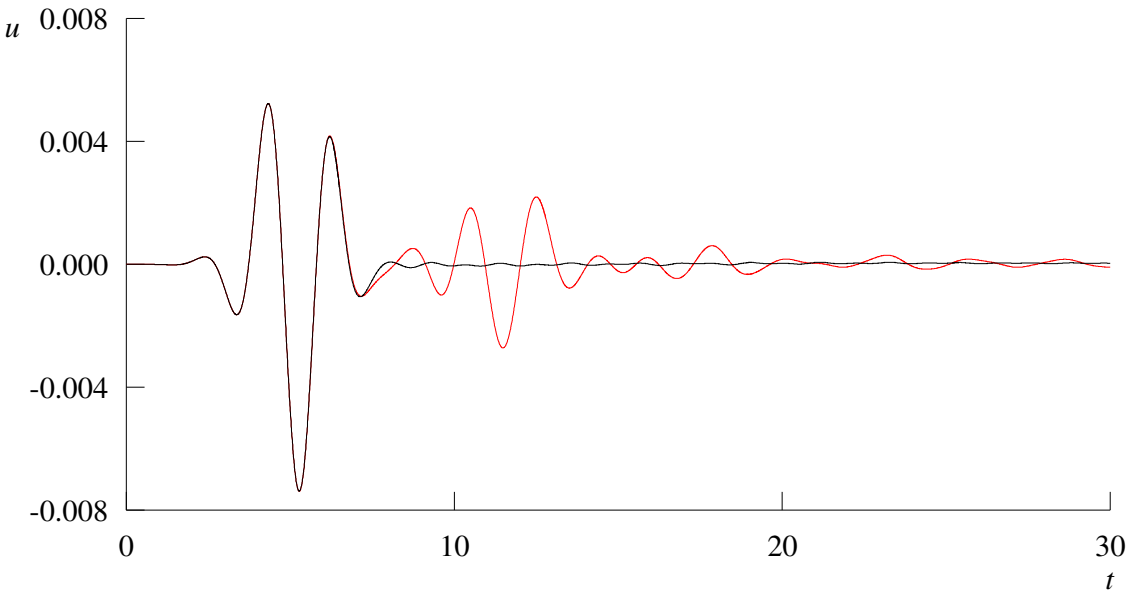

(a)

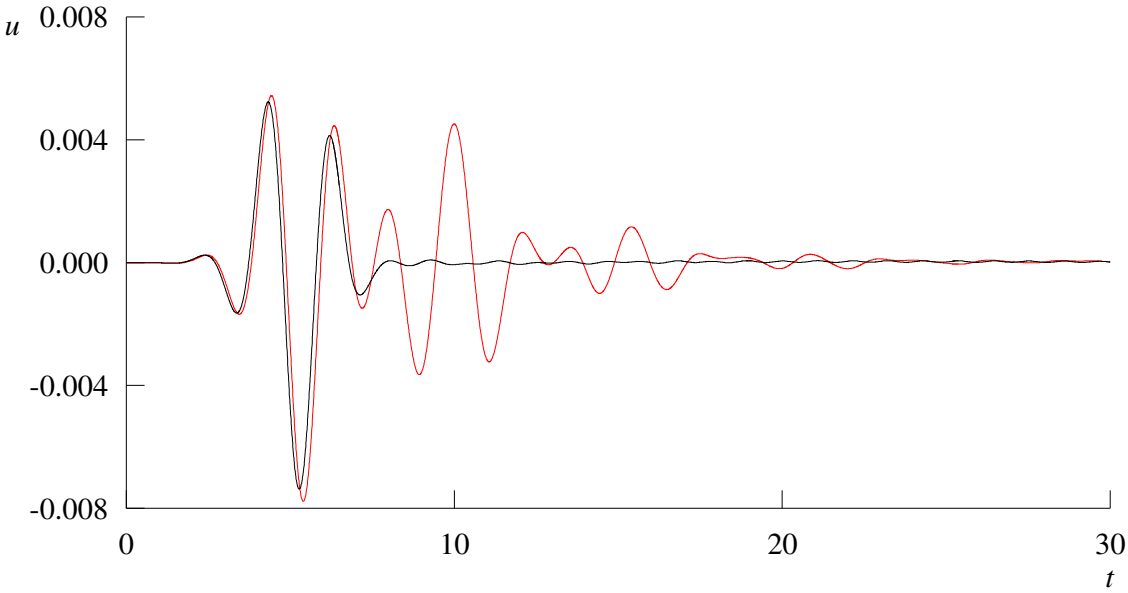

(b)

Figure 6.9 Radial time history responses observed in a pitch-catch arrangement at (a) z = -2 and (b) z = -1.

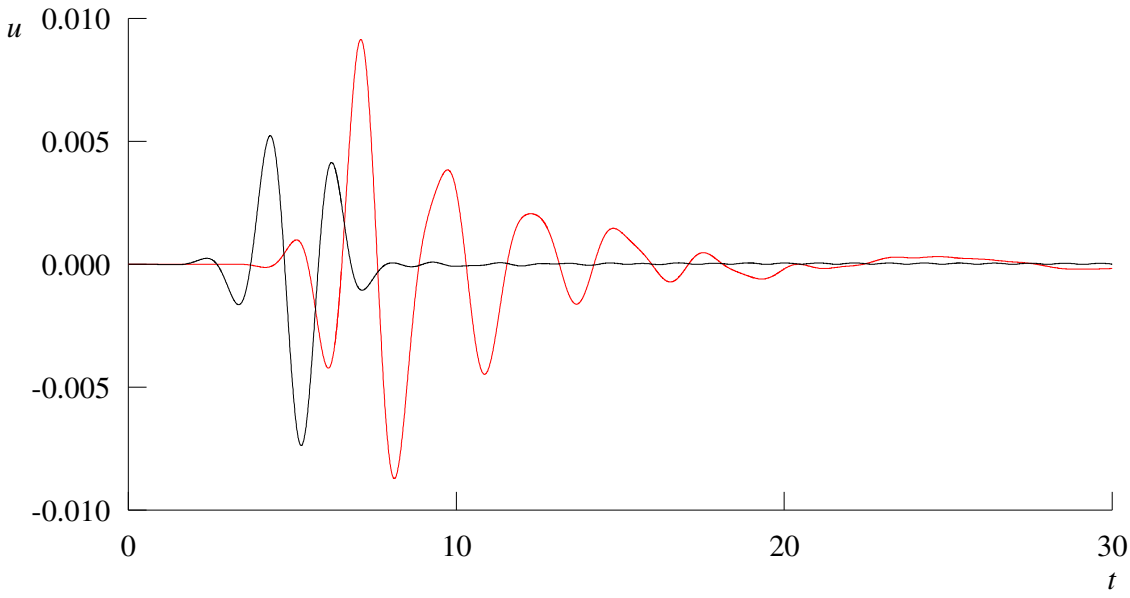

Figure 6.10 Arrival of through-thickness transmission was delayed with the pitch-catch probes right in the middle of the delamination.

Figure 6.11 shows a schematic of a pipe experiencing localized wall-thinning, a corrosion by-product, on its inner surface. Several researchers have reported the potential and effectiveness of using guided elastic waves to detect hidden corrosion defects in tubular and plate-like structures [147-149]. In these works, experimental investigations were combined with numerical simulations. In addition, some literature reports dedicated entire studies to numerical simulation of the complex interaction of guided elastic waves with corrosion [55]. Here, we present a simulation study of a steel pipe with a part-circumferential corrosion. The corrosion is simulated by the wall thinning schematically shown in Figure 6.11. However, the pipe is excited by an axisymmetric load; the problem is 3D due to the asymmetric corrosion. Radial outer-surface displacements excited by

loading the pipe at z = 0, are predicted along several circumferential paths (between 0^o to 180^o) at z = 0.125-1.000.

These time histories are contrasted to their counterparts in flawless pipe. The presence of corrosion is obvious. The corrosion has a relatively stronger effect on the time histories predicted at points located directly above corrosion (z = 0.125-0.625). Circumferentially, the eye-catching change in predicted time histories from a flawless to a corroded pipe takes place at $\theta = 90^o$, the corrosion edge. This key information can guide the identification of a hidden corrosion and an estimate of its circumferential and axial extension in a similar experimental arrangement.

6.6 Conclusions

In this chapter the FE-PML model has been formulated and implement in cylindrical coordinates for simulating propagation and scattering of guided elastic waves in infinite pipes and cylindrical shells. The model has been validated by comparing its output for a cylindrical shell with a 100 inner-radius-to-thickness ratio to the results obtained by using a verified 2D FE-PML for a plate; both are in agreement as expected. In addition to numerical validation, the model has been physically verified by simulating practical NDT experiments. Applications include PE characterization of welded steel pipe, P-C testing of a delaminated composite cylindrical shell, and identification of an internal corrosion in a steel pipe.

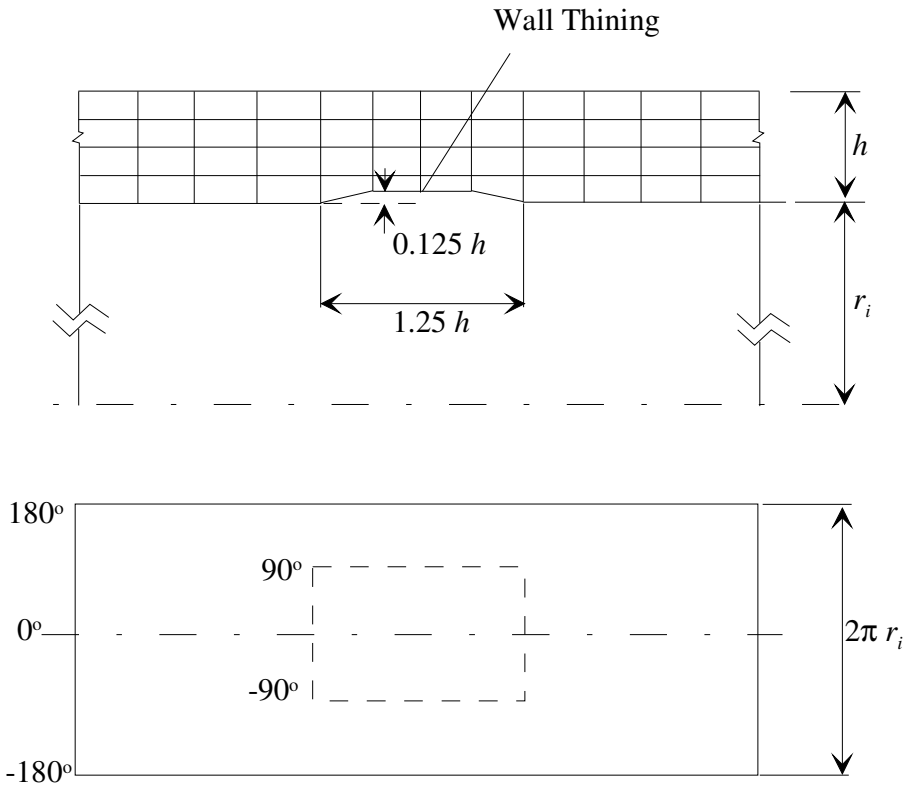

Figure 6.11 A schematic of 3D wall thinning in the steel pipe

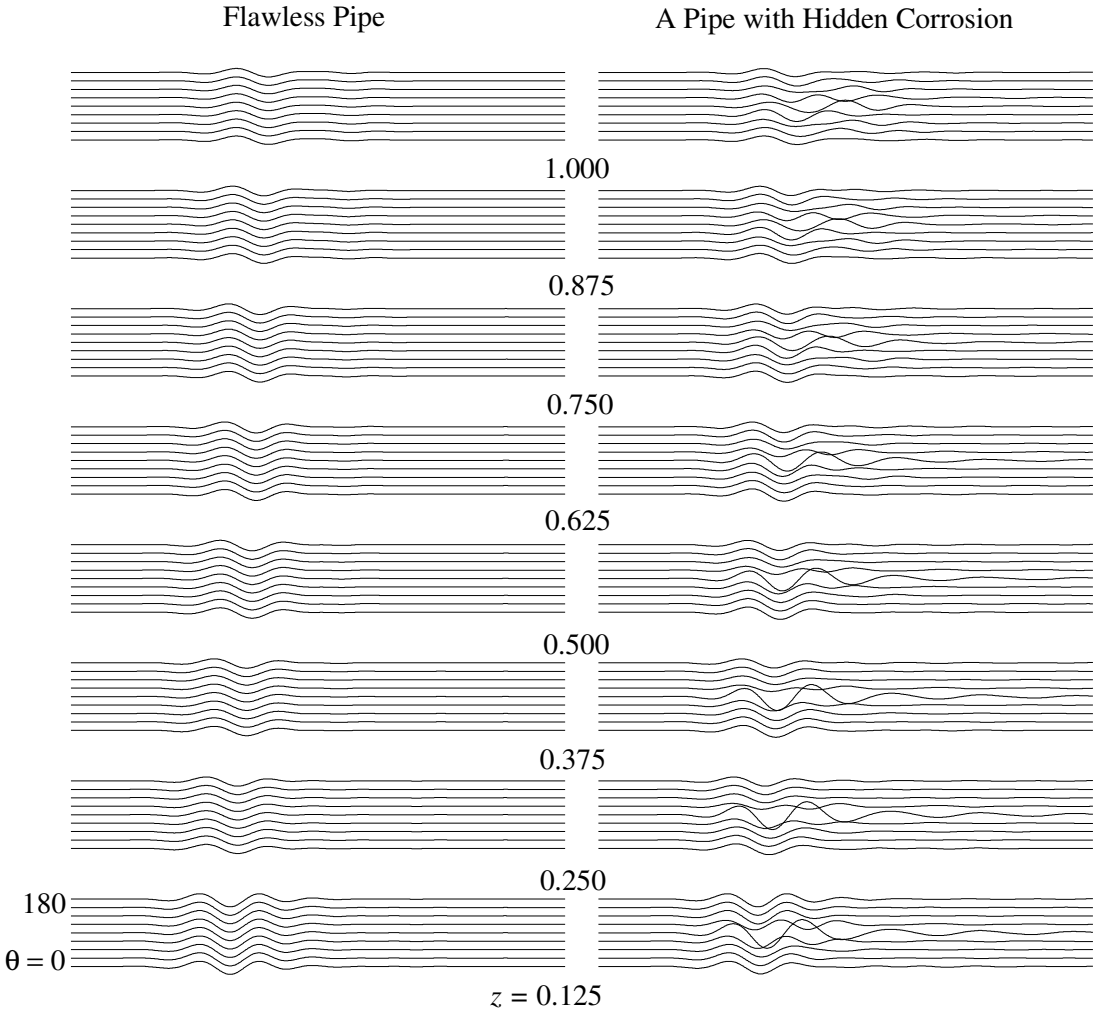

Figure 6.12 Radial displacement time histories predicted at different circumferential and axial locations

"There will come a time when you think everything is finished. That will be the beginning"
Louis L'Amour (1908-1988)

Chapter 7

Conclusions and Future Plan

7.1 Summary of Conclusions

This thesis advocates a combined FE-PML approach to modeling guided elastic wave propagation and scattering in infinite plate-like and cylindrical structures. The model has been validated. In addition, the applicability of the model has been demonstrated, and its pros and cons have been highlighted. Validity of the proposed FE-PML modeling has been established for SH (torsional), PSV (axisymmetric), and 3D waves in plates (and cylinders) has been proven through:

1. Comparative studies of its predictions with:
    a. exact analytical solutions;
    b. semi-analytical solutions; and
    c. available literature data

2. Reciprocity check.
3. Error analysis in reference to a validated EMFE model
4. Reaching to same conclusion(s) reported by previous researchers.
5. Predicting dynamic responses that reflect the physics of the problem.

Applicability of the proposed FE-PML modeling to NDT of cylindrical and plate-like structures is demonstrated by considering practical examples linked to real industrial applications. The model offers substantial savings in computational cost compared to a full FEM simulation. These savings can reach up to 80% in 3D modeling. However, they come at the cost of 0-11% degradation in accuracy. Practically this can be acceptable if there is no other numerical means available for modeling. FE-PML results, however rough, can then be used to judge the feasibility of an experimental NDT program before a financial commitment is made, thus saving what could be wasted money.

7.2 Future Work

Contrasting the combined FE-PML model to the time-efficient BEM will complete the picture of the FE-PML advantages and disadvantages. Furthermore, the author foresees potential applications of the current research progressing in two paths. Along the first path, computational cost effectiveness of the FE-PML can be exploited to produce training data for ANNs. The second path would be a joint effort with experiments to understand in depth the physics of elastic wave propagation and scattering in complex configu-

rations. The two paths should proceed in synergy towards one destination that is inverse characterization of defects.

Bibliography

[1] Y. Y. Lee and K. M. Liew, Detection of damage locations in a beam using the wavelet analysis, Int. J. Struct. Stab. Dyn. 1 (2001) 455

[2] H. –I. Yoon, I. –S. Son, and S. –J. Ahn, Free vibration analysis of Euler-Bernoulli Beam with double cracks, J. Mech. Sci. Technol. 21 (2007) 476

[3] N. J. Carino, M. Sansalone, and N. Hsu, A point source point receiver pulse-echo technique for flaw detection in concrete, J. Am. Conc. Inst. 83 (1986) 199

[4] P. Liu, C. –D. Tsai, and T. –T. Wu, Imaging of surface-breaking concrete cracks using transient elastic waves, NDT & E Int. 29 (1996) 323

[5] P. Cawley and D. Alleyne, The use of Lamb waves for the long range inspection of large structures, Ultrasonics 34 (1996) 287

[6] R. P. Dalton, P. Cawley, and M. J. S. Lowe, The potential of guided waves for monitoring large areas of metallic aircraft fuselage structure, J. Nondestr. Eval. 20 (2001) 29

[7] J. L. Rose, A baseline and vision of ultrasonic guided wave inspection potential, J. Pressure Vessel Technol. Trans. ASME 124 (2002) 273

[8] T. R. Hay, L. Wei, and J. L. Rose, Rapid inspection of composite skin-honeycomb core structures with ultrasonic guided waves, J. Compos. Mater. 37 (2003) 929

[9] A. A. Markov, V. V. Mosyagin, and M. V. Keskinov, A program for 3D simulation of signals for ultrasonic testing of specimens, Russ. J. Nondestr. Test. 41 (2005) 778

[10] G. R. Liu and X Han, Computational Inverse Techniques in Nondestructive Evaluation. CRC Press (2003) Boca Raton

[11] K. Zgonc and J. D. Achenbach, A neural network for crack sizing trained by finite element calculations, NDT & E Int. 29 (1996) 2097

[12] A. Oishi, K. Yamada, S. Yoshimura, G. Yagawa, S. Nagai, and Y. Matsuda, Neural network-based inverse analysis for defect identification with laser ultrasonics, Res. Nondestruct. Eval. 13 (2001) 79

[13] Z. Su and L. Ye, Lamb wave propagation-based damage identification for quasi-isotropic CF/EP composite laminates using artificial neural algorithm: Part I – methodology and data base development, J. Intell. Mater. Syst. Struct. 16 (2005) 97

[14] Z. Su and L. Ye, Lamb wave propagation-based damage identification for quasi-isotropic CF/EP composite laminates using artificial neural algorithm: Part II – implementation and validation, J. Intell. Mater. Syst. Struct. 16 (2005) 113

[15] Y. Lu, L. Ye, Z. Su, L. Zhou, and L. Cheng, Artificial neural network (ANN)-based crack identification in aluminum plates with Lamb wave signals, J. Intell. Mater. Syst. Struct. 20 (2009) 39

[16] S. Grondel, C. Paget, C. Delebarre, J. Assaad, and K. Levin, Design of optimal configuration for generating A_0 Lamb mode in a composite plate using piezoceramic transducers, J. Acoust. Soc. of Am. 112 (2002) 84

[17] N. Hu, T. Shimomukai, H. Fukunaga, and Z. Su, Damage identification of metallic structures using A_0 mode of Lamb waves, Struct. Health Monit. 7 (2008) 271

[18] S. B. Dong and R. B. Nelson, On natural vibrations and waves in plated orthotropic plates, J. Appl. Mech. Trans. ASME 39 (1972) 739

[19] R. B. Nelson and S. B. Dong, High frequency vibrations and waves in laminated orthotropic plates, J. Sound Vib. 30 (1973) 33

[20] S. B. Dong and K. E. Pauley, Plane waves in anisotropic plates, J. Eng. Mech. 104 (1978) 801

[21] E. Kausel, Wave propagation in anisotropic layered media, Int. J. Numer. Methods Eng. 23 (1986) 1567

[22] E. Kausel and J. M. Roësset, Stiffness matrices for layered solids, Bull. Seism. Soc. Am. 71 (1981) 1743

[23] G. R. Liu, J. Tani, T. Ohyoshi, and K. Watanabe, Characteristic wave surfaces in anisotropic laminated plates, J. Vib. Acoust. Trans. ASME 113 (1991) 279

[24] N. Rattanawangcharoen and A. H. Shah, Wave propagation in laminated composite circular cylinders, Int. J. Solids and Struct. 29 (1992) 97

[25] E. Pan, J. Rogers, S. K. Datta, and A. H. Shah, Mode selection of guided waves for ultrasonic inspection of gas pipelines with thick coating, Mech. Mat. 31 (1999) 165

[26] O. Onipede Jr. and S. B. Dong, Propagating waves and end modes in pretwisted beams, J. Sound Vib. 195 (1996) 313

[27] D. Alleyne and P. Cawley, A two-dimensional Fourier transform method for measurement of propagating multimode signals, J. Acoust. Soc. Am. 89 (1991) 1159

[28] C. Eisenhardt, L. J. Jacobs, and J. Qu, Application of laser ultrasonics to develop dispersion curves for elastic plates, J. Appl. Mech. Trans. ASME 66 (1999) 1043

[29] M. Niethammer, L. J. Jacobs, J. Qu, and J. Jarzynski, Time frequency representation of Lamb waves, J. Acoust. Soc. Am. 109 (2001) 1841

[30] W. H. Prosser, M. D. Seale, and B. T. Smith, Time-frequency analyasis of the dispersion of Lamb modes, J. Acoust. Soc. Am. 105 (1999) 2669

[31] K. Luangvilai, W. Punurai, and L. J. Jacobs, Guided Lamb wave propagation in composite plate/concrete component, J. Eng. Mech. 128 (2002) 1337

[32] E. Pan, Static Green's functions in multilayered half spaces, Appl. Math. Modelling, 21 (1997) 509

[33] S. K. Lee, Identification of impact force in thick plates based on the elastodynamics and time-frequency method (I) -Theoretical approach for identification the impact force based on elastodynamics-, J. Mech. Sci. Technol. 22 (2008) 1349

[34] J. Zhu, A. H. Shah, and S. K. Datta, Modal representation of two-dimensional elastodynamic Green's functions, ASCE J. Eng. Mech., 121 (1995) 26

[35] E. Pan and S. K. Datta, Ultrasonic waves in multilayered superconducting plates, J. App. Phys. 86 (1999) 543

[36] G. R. Liu, J. Tani, T. Ohyoshi, and K. Watanabe, Transient waves in anisotropic laminated plates, Part I: Theory, J. Vib. Acoust. Trans. ASME 113 (1991) 230

[37] G. R. Liu, J. Tani, T. Ohyoshi, and K. Watanabe, Transient waves in anisotropic laminated plates, Part II: Application, J. Vib. Acoust. Trans. ASME 113 (1991) 235

[38] X. Han, G. R. Liu, and K. Y. Lam, Transient waves in plates of functionally graded materials, Int. J. Numer. Methods Eng. 52 (2001) 851

[39] X. Han, C. Jiang, S. Gong, and Y. H. Huang, Transient waves in composite-laminated plates with uncertain load and material property, Int. J. Numer. Methods Eng. 75 (2008) 253

[40] W. Zhuang, A. H. Shah, and S. B. Dong, Elastodynamic Green's function for laminated anisotropic circular cylinders, J. Appl. Mech. Trans. ASME, 66 (1999) 665

[41] H. Bai, J. Zhu, A. H. Shah, and N. Popplewell, Three-dimensional steady state Green's function for a layered isotropic plate, J. Sound Vib. 269 (2004) 251

[42] A. Mahmoud, A. H. Shah, and S. B. Dong, Transient response of transversely isotropic composite plates to a point source, J. Appl. Mech. Trans. ASME 73 (2006) 338

[43] W.H. Prosser, M.A. Hamstad, J. Gary and A. O'Gallagher, comparison of finite element and plate theory methods for modeling acoustic emission waveforms, J. NDE. 18 (1999) 83

[44] M. A. Hamstad, J. Gary, and A. O'Gallagher, Far-field acoustic emission waves by three-dimensional finite element modeling of pencil-lead breaks on a thick plate, J. Acoust. Emiss. 14 (1996) 103

[45] R. Ludwig and W. Lord, A finite-element formulation for the study of ultrasonic NDT systems, IEEE Trans. Ultrason. Ferroelectr. Freq. Control 35 (1988) 809

[46] Z. You, M. Lusk, R. Ludwig, and W. Lord, Numerical simulation of ultrasonic wave propagation in anisotropic and attenuative solid materials, IEEE Trans. Ultrason. Ferroelectr. Freq. Control 38 (1991) 436

[47] D. N. Alleyne and P. Cawley, The interaction of Lamb waves with defects, IEEE Trans. Ultrason. Ferroelectr. Freq. Control 39 (1992) 381

[48] D. N. Alleyne, M. J. S. Lowe, and P. Cawley, The reflection of guided waves from circumferential notches in pipes, J. Appl. Mech. Trans. ASME 65 (1998) 635

[49] M. J. S. Lowe, D. N. Alleyne, and P. Cawley, The mode conversion of a guided wave by a part-circumferential notch in a pipe, J. Appl. Mech. Trans. ASME 65 (1998) 649

[50] L. Tang and J. Cheng, Numerical analysis of laser-generated guided elastic waves in a hollow cylinder, J. Nondestr. Eval. 21 (2002) 45

[51] C. A. Issa, K. S. Iyer, and K. Balasubramaniam, Numerical modelling of ultrasonic wave propagation using the efficient p-version finite element method, Ultrasonics 32 (1994) 13

[52] N. Hu, H. H. Wang, B. Yan, H. Fukunaga, D. R. Mahapatra, and S. Gopalakrishnan, The partition of unity finite element method for elastic wave propagation in Reissner-Mindlin plates, Int. J. Numer. Methods Eng. 70 (2007) 1451

[53] D. Rabinovich, D. Givoli, and S. Vigdergauz, Crack identification by 'arrival time' using XFEM and a genetric algorithm, Int. J. Numer. Methods Eng. 77 (2009) 337

[54] F. Moser, L. J. Jacobs, and J. Qu, Modeling elastic wave propagation in waveguides with the finite element method, NDT & E Int. 32 (1999) 225

[55] W. Zhu, An FEM simulation for guided elastic wave generation and reflection in hollow cylinders with corrosion defects, J. Pressure Vessel Technol. Trans. ASME 124 (2002) 108

[56] A. Zewer, A. Polak, and J. C. Santamarina, Rayleigh wave propagation for the detection of near surface discontinuities: finite element modeling, J. Nondestr. Eval. 22 (2003) 39

[57] I. Bartoli, F. L. di Scalea, M. Fateh, and E. Viola, Modeling guided wave propagation with application to the long-range defect detection in railroad tracks, NDT & E Int. 38 (2005) 325

[58] H. Jeong and M. Park, Finite-element analysis of laser-generated ultrasounds for wave propagation and interaction with surface-breaking cracks, Res. Nondestruct. Eval. 16 (2005) 1

[59] C. M. Lee, Guided Elastic Waves in Structures with Arbitrary Cross-section. PhD Thesis. Pennsylvania State University (2006)

[60] I. Erdem, Transient elastic impact response of slender graphite rods, J. Nondestr. Eval. 26 (2007) 89

[61] V. C. Protopappas, I. C. Kourtis, L. C. Kourtis, K. N. Malizos, C. V. Massalas, and D. I. Fotiadis, Three-dimensional finite element modeling of guided ultrasound wave propagation in intact and healing long bones, J. Acoust. Soc. Am. 121 (2007) 3907

[62] G. Baskaran, C. L. Rao, and K. Balasubramaniam, Simulation of the TOFD technique using the finite element method, Insight 49 (2007) 641

[63] W. Ke, M. Castaings, and C. Bacon, 3D finite element simulations of an air-coupled ultrasonic NDT system, NDT & E Int. 42 (2009) 524

[64] J. Lysmer and R. L. Kuhlemeyer, Finite dynamic model of infinite media, ASCE J. Eng. Mech. 95 (1969) 859

[65] J. Lysmer, Lumped mass method for Rayleigh Waves, Bull. Seism. Soc. Am. 60 (1970) 89

[66] J. Lysmer and G. Waas, Shear Waves in plane infinite structures, J. Eng. Mech. 98 (1972) 85

[67] B. H. McDonald and A. Wexler, Finite-element solution of unbounded field problems, IEEE Trans. Microwave Theory Tech. 20 (1972) 841

[68] K. K. Mei, Unimoment method of solving antenna and scattering problems, IEEE Trans. Antennas Propag. 22 (1974) 760

[69] S. Chang and K. K. Mei, Application of the unimoment method to electromagnetic scattering of dielectric cylinders, IEEE Trans. Antennas Propag. 24 (1976) 35

[70] S. K. Datta, A. H. Shah, and C. M. Fortunko, Diffraction of medium and long wavelength horizontally polarized shear waves by edge cracks, J. Appl. Phys. 53 (1982) 2895

[71] T. A. Angelov and T. P. Ivanov, Finite-infinite element analysis of P- and SV-wave propagation in a semi-bounded medium, Comput. Struct. 54 (1995) 377

[72] Z. Abduljabbar, S. K. Datta, and A. H. Shah, Diffraction of horizontally polarized shear waves by normal edge cracks in a plate, J. Appl. Phys. 54 (1983) 461

[73] M. Koshiba, S. Karakida, and M. Suzuki, Finite element analysis of Lamb wave scattering in an elastic plate waveguide, IEEE Trans. Sonics Ultrason. 31(1) (1984) 18

[74] S. K. Datta, Y. Al-Nassar, and A. H. Shah, Lamb wave scattering by a surface-breaking crack in a plate, Review of Progress in NDE, O. D. Thompson and D. E. Chimenti (eds), 10A (1991) 97

[75] Y. N. Al-Nassar, S. K. Datta, and A. H. Shah, Scattering of Lamb waves by a normal rectangular strip weldment, Ultrasonics 29 (1991) 125

[76] W. M. Karunasena, A. H. Shah, and S. K. Datta, Plane-strain-wave scattering by cracks in laminated composite plates, J. Eng. Mech. 117 (1991) 1738

[77] J. Tian, U. Gabbert, H. Berger, and X. Su, Lamb wave interaction with delaminations in CFRP laminates, Comput. Mater. Contin. 1 (2004) 327

[78] G. R. Liu and K. Y. Lam, Characterization of a horizontal crack in anisotropic laminated plates, Int. J. Solids Struct. 31 (1994) 2965

[79] W. Zhaung, A. H. Shah, and S. K. Datta, Axisymmetric guided wave scattering by cracks in welded steel pipes, J. Pressure Vessel Technol. Trans. ASME 119 (1997) 401

[80] N. Rattanawangcharoen, W. Zhaung, A. H. Shah, and S. K. Datta, axisymmetric guided waves in jointed laminated cylinders, J. Eng. Mech. 123 (1997) 1020

[81] C. Zensheu and A. Mal, Scattering of Lamb waves from a rivet hole with edge cracks, Mech. Mater. 31 (1999) 197

[82] A. Mahmoud, A. H. Shah, and N. Popplewell, Parallel hybrid algorithm for three-dimensional elastic wave scattering in steel pipes, J. Pressure Vessel Technol. Trans. ASME 126 (2004) 510

[83] E. Moulin, J. Assaad, C. Delebarre, and D. Osmont, Modeling of Lamb waves generated by integrated transducers in composite plates using a coupled finite element-normal modes expansion method, J. Acoust. Soc. Am. 107 (2000) 87

[84] J. Doyle, Wave Propagation in Structures. Springer (1997) New York

[85] A. T. Patera, A spectral element method for fluid dynamics: laminar flow in a channel expansion, J. Comput. Phys. 54 (1984) 468

[86] D. S. Kumar, D. R. Mahapatra, and S. Gopalakrishnan, A spectral finite element for wave propagation and structural diagnostic analysis of composite beam with transverse crack, Finite Elem. Anal. Des. 40 (2004) 1729

[87] Y. Wang, X. Zhu, H. Hao, and J. Ou, Guided wave propagation and spectral element method for debonding damage assessment in RC structures, J. Sound Vib. 324 (2009) 751

[88] M. Palacz, M. Krawczuk, and W. Ostachowicz, The spectral finite element model for analysis of flexural-shear coupled wave propagation. Part I: laminated multilayer composite beam, Compos. Struct. 68 (2005) 37

[89] M. Palacz, M. Krawczuk, and W. Ostachowicz, The spectral finite element model for analysis of flexural-shear coupled wave propagation. Part II: delaminated multilayer composite beam, Compos. Struct. 68 (2005) 45

[90] A. Chakraborty and S. Gopalakrishnan, A spectral finite element model for wave propagation analysis in laminated composite plate, J. Vib. Acoust. Trans. ASME 128 (2006) 477

[91] A. Zak, A novel formulation of a spectral plate element for wave propagation in isotropic structures, Finite Elem. Anal. Des. 45 (2009) 650

[92] P. Haikou, M. Guang, and L. Fucai, Modeling wave propagation in plate structure using three dimensional spectral element methods for damage detection, J. Sound Vib. 320 (2009) 942

[93] A. H. Harker, Numerical modelling of the scattering of elastic waves in plates, J. Nondestr. Eval. 4 (1984) 89

[94] C. L. Scandrett and J. D. Achenbach, Time-domain finite difference calculations for interaction of an ultrasonic wave with a surface breaking crack, Wave Motion 9 (1987) 171

[95] T. –T. Wu and J. H. Chang, Application of transient elastic waves to the NDE of plate structures with cavity or inclusion, J. Acoust. Soc. Am. 94 (1993) 1453

[96] C. Sridharan, A. Muralidharan, K. Balasubramaniam, and C. V. Krishnamurthy, A simulation study of the impact echo array technique for concrete structure NDT, Nondestruct. Test. Eval. 21 (2006) 123

[97] X. Yin, S. A. Morris, and W. D. O'Brien Jr., Ultrasonic pulse-echo sub-wavelength defect detection mechanism: experimental and simulation, J. Non-destr. Eval. 22 (2003) 103

[98] L. Satyanarayan, C. Sridhar, C. V. Krishnamurthy, and K. Balasubramaniam, Simulation of ultrasonic phased array technique for imaging and sizing of defects using longitudinal waves, Int. J. Pressure Vessels Piping 84 (2007) 716

[99] L. Satyanarayan, K. V. Mohan, C. V. Krishnamurthy, and K. Balasubramaniam, Finite difference time domain simulation of ultrasonic phased array sector scan for imaging cracks in large pipes, elbows, and tee sections, Res. Nondestr. Eval. 19 (2008) 61

[100] Y. Yang, G. Cascante, and M. A. Polak, Depth detection of surface-breaking cracks in concrete plates using fundamental Lamb modes, NDT & E Int. 42 (2009) 501

[101] F. J. Rizzo, D. J. Shippy, and M. Rezayat, A boundary integral equation method for radiation and scattering of elastic waves in three dimensions, Int. J. Numer. Methods Eng. 21 (1985) 115

[102] Y. Cho and J. L. Rose, A boundary element solution of mode conversion study on the edge reflection of Lamb waves, J. Acoust. Soc. Am. 99 (1996) 2097

[103] Y. Cho and J. L. Rose, An elastodynamic hybrid boundary element study of elastic guided wave interactions with a surface breaking defect, Int. J. Solids Struct. 31 (2000) 4103

[104] J. Zhu, A. H. Shah, and S. K. Datta, The evaluation of Cauchy principal value integrals and weakly singular integrals in BEM and their applications, Int. J. Numer. Methods Eng. 39 (1996) 1017

[105] X. Zhao and Joseph Rose, Boundary element modeling for defect characterization potential in a wave guide, Int. J. Solids Struct. 40 (2003) 2645

[106] J. M. Galan and R. Abascal, Elastodynamic guided wave scattering in infinite plates, Int. J. Numer. Methods Eng. 58 (2003) 1091

[107] J. M. Galan and R. Abascal, Boundary element solution for the bidimensional scattering of guided waves in laminated plates, Comput. Struct. 83 (2005) 740

[108] W. Song, J. L. Rose, J. M. Galan, and R. Abascal, Ultrasonic guided waves scattering in a plate overlap, IEEE Trans. Ultrason. Ferroelectr. Freq. Control 52 (2005) 892

[109] G. R. Liu and J. D. Achenbach, Strip element method to analyze wave scattering by cracks in anisotropic laminated plates, J. Appl. Mech. Trans. ASME 62 (1995) 607

[110] P. Fellinger, R. Marklein, K. J. Langenberg, and S. Klaholz, Numerical modeling of elastic wave propagation and scattering with EFIT – elastodynamic finite integration technique, Wave Motion 21 (1995) 47

[111] H. Yim and Y Sohn, Numerical simulation and visualization of elastic waves using mass-spring lattice model, IEEE Trans. Ultrason. Ferroelectr. Freq. Control 47 (2000) 549

[112] R. W. Clayton and B. Engquist, Absorbing boundary conditions for wave-equation migration, Geophysics 45 (1980) 895

[113] R. L. Higdon, Radiation boundary condition for elastic wave propagation, SIAM J. Numer. Anal. 27 (1990) 831

[114] D. Givoli, B. Neta, and I. Patlashenko, Finite element analysis of time-dependent semi-infinite wave-guides with higher order boundary treatment, Int. J. Numer. Methods Eng. 58 (2003) 1955

[115] C. Cerjan, D. Kosloff, R. Kosloff, and M. Reshef, A nonreflecting boundary condition for discrete acoustic and elastic wave equations, Geophysics 50 (1985) 705

[116] J. Sochacki, R. Kubichek, J. George, W. R. Fletcher, and S. Smithson, Absorbing boundary conditions and surface waves, Geophysics 52 (1987) 60

[117] G. R. Liu and S.S. Quek Jerry, A non-reflecting boundary for analyzing wave propagation using the finite element method, Finite Elem. Anal. Des. 39 (2003) 403

[118] L. Ziemianski, Hybrid neural network/finite element modeling of wave propagation in infinite domains, Comput. Struct. 81 (2003) 1099

[119] J. P. Berenger, A perfectly matched layer for the absorption of electromagnetic waves, J. Comput. Phys. 114 (1994) 185

[120] W. C. Chew and W. H. Weedon, A 3D perfectly matched medium from modified Maxwell's equations with stretched coordinates, Microw. Opt. Technol. Lett. 7 (1994) 599

[121] F. D. Hastings, J. B. Schneider and S. L. Broschat, Application of the perfectly matched layer (PML) absorbing boundary condition to elastic wave propagation, J. Acoust. Soc. Am. 100 (1996) 3061

[122] W. C. Chew and Q. H. Liu, Perfectly matched layers for elastodynamic: A new absorbing boundary condition, J. Comp. Acoust. 4 (1996) 341

[123] Q. H. Liu, Perfectly matched layers for elastic waves in cylindrical coordinates, J. Acoust. Soc. Am. 105 (1999) 2075

[124] F. Collino and C. Tsogka, Application of perfectly matched absorbing layer model to the linear elastodynamic problem in anisotropic heterogeneous media, Geophysics 66 (2001) 294

[125] F. Becache, P. Joly, and C. Tsogka, Fictitious domains, mixed finite elements and perfectly matched layers for 2-D elastic wave propagation, J. Comp. Acoust. 3 (2001) 1175

[126] D. Komatitsch and J. Tromp, A perfectly matched layer absorbing boundary condition for the second-order seismic wave equation, Geophys. J. Int. 154 (2003) 146

[127] U. Basu and A. K. Chopra, Perfectly matched layers for time-harmonic elastodynamics of unbounded domains: theory and finite element implementation, Comput. Methods Appl. Mech. Eng. 192 (2003) 1337

[128] U. Basu and A. K. Chopra, Perfectly matched layers for transient elastodynamics of unbounded domains, Int. J. Numer. Methods Eng. 59 (2004) 1039

[129] U. Basu, Explicit finite element perfectly matched layer for transient three-dimensional elastic waves, Int. J. Numer. Methods Eng. 77 (2009) 151

[130] T. Wang and X. Tang, Finite-difference modeling of elastic wave propagation: A nonsplitting perfectly matched layer approach, Geophysics 68 (2003) 1749

[131] W. C. Chew, J. M. Jin and E. Michieissen, Complex coordinate stretching as a generalized absorbing boundary condition, Microw. Opt. Technol. Lett. 20 (1999) 124

[132] K. –J. Bathe, Finite Element Procedures. Prentice Hall (1996) New Jersey

[133] K. Graff, Wave Motion in Elastic Solids. Ohio State University Press (1975) Ohio

[134] J. Zhu, S. K. Datta and A. H. Shah, Modal representation of transient dynamics of laminated plates, Compos. Eng. 5 (1995) 1477

[135] J. Zhu, Numerical Modeling of Elastic Waves in Laminated Composite Plates. Ph.D. Thesis. University of Manitoba (1996)

[136] E. Kausel, Fundamental Solutions in Elastodynamics: A Compendium. Cambridge University Press (2006) Cambridge

[137] G. R. Liu and Z. C. Xi, Elastic Waves in Anisotropic Laminates. CRC Press (2001) Boca Raton

[138] T. J. R. Hughes, Finite Element Method. Prentice-Hall (1987) New Jersey

[139] G. R. Liu and J. D. Achenbach, Strip element method to analyze wave scattering by cracks in anisotropic laminated plates, J. App. Mech. Trans. ASME 62 (1995) 607

[140] R. L. Hudgell, L. L. Morgan, and R. F. Lumb, Non-destructive measurement of the depth of a surface-breaking cracks using ultrasonic Raleigh wave, Br. J. Non Destr. Test. 16 (1974) 144

[141] N. J. Nigro, Steady-state wave propagation in infinite bars of noncircular cross section, J. Acoust. Soc. Am. 40 (1966) 1501

[142] H. Taweel, S. B. Dong, and M. Kazic, Wave reflection from the free end of a cylinder with an arbitrary cross-section, Int. J. Solids Struct. 37 (2000) 1701

[143] O. M. Mukdadi, Y. M. Desai, S. K. Datta, A. H. Shah, and A. J. Niklasson, Elastic guided waves in a layered plate with rectangular cross section, J. Acoust. Soc. Am. 112 (2002) 1766

[144] O. M. Mukdadi and S. K. Datta, Transient ultrasonic guided waves in layered plates with rectangular cross section, J. Appl. Phys. 93 (2003) 9360

[145] A. Mahmoud, N. Popplewell, and A. H. Shah, Exact versus PML absorption of guided SH waves in a cracked plate, Proceedings of the Ninth International Conference on Recent Advances in Structural Dynamics, Paper # 099 (on a CD)

[146] A. Mahmoud and Y. Luo, Application of a perfectly matched layer boundary condition to finite element modeling of elastic wave scattering in cracked plates, Adv. Theo. Appl. Mech., 2 (2009) 75

[147] W. Zhu, J. L. Rose, J. N. Barshinger, and V. S. Agarwala, Ultrasonic guided wave NDT for hidden corrosion detection, Res. Nondestr. Eval., 10 (1998) 205

[148] J. L. Rose and L. E. Soley, Ultrasonic guided waves for anomaly detection in aircraft components, Mat. Eval., 58 (2000) 1080

[149] D. Tuzzeo and F. Lanza di Scala, Noncontact air-coupled guided waves ultrasonics for detection of thinning defects in aluminum plates, Res. Nondestr. Eval., 13 (2001) 61

Vita

Abdel-Rahman (*alias* Abdu) Mahmoud was born in the city of Manfalut, Egypt. Abdu earned his B.Sc. degree in 1997 from Assiut University Mechanical Engineering Department with a major in applications of mechanical engineering in agriculture. Abdu was granted an assistantship to pursue his M.Sc. studies at the University of Manitoba (then) Mechanical and Industrial Engineering Department. Abdu has earned his M.Sc. degree in 2002 along with the prestigious University of Manitoba Graduate Fellowship to pursue his Ph.D. studies. Abdu joined Schlumberger Technology Corporation as a junior field engineer in 2006. With Schlumberger, Abdu designed/installed electrical submersible pumping applications and developed new reverse-flow check systems for retrievable gas lift valves. Abdu has co-authored several publications and a pending US patent.